UNIVERSIDAD NACIONAL AUTÓNOMA DE MÉXICO

PROGRAMA DE MAESTRÍA Y DOCTORADO EN INGENIERÍA
ENERGÍA - USO EFICIENTE DE ENERGÍA

EXPERIMENTAL AND THEORETICAL STUDY OF ELECTRICALLY DRIVEN VORTICES IN A LIQUID METAL LAYER

TESIS
QUE PARA OPTAR POR EL GRADO DE:
DOCTORA EN INGENIERÍA

PRESENTA:
CINTHYA GUTIÉRREZ LARA

TUTOR PRINCIPAL:
DR. SERGIO CUEVAS GARCÍA, IER-UNAM

COMITÉ TUTOR:
DR. EDUARDO RAMOS MORA, IER-UNAM
DR. ALDO FIGUEROA LARA, CONAHCYT-CInC-UAEM
DR. ALBERTO BELTRÁN MORALES, ENES-UNAM
DR. RAÚL ALEJANDRO ÁVALOS ZÚÑIGA, CICATA-IPN

CIUDAD DE MÉXICO, SEPTIEMBRE 2023

JURADO ASIGNADO:

Presidente:	Dr. Eduardo Ramos Mora
Secretario:	Dr. Sergio Cuevas García
Vocal:	Dr. Aldo Figueroa Lara
1er. Suplente:	Dr. Alberto Beltrán Morales
2do. Suplente:	Dr. Raúl Ávalos Zúñiga

Lugar donde se realizó la tesis:

Instituto de Energías Renovables, Temixco, Morelos, México.

TUTOR DE TESIS:

Dr. Sergio Cuevas García

FIRMA

Dedicado a

Mis hijos Saúl y Lucía, por ser mi mayor inspiración.

A mi esposo Saúl, por todo el amor que me da.

A mi madre por todo su apoyo.

Agradecimientos

A la Universidad Nacional Autónoma de México, especialmente al Instituto de Energías Renovables por el apoyo brindado durante mis estudios de Posgrado.

A CONAHCyT (Consejo Nacional de Humanidades, Ciencias y Tecnologías), por brindarme el soporte económico para realizar mis estudios de Posgrado.

A los miembros de mi comité tutoral, sus críticas y comentarios fueron de gran ayuda para mejorar la calidad de mi trabajo de investigación.

A James que ahora lo considero un hermano más. A mis amigos y compañeros, gracias por todos los momentos compartidos.

Agradezco especialmente al Dr. Sergio Cuevas García por haberme permitido trabajar bajo su supervisión. Agradezco su confianza y el gran apoyo que tuve de su parte para desarrollarme académicamente y como ser humano.

Agradezco también al Dr. Aldo Figueroa Lara por todo su apoyo y orientación a lo largo de la realización de este trabajo. Definitivamente, es un excelente mentor.

Contents

Resumen

En este trabajo se presenta un estudio teórico-experimental del patrón de vórtices en una delgada capa de metal líquido vertida en un contenedor rectangular, donde el movimiento del fluido es generado por la interacción de una corriente eléctrica directa y un campo magnético no uniforme producido por un imán permanente de forma cuadrada, y cuyo tamaño es mucho menor que el contenedor. Mientras una configuración similar origina un vórtice dipolar clásico cuando el fluido de trabajo es un electrolito de baja conductividad, los experimentos muestran que en una capa de metal líquido se forma una estructura más compleja. En un fluido de alta conductividad, las observaciones muestran un vórtice dipolar anidado con una región de cuasi-estancamiento en la zona donde el campo magnético es más intenso. Dos recirculaciones externas encierran el vórtice dipolar interior. El patrón de cuatro vórtices resulta de la superposición de varias fuerzas electromagnéticas producidas por la interacción de las corrientes aplicadas e inducidas con el campo magnético de orientación norte, que presenta una distribución Gaussiana, con valores de campo positivos en las regiones cercanas al imán, y valores negativos en regiones más alejadas, cuya magnitud tiende a cero suficientemente lejos. El método de generación electromagnética de vórtices en metales líquidos bajo campos magnéticos no-uniformes localizados no ha sido muy explorado, a pesar de ser una herramienta fundamental en el procesamiento electromagnético de materiales. La principal motivación de este estudio es generar conocimiento del mezclado producido por fuerzas electromagnéticas de manera no-intrusiva en fluidos de alta conductividad que pueda ser aplicado para mejorar diversas aplicaciones industriales. Para ello, el flujo es visualizado a través de burbujas trazadoras, generadas por una reacción química del metal líquido y el ácido clohídrico. Los experimentos realizados para distintas corrientes eléctricas se cuantifican utilizando dos técnicas de medición. Los perfiles de velocidad se obtienen a lo largo de un eje en distintos puntos con la técnica de Velocimetría Doppler Ultrasónica. Además los campos de velocidades en todo el dominio experimental se obtienen mediante la técnica de Velocimetría por Imágenes de Partículas, utilizando las burbujas generadas en la superficie superior del metal líquido como trazadores. La parte teórica se divide en un estudio analítico y un análisis numérico. Para el estudio teórico se presentan las ecuaciones de la magnetohidrodinámica para un fluido incompresible, viscoso y eléctricamente conductor bajo un campo magnético aplicado, suponiendo que el número de Reynolds magnético es pequeño. En el caso analítico se obtiene una solución puramente bidimensional resolviendo las ecuaciones fundamentales mediante dos expansiones asintóticas. El modelo analítico muestra una buena comparación cualitativa con los resultados experimentales. En el estudio numérico, se desarrolla un modelo numérico cuasi-bidimensional que toma

en cuenta los efectos de la capa límite adherida a la pared del fondo, la fricción de Hartmann y los efectos inducidos. Las soluciones numéricas muestran buenas comparaciones cualitativas y cuantitativas con los resultados experimentales. Además, utilizando el modelo numérico puramente bidimendional se predice la formación de vórtices anidados para campos magnéticos muy intensos.

Abstract

In this work, we present an experimental and theoretical study of the vortex pattern in a thin liquid metal layer contained in a rectangular box, in which the fluid motion is generated by the interaction of a uniform direct current and a non-uniform magnetic field produced by square-shaped permanent magnet much smaller than the container. While a similar configuration originates a classical vortex dipole when the working fluid is a low conductivity electrolyte, experiments show that in a liquid metal layer, a more complex pattern is formed. The observations in the high conductivity fluid show a vortex dipole nested with a quasi-stagnation region in the zone of strongest magnetic field. Two external recirculations circle around the inner dipolar vortex. The four vortex pattern results from the superposition of several electromagnetic forces produced by the interaction of the applied and induced currents with the magnetic field of north orientation, which presents a Gaussian distribution with positive field values in the regions near the magnet and negative values in more remote regions, the magnitude of which tends to zero far enough away. The method of electromagnetic generation of vortices in liquid metals under localized non-uniform magnetic field has remained largely unexplored, in spite of being a fundamental tool for the electromagnetic processing of materials. The main motivation of this study is to generate basic knowledge of the mixing produced by electromagnetic forces in a non-intrusive way in a high conductivity fluid that can be applied to improve diverse industrial applications. The flow is visualized by tracking bubbles generated by the chemical reaction of the liquid metal and the hydrochloric acid layer on top of it. The experiments performed for different electrical currents are quantified using two measurement techniques. Velocity profiles are measured along an axis in different positions using the Ultrasonic Doppler Velocimetry technique. The velocity fields in the whole experimental area are obtained through the Particle Image Velocimetry technique using as tracers the bubbles generated in the top surface of the liquid metal. The analysis of the flow includes an analytical study and a numerical analysis. For the theoretical study, the fundamental equations of magnetohydrodynamics for a incompressible, viscous and electrically conducting fluid under an applied magnetic field are presented assuming the low magnetic Reynolds number approximation. In the analytical case, a purely two-dimensional solution is obtained by solving the governing equations using two asymptotic two expansions. The analytical model shows a satisfactory qualitative agreement with the experimental results. In the numerical study, a quasi-two-dimensional numerical model that takes into account the effect of the boundary layers adhered to the bottom wall, the Hartmann friction and the induced effects, is developed. Numerical simulations show a satisfactory qualitative and quantitative agreement with the experimental results. Fur-

ther, using the purely two-dimensional numerical model six nested vortices are predicted when the magnetic field strength is increased.

Introduction

The study of vortex dynamics is a very important topic in fluid mechanics since it is relevant in a large number of natural phenomena and many technological applications. For instance, to a large extent the evolution of atmospheric and oceanic phenomena are determined by the motion of vortices such as whirlwinds, tornadoes, hurricanes and ocean gyres. In fact, several laboratory-scale studies have been carried out to mimic ocean flows using non-intrusive electromagnetic methods that are capable of generating vortex motions in electrically conducting fluids such as electrolytes. In turn, electromagnetic forces have also been used to produce stirring and mixing in liquid metals in technological applications related to materials processing.

Although most metals become liquid at high temperatures, some of them are liquid at room temperature. Typical examples of this kind of liquid metals (LM) are mercury (Hg), and gallium alloys, the latter being commonly used in laboratory applications in different eutectic alloys (e.g. GaIn and GaInSn) due to its stability and nontoxicity. In recent years, the rapid development of Additive Manufacturing (AM) technology, in combination with the use of liquid metals, has opened the door to fabricate small-sized devices for different applications, such as tunning components for radio frequency and microwave applications (McClung et al., 2018; Liu et al., 2020), strain sensors for medical applications (Otake and Konishi, 2018; Li et al., 2019), pressure sensors (**?**), flexible electronics (Kim et al., 2017), soft robots (**?**), wearable devices (**?**), and thermal management (**?**). A review on liquid metal-based devices, their properties and applications can be found in Dong et al. (2021). To improve and optimize any of these applications, the behavior of the LM inside the used devices must be understood in detail. To that end, in many studies the dynamics of the flow is analyzed using analytical, experimental and numerical techniques.

The use of a static magnetic field for the production of vortex flow in conducting fluids has been widely investigated since the pioneering studies of magnetohydrodynamics (MHD), many of which were developed in the former Soviet Union, with the aim of understanding atmospheric phenomena (Bondarenko and Gak, 1978; Bondarenko et al., 1979; Dovzhenko et al., 1979; Ponomarev, 1980; Dovzhenko et al., 1981; Krymov, 1989; Manin, 1989; Batchaev and Ponomarev, 1989; Dolzhanskii et al., 1990, 1992). The assumption that the magnetic field is uniform and homogeneous underlies most of the analyzed situations, many of them related with technological applications. For instance, recently, Rivero et al. (2022) analyzed a LM vortex generator using an analytical model and numerical

simulations, both of which were partially validated using experimental data obtained using a laboratory prototype. By varying the size of the external electrode, the authors assessed the efficiency of the generator, which has a potential use in energy harvesting applications. The study of MHD flows has been an active area of research, as evidenced by the large body of recent literature devoted to the analysis this kind of flows for diverse applications such as fusion reactors (Klüber et al., 2020; Bühler et al., 2020; Mistrangelo et al., 2021), heat transfer (Singh and Gohil, 2019; Alzabut et al., 2023; Hickie-Bentzen et al., 2023), energy harvesting (**?**) and even biomedicine (Cherkaoui et al., 2022).

A liquid metal flow under a strong uniform magnetic field, for which the low magnetic Reynolds number approximation holds (Davidson, 2001), presents two important well-known features. On the one hand, the anisotropy introduced by a uniform field is manifested by the elongation of flow structures in the direction parallel to the field (Alemany et al., 1979). On the other hand, the motion of the conducting liquid across the field lines induces electric currents that lead to Joule dissipation and, consequently, to the damping of the flow (Davidson, 1995). The evolution of vortices under these conditions has been investigated both experimentally and theoretically in the past, see for instance Mück et al. (2000); Sreenivasan and Alboussière (2000, 2002); Hamid et al. (2015) and references therein.

Uniform magnetic fields have also been used for the generation of vortices in thin liquid metals layers, with Lorentz forces created by the interaction of injected electric currents with the applied field. Relevant studies have used this methodology, for instance, Sommeria analyzed isolated vortex dynamics (Sommeria, 1988) as well as steady two-dimensional vortex couples (Nguyen Duc and Sommeria, 1988) in a thin layer of mercury. This author also provided experimental evidence of the inverse energy cascade characteristic of quasi-two-dimensional turbulence (Sommeria, 1986). The energy transfer towards large scales that arises in this kind of turbulence, was also explored by Messadek and Moreau (2002) in a quasi-two-dimensional turbulent shear flow by enforcing a mercury layer by the action of a steady vertical magnetic field and a radial horizontal electric current in a cylindrical container. These studies confirm that the quasi-two-dimensional flow behaviour prevails in thin liquid metal layers under strong uniform magnetic fields where the key dissipation mechanism is the Hartmann layer friction. Nevertheless, more recent studies have examined the limit of the quasi-two-dimensionality assumption and showed evidence of a transition between quasi-two-dimensional and three-dimensional flows in liquid metal MHD flows, see for instance Ref. (Klein et al., 2009).

Although some interesting investigations of MHD vortices generated using alternative procedures as the one mentioned above have been reported (v. e. Kolesnichenko et al. (2005)), it appears that electrically driven vortices in liquid metals under non-uniform magnetic fields have remained largely unexplored. This is not the case for electrolyte flows since in many experimental works one or several small magnets interacting with applied currents have been used to generate vortical flows. In fact, it is well known that

in a thin layer of electrolyte the interaction of a uniform DC current with a permanent magnetic dipole results in a vortex dipole (Lara, 2013; Salas et al., 2001; Figueroa et al., 2009). If a current pulse is applied, a travelling vortex dipole is created by the localized Lorentz force (Afanasyev and Korabel, 2004). Since electrolytes are low conductivity liquids, electric currents induced by the fluid motion across the applied magnetic field, are completely negligible. The question then arises as to how is the flow structure modified in this simple experiment if the thin layer is a liquid metal instead of an electrolyte. It is worth mentioning that very interesting vortex patterns have been observed when a magnet is dragged underneath a liquid metal layer (Samsami et al., 2014; Prinz et al., 2016). In fact, a sequence of vortices can be generated by varying the magnet velocity although in this case Lorentz forces are only produced by induced currents.

In this work, we present an experimental and numerical study of electrically driven vortices in a thin liquid metal layer (GaInSn) contained in a rectangular box under a dipolar magnetic field created by a permanent magnet of small size compared with the container. It is shown that the action of a uniform DC current with the localized magnetic field results in a vortex dipole with a central zone of reduced velocity nested inside two external vortices. Apparently, this flow structure has not been previously reported experimentally although a similar structure was found by Cuevas et al. (2006) in numerical simulations of a pressure driven creeping flow past a magnetic obstacle (see also **?**). In the present contribution, velocity profiles along the symmetry axis of the flow were obtained through Ultrasonic Doppler Velocimetry (UDV). In addition, velocity fields were captured in the liquid metal surface by Particle Image Velocimetry (PIV), using as tracers the bubbles generated in the acid layer on top of the liquid metal. The analysis is complemented with finite volume numerical simulations based on a quasi-two-dimensional model which approximates the MHD flow in the thin liquid metal layer. We carry out a comparison of numerical results with experimental data obtained with both techniques and discuss the formation of the flow structure taking into account the applied and induced forces as well the non-uniformity of the magnetic field.

This thesis is structured as follows. In Chapter 1, we present the experimental setup used to carry out a laboratory study of electrically driven vortices in a thin liquid metal layer (GaInSn) contained in a rectangular box under a dipolar magnetic field generated by a permanent magnet of small size compared with the container. The experimental results show that the action of a uniform DC current with the localized magnetic field results in a vortex dipole with a central zone of reduced velocity nested inside two external vortices. The flow dynamics is explored by means of two experimental techniques of velocity measurement. First, velocity profiles along the symmetry $x-$axis of the flow and parallel to it were obtained through Ultrasonic Doppler Velocimetry (UDV) in the liquid metal bulk. Secondly, velocity fields were captured in the liquid metal surface by Particle Image Velocimetry (PIV), using as tracers the bubbles generated in the acid layer on top of the liquid metal. The distribution of the magnetic field is measured experimentally at the two heights in which the velocity measurements are taken. Then, the magnetic field is

reproduced with the analytic formula provided by (McCaig, 1977) using two magnetized plates. Experimental results are presented and analysed.

Chapter 2 is focused on the analytical model of the flow pattern produced by electromagnetic forces in a high conductivity fluid. Here, a summary of the fluid dynamics and Maxwell's equations is presented. Under certain assumptions, the fundamental MagnetoHydroDynamic (MHD) equations were established by implementing a formulation that uses the induced magnetic field as the electromagnetic dependent variable. The flow behavior is analyzed mathematically using a purely two-dimensional model. The analytical solution was found through the expansion in Reynolds (Re) and Hartmann (Ha) parameters, considering that ReHa $\ll 1$. Despite the fact that there is a singularity in the origin due to the equation used to model the magnetic field, the analytical results show the symmetric formation of two nested dipolar vortices.

In Chapter 3, the flow pattern obtained experimentally is modeled numerically using a quasi-two-dimensional approximation as proposed by Figueroa et al. (2009). This averaged numerical model takes into account the main features that affect the vortical flow, namely, the Hartmann and bottom frictions, the decay of the non-uniform magnetic field in the direction normal to the liquid metal layer and the induced currents generated in the applied magnetic field region. The numerical simulations were performed in two different planes of the fluid layer in order to compare with the velocity measurements taken with the two techniques used. The numerical comparison of the velocity field shows a good qualitative agreement with the field obtained by means of the PIV technique. In turn, the velocity profiles obtained from the simulations show a good quantitative agreement with the experimental profiles obtained with the UDV technique. In addition, in this chapter a purely two-dimensional model to carry out an idealized numerical analysis of the shallow flow generated by an applied electrical current and a localized magnetic field produced by a very strong permanent magnet, is explored. Unlike the quasi-two-dimensional simulations, in this model is only taken into account the applied and induced Lorentz force and the magnetic field distribution. With this model, a flow pattern composed by three nested dipolar vortices is found. Even though the formation of a greater number of vortices is obatined with the ideal model in absence of bottom friction, in the experiments we can observe some evidence of the same vortex pattern. A similar pattern was reported by **?** in a numerical study of the creeping flow past a magnetic obstacle. At the end of the chapter, a numerical comparison with the two experimental techniques is discussed.

Finally, the main conclusions of this thesis are summarized and some topics for future work are presented.

Chapter 1

Experimental vortex patterns

In this chapter, the experimental device used for the study of flow patterns generated by non-uniform electromagnetic forces acting on highly electrically conducting fluids, is presented. Since the magnetic field produced by the permanent magnet is an important factor in the fluid motion, measurements of the magnetic field distribution were performed. In order to analyze the flow dynamics, optical visualizations and experimental measurements were carried out. The Ultrasound Doppler Velocimetry (UDV) and Particle Image Velocimetry (PIV) techniques were used to measure the velocities of the liquid metal. Some results are presented in the last section.

1.1 Experimental setup

The experimental setup consists of a rectangular box with inner measurements of 27 cm long, 25 cm wide and 4 cm high. The device frame is made of plexiglass glued to a glass plate of thickness 0.3 cm. An acrylic base, with a square cavity in the central region, is placed underneath the glass bottom wall in order to support the weight of the working fluid. Two copper electrodes of rectangular cross-section with length, width, and height of 25 cm, 1 cm and 0.5 cm, respectively, are placed parallel to the width of the container. The container is filled up with a liquid metal layer composed of an eutectic Gallium, Indium, and Tin (GaInSn) alloy that is in liquid state at room temperature, and whose properties, namely, mass density ($\rho = 6360$ kg/m^3), kinematic viscosity ($\nu = 3.4\times10^{-7}$ m^2/s), electrical conductivity ($\sigma = 3.46\times10^6$ S/m), surface tension ($\gamma = 0.533$ N/m), speed of sound ($\nu_\iota = 2725$ m/s) and magnetic permeability ($\mu = 4\pi\times10^{-7}$ N/A^2), are considered as constant (Morley et al., 2008). A secondary layer, with thickness of 0.3 cm of a hydrochloric acid solution at 3% by weight, is poured on top of the liquid metal in order to reduce its oxidation. The depth of the liquid metal layer is 0.55 cm. In this way, the copper electrodes are completely submerged in the liquid metal, avoiding its contact with the hydrochloric acid layer, thus preventing electrochemical reactions that produce noise in the experiments. A square-shaped Neodymium-Iron-Boron permanent magnet, with a length-side of 2.54 cm and height of 1.27 cm, is placed in the cavity of the acrylic base, touching the lower surface of the glass plate. The center of the magnet coincides with the geometric center of the container. The magnet, with north orientation, is magnetized along the normal direction of the free surface of the fluid and has a maximum strength of 0.33 T at its center.

An adjustable DC voltage source is connected to the electrodes to produce a uniform electric current along the positive direction of the x axis through the fluid. The applied electric current was varied from 0.25 A up to 2 A. The origin of the coordinate system is fixed at the geometric center of the container, at the top wall of the glass plate, with the $x-$ and $y-$axes parallel to the applied current, and to the longest side of the electrodes, respectively. The $z-$direction points in the same direction as the normal component of the glass plate. The open container is placed on three supports so that the system can be leveled to obtain a liquid metal layer with a uniform height. Figure 1.1a) shows a sketch of the top view of the experimental device. We can observe that the power supply is connected in the central part of the electrodes by means of an electrical conductor, while Figure 1.1b) shows the lateral view of the setup, where the confined fluid, the magnetic field lines, and the electrodes immersed in the liquid metal, can be observed. Once the DC voltage source is switched on, an approximately uniform electric current interacts with the magnetic field producing Lorentz forces that originates motion within the liquid metal. Despite considerably high electrical currents are applied throughout the liquid metal, temperature changes within the fluid are negligible due to its high electrical conductivity.

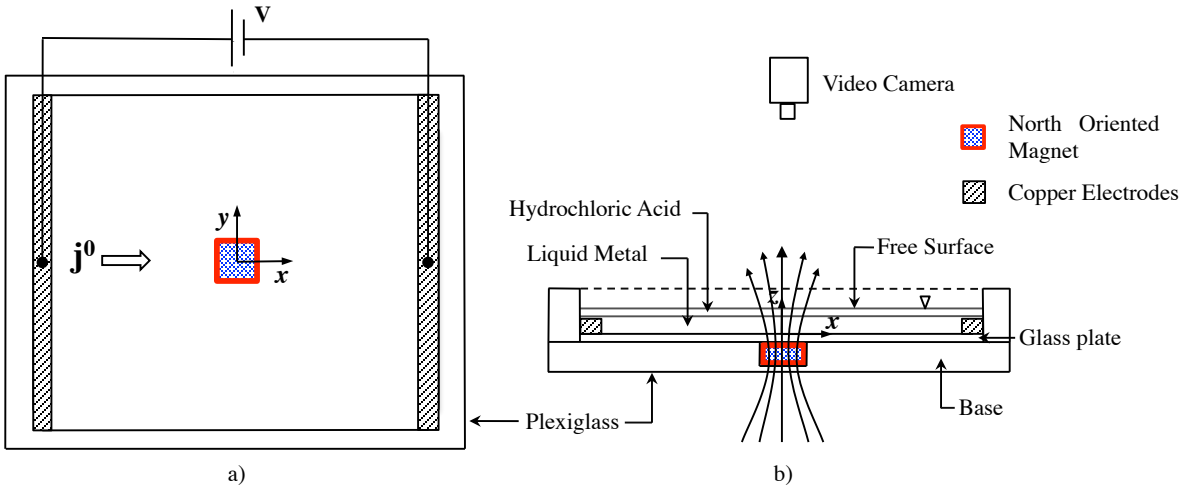

Figure 1.1: Schematic representation of the experimental device used to study the vortex dynamics produced by localized Lorentz forces in a liquid metal layer; a) plane view and b) lateral view along the $x-$axis.

1.1.1 Magnetic field characterization

In order to understand in detail the phenomenon under study, it is necessary to characterize the applied magnetic field responsible for the fluid motion. For this purpose, the magnetic field was measured on two fixed planes at different heights in the $z-$direction. The selected heights were chosen to be the same at which the experimental measurements

of the velocities were carried out. The magnetic field was measured along the x and y symmetry axes. The experimental measurements of the magnetic field, as functions of the distance along the axes, for two different heights (3.5 mm and 5.5 mm), are plotted with points in Figures 1.2a) and 1.2b). Taking into account that the normal magnetic field component is dominant, and that the transversal components are very small (Figueroa et al., 2009; Alboussière, 2004), the dimensionless magnetic field, along the $z-$direction, of a dipolar magnet can be reproduced using the analytical expression presented by Figueroa et al. (2009):

$$\mathcal{B}_z^0(x,y,z) = \mathscr{B}_z^0(x,y)g(z), \tag{1.1}$$

where the term $\mathscr{B}_z^0(x,y)$ reproduces the variation of the magnetic field in the $(x-y)$ plane using the analytical expression given by McCaig (1977) for a uniformly magnetized rectangular surface (Figueroa et al., 2009; Beltrán, 2010; Cuevas et al., 2006). The term $g(z)$ represents the variation of the magnetic field (measured experimentally) in the normal direction ($z-$axis) given by

$$g(z) = \exp(-\gamma\varepsilon z), \tag{1.2}$$

in which $\gamma = 2.05$ is an empirical constant; $\varepsilon = h/L$, h and L being the depth of the liquid layer, and the characteristic length, respectively, and z is normalized by h (Figueroa, 2010).

The experimental measurements show a magnetic field distribution with positive and negative values. This behavior can be reproduced by the superposition of two parallel magnetized square surfaces of length L, separated by a distance c, with opposite polarity, so that both external surfaces act as the north and south poles of the magnet. The dimensions L and c were fixed so that the distribution of the magnetic field coincides with the experimentally measured magnetic field distribution. The explicit expression by McCaig (1977) for the magnetic field is

$$\begin{aligned}
\mathscr{B}_{z_i}^0(x,y) \;=\; \xi\Bigg\{ & \arctan\left(\frac{(x+a)(y+b)}{z_{0i}\left[(x+a)^2+(y+b)^2+z_{0i}^2\right]^{1/2}}\right) \\
& + \arctan\left(\frac{(x-a)(y-b)}{z_{0i}\left[(x-a)^2+(y-b)^2+z_{0i}^2\right]^{1/2}}\right) \\
& - \arctan\left(\frac{(x+a)(y-b)}{z_{0i}\left[(x+a)^2+(y-b)^2+z_{0i}^2\right]^{1/2}}\right) \\
& - \arctan\left(\frac{(x-a)(y+b)}{z_{0i}\left[(x-a)^2+(y+b)^2+z_{0i}^2\right]^{1/2}}\right)\Bigg\},
\end{aligned} \tag{1.3}$$

where ξ is a normalization constant. The dimensions of the magnetized surface are $x_0 = 2a$ and $y_0 = 2b$, where $2a = 2b = L$. Subscript i takes values of 1 and 2, which correspond to the magnetic fields produced by the two square surfaces, normalized by the maximum magnetic field (B_{max}), measured at the geometrical center of the magnetized surface. The total magnetic field distribution $\mathscr{B}_z^0(x,y)$ in the $(x-y)$ plane is the superposition of the fields calculated as

$$\mathscr{B}_z^0(x,y) = \mathscr{B}_{z_1}^0 - \mathscr{B}_{z_2}^0. \tag{1.4}$$

Figures 1.2a) and 1.2b) show the comparison between the experimental results and the magnetic field calculated with McCaig (1977) equation for the planes at $z = 3.5$ mm and $z = 5.5$ mm, respectively. In these, the measured profiles of the normalized $z-$component of the magnetic field, along the x and y symmetry axes, are very similar to each other, for the two selected heights, thus demonstrating the uniformity of the magnetization and the symmetry of the magnetic field. In addition, the analytical magnetic field profiles of the normalized $z-$component are in good qualitative and quantitative agreement with the experimentally measured profiles for the two heights.

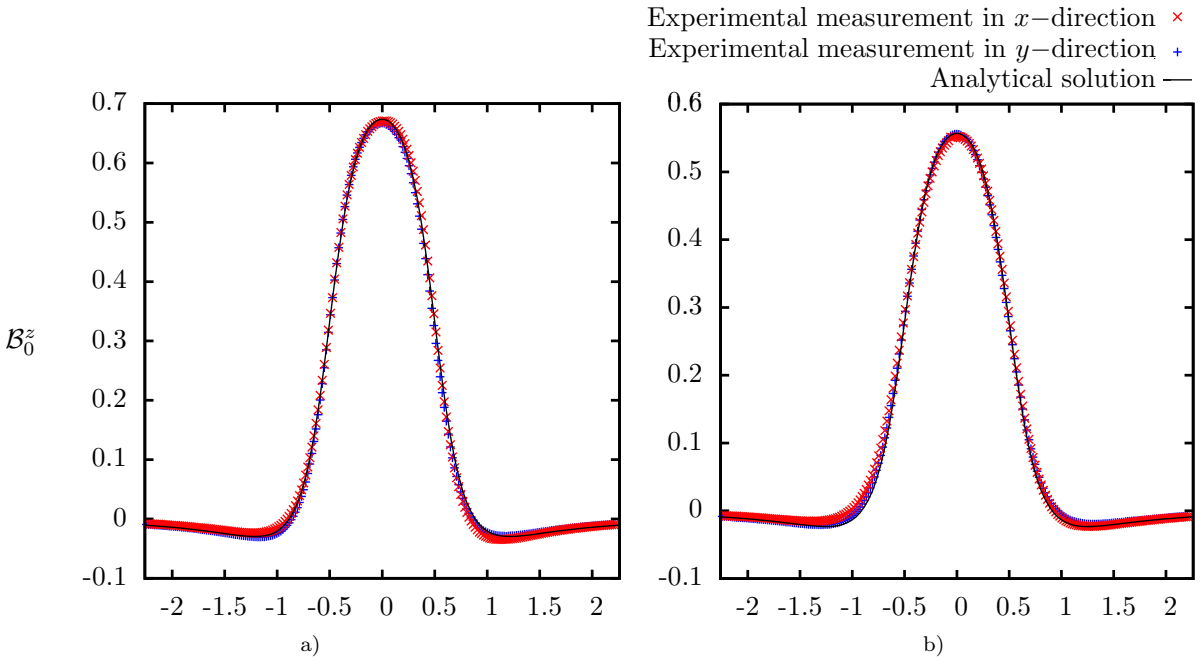

Figure 1.2: Experimental and analytical profiles of the normalized $z-$component of the magnetic field as functions of x and y for two heights within the liquid metal layer at a) 3.5 mm and b) 5.5 mm. The red and blue symbols represent the $z-$component of the magnetic field measured experimentally along the x and y symmetry axes, respectively, while the solid black line is the magnetic field calculated with the expression given by McCaig (1977).

The maximum magnetic field strength ($B^0_{z,m}$) measured at $z = 3.5$ mm is 0.218 T, whereas, at $z = 5.5$ mm is 0.181 T. With these values of magnetic field, it is possible to obtain the ratio between the Lorentz forces and viscous forces by means of the dimensionless parameter called the Hartmann number (Ha):

$$Ha = B^0_{z,m} L \sqrt{\frac{\sigma}{\rho\nu}}. \tag{1.5}$$

The Hartmann number calculated with the maximum magnetic field of 0.218 T is $Ha = 221$, whereas, this parameter takes the value $Ha = 184$ for the maximum strength of 0.181 T.

1.1.2 Experimental visualizations

The experimental visualizations are performed using the bubbles generated at the interface between the liquid metal and the hydrochloric acid layers which allowed to observe the motion of the liquid metal surface. Initially, the gas bubbles are produced due to the chemical reaction between the liquid metal and the acid. However, bubble production increases when the electrodes, hydrochloric acid, and liquid metal are in contact with one another, even before the DC current is present. Bubble generation is intensified once the electric current is applied, and the electrodes remain in contact with both the liquid metal and the acid, until the liquid metal completely permeates the electrodes with a thin coating. Due to surface tension effects, bubbles stick at the interface and are dragged away when the liquid metal is set into motion. The schematic representation of the location of the gas bubbles between the interface of the liquid metal, and the hydrochloric acid is shown in Figure 1.3a). The white dots observed in Figure 1.3b) are the bubbles used as tracers that help to track the dynamics of the flow optically. In addition, Figure 1.3b) shows a picture of the full experimental flow domain when a DC current of 500 mA is applied in the thin liquid metal layer. The arrows are superimposed to indicate the recirculation of the flow, sketching the flow patterns and giving an idea of the size of the different regions. Visualization reveals the formation of a symmetrical structure relative to $y-$axis, consisting of two external recirculation zones (highlighted with white arrows) flowing in counter-clockwise and clockwise directions on the left and right sides of the domain, respectively. Nested within these recirculation zones, a steady vortex dipole is found (red arrows) which presents opposite sense of circulation with respect to the external vortices. This structure originates two stagnation points (represented by white crosses in Figure 1.3b) located on the symmetry axis. Furthermore, near the center of the vortex dipole, a low velocity zone is formed in the region of maximum magnetic field strength (green square).

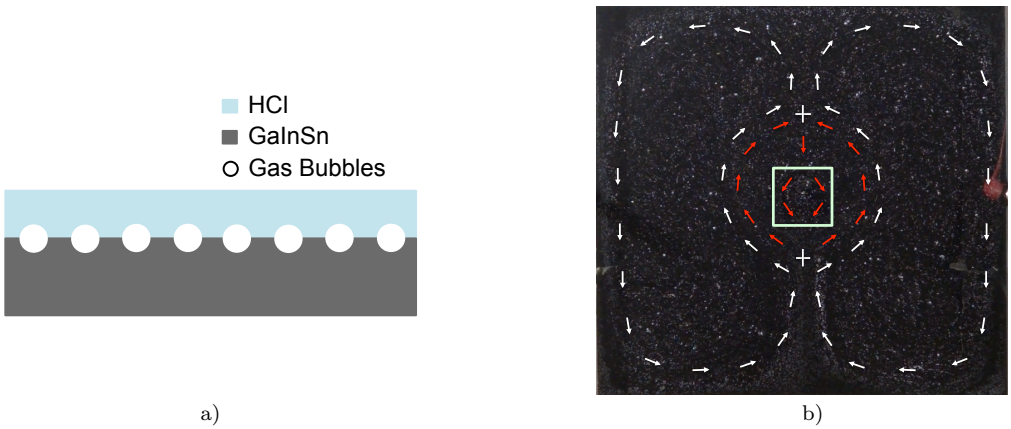

a) b)

Figure 1.3: a) Localization of gas bubbles at the interface of liquid metal and hydrochloric acid. b) Experimental picture of the flow domain in a thin liquid metal layer driven by a non-uniform Lorentz force. Arrows indicate the global flow circulation, and the green square denotes the position of the permanent magnet that lies underneath.

The optical visualizations were repeated for different experimental conditions, noting the same qualitative behavior of the flow, only with different elongation and internal vortex size. The experimental visualizations were recorded with a high definition Sony DSC-WX80 camera, with a resolution of 1920×1080 at 30 fps and "Optical SteadyShot" image stabilization, placed in the center of the container, normal to the fluid plane (see Figure 1.1b). As can be seen from the experimental measurements that will be discussed below, the analysed flow presents very low velocities, characteristic of the creeping flow regime.

1.2 Measurement techniques

The experimental measurements of the velocities produced by Lorentz forces in the liquid metal layer were carried out using two different techniques. Since the working fluid is opaque, the Ultrasound Doppler Velocimetry (UDV) technique was used to measure the bulk velocity profiles at 3.5 mm height of the liquid metal layer. At this height, the measurement errors produced by the bubbles in the top surface of the liquid metal, and the notch formed between the acrylic wall of the container and the liquid metal, are reduced. In addition, velocity measurements on the upper surface of the liquid metal (at 5.5 mm height) were performed with the Particle Image Velocimetry (PIV) technique using the bubbles as tracers.

1.2.1 UDV technique

UDV technique is a measurement method used in the areas of physics and engineering. In basic science, the method is employed in the analysis of various problems of fluid dynamics with opaque liquids (Takeda, 1986, 1991, 1995). The UDV technique has been used both to measure the flow velocity of liquid gallium contained in a rotating cylinder (Brito et al., 2001) and to reconstruct the velocity fields of a flow pattern produced by magnetic forces in a liquid metal at room temperature (Nauber et al., 2013). This measurement method has the advantage that can be used in an invasive (see Andreev et al. (2009)) or non-invasive way, as in the research presented by Cramer et al. (2004). For this study, the UDV method uses a transducer that functions as an emitter and receiver of information, sending a cone-shaped ultrasonic beam through the working fluid and continuously collecting echoes emitted from the targets, in this case the oxidized particles of liquid metal. With the emitting frequency of each ultrasonic wave and the delay time of each one, it is possible to calculate a velocity component of all of the targets that are present in the path of the beam. The calculated velocity component is always parallel to the beam emitted by the ultrasonic transducer (Signal Processing, 2015). In the experiments, the velocity profiles along the $y-$axis for several fixed positions in the $x-$axis (that run perpendicular to the applied electric current), are obtained through the DOP3010 ultrasonic doppler velocimeter connected to a TR0405LS transducer that has an emitting frequency of 4 MHz, and an acoustic active diameter of 5 mm. The transducer is placed outside the acrylic container, perpendicular to the walls (see Fig. 1.4). In order

to get a good contact between the transducer and the wall, an ultrasonic gel is placed between them in order to improve their contact and guarantee path for the ultrasonic waves. The ultrasonic beam emitted by the transducer measures along a 600 mm length, and its opening angle is 2.21° (Signal Processing, 2015). The important features used in the DOP3000 program for post-processing were: a pulse repetition frequency $PRF = 15$ MHz to measure maximum velocities of $v_{max} = 11.2$ mm/s, and a depth of $d = 328$ mm that allows to observe the echo produced by the second container wall.

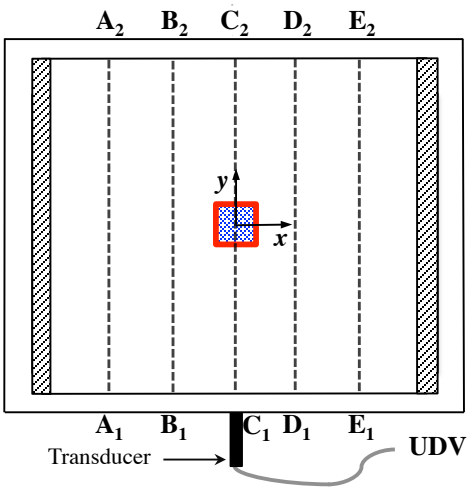

Figure 1.4: The sketch indicates the positions in which the transducer is alternately placed to take the different velocity profile measurements for five values of x.

The center of the transducer was always placed at a fixed height of $z = 3.5$ mm from the bottom of the liquid metal layer, while the length of the transducer was located perpendicular to the wall. Taking into account the origin of the geometric coordinates and the thickness of the acrylic walls of 1.2 cm, the positions x and y, in centimeters, at which the transducer is placed are shown in Table (1.1). Measuring the same velocity profile in opposite walls guarantees reliable measurements of the velocity component, in spite of the divergence of the acoustic beam.

The velocity readings are taken positive when the fluid moves away from the transducer, and negative if it is moving towards the transducer. It is important to mention that the velocity profile measurements were performed alternately; first, the velocity measurement was done by placing the transducer in position $\mathbf{A}_1$, and then in position $\mathbf{A}_2$ (see Fig. 1.4). In both cases, the measurements start from a fluid at rest, and the beginning and end time of the recorded data does not vary. This same procedure was carried out for the measurements of profiles **B**, **C**, **D** and **E**. Moreover, velocity measurements, over time along the y-axis for a fixed x-value, can also be obtained with the UDV technique.

Figure 1.5 shows the contour map of the velocities in $y-$axis obtained along time when

Position	x (cm)	y (cm)
$\mathbf{A}_1$	-8.35	-13.7
$\mathbf{A}_2$	-8.35	13.7
$\mathbf{B}_1$	-4.15	-13.7
$\mathbf{B}_2$	-4.15	13.7
$\mathbf{C}_1$	0	-13.7
$\mathbf{C}_2$	0	13.7
$\mathbf{D}_1$	4.15	-13.7
$\mathbf{D}_2$	4.15	13.7
$\mathbf{E}_1$	8.35	-13.7
$\mathbf{E}_2$	8.35	13.7

Table 1.1: Positions of the transducer to take the measurements of the velocity profiles.

the flow pattern reached a steady state for an experiment with the configuration shown in Figure 1.1 where a direct current of 350 mA was applied. For this map, values near to the wall were deleted owing to the generation of noise produced by the difference in the speed of sound of the acrylic walls and the liquid metal at the start and end of the profiles. Initially, this figure shows small values that are increasing positively until reaching a maximum value approximately between $y = 80$ and $y = 100$. It immediately begins to decrease until obtaining maximum negative values. Finally, positive values of the velocity are observed in the right region. This contour map can be better analyzed by looking at Figure 1.6, here, the $v-$component velocity profiles are shown along the entire $y-$axis of the container with the transducer placed in the center of the container ($x = 0$). For each one of the profiles of Figure 1.6, 100 steady state profiles were averaged taken the readings with the transducer located in $\mathbf{C}_1$. Green and red line are two different experiments taken the profiles at the same time with the transducer placed in the same position. The blue profile is the average of the two velocity measurements. Based on the average profile, at the ends of the profile closest to the walls and for approximate values between -7.5 and -2.7 in the $y-$axis the velocities are positive. Velocities close to the $y = 0$ axis take negative values until y is close to 23. Then, the velocities are positive again. Nearby to the walls the noise produced by the different speeds of sound between the wall and the liquid metal, is observed. The velocity measurements shown in Figure 1.6 were only taken with the transducer placed in one position, since the profiles take more accurate values close to the transducer, but not when the targets are further away from it, so for the central profiles it was decided to place the transducer in $\mathbf{C}_1$-position.

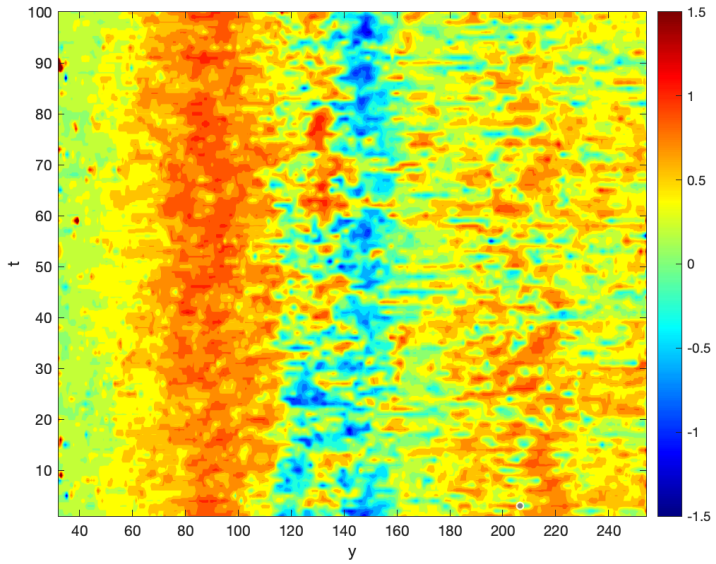

Figure 1.5: Contour map shows the velocity along y direction as a function of time. Color bar is the magnitude of the velocity in mm/s. $I = 350$ mA.

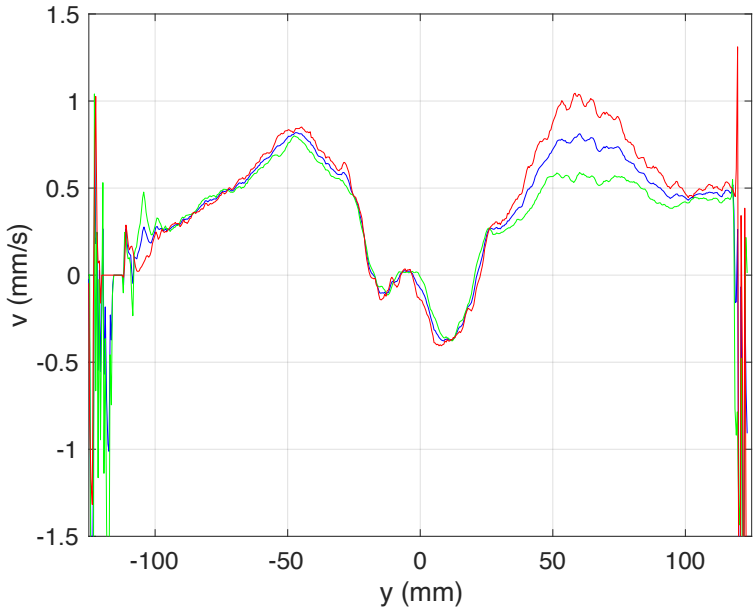

Figure 1.6: Velocity profiles of the v-component along y. Green and red lines were taken with a transducer placed in $\mathbf{C}_1$. Both profiles show different measurements in a same time interval. Blue line is the average of the two measurements. $I = 350$ mA.

The measurements of the velocity profiles off the central axis $x = 0$ were averaged to reduce the experimental error that is generated by the conical shape of the beam emitted by the transducer. The greater the distance between the beam emission and the targets from which velocity readings will be received, the greater the number of targets whose velocity is averaged. In the case of the central profile, only one of the readings was taken into account because by averaging the readings from $\mathbf{C}_1$ and $\mathbf{C}_2$, the changes in the direction of velocity in the central part were no longer observed.

Velocity profiles **B** and **D** can be observed in Figure 1.7. Red line is the average of velocity measurements with the transducer placed in B_1 and B_2, each one of this profiles were obtained by averaging 100 profiles. The measurements shown in the blue velocity profile are obtained similarly to the red profile. In both profiles, the velocities are qualitatively similar along $y-$axis and the maximum velocity is in the middle. For values from $y \approx 50$ to $y \approx 100$, red profile exhibits a non-expected qualitative behavior since the velocities close to the wall should be decreasing as shows the blue profile. This can be considered a measurement error due to the experimental technique.

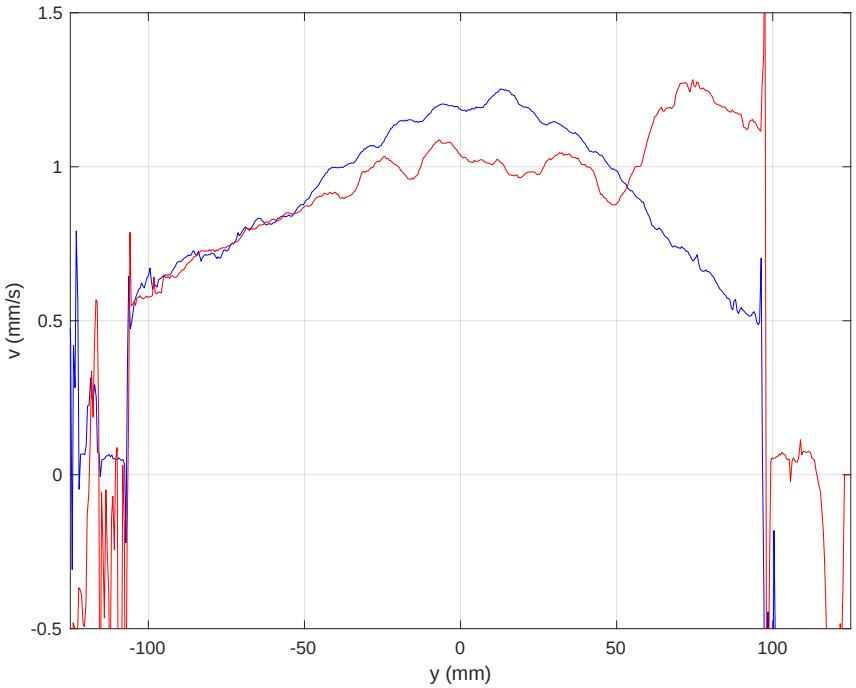

Figure 1.7: Velocity profiles of the v-component along y. Red and blue lines are the average of the measurements taken alternately with a transducer placed in B_1 and B_2 and D_1 and D_2, respectively.

In Figure 1.8 the velocity profiles **A** (red color) and **E** (blue color) can be observed. The values were obtained similarly to the profiles of Fig. 1.7 and it shows that the maximum value is in the center $y \approx 0$. Both Fig. 1.7 and 1.8 present more noise near to the walls,

but the comparison of two figures shows a quasi-symmetric flow pattern, with velocity measurements very close to each other. In addition, in this figure is clear that the velocity decay in regions close to the walls.

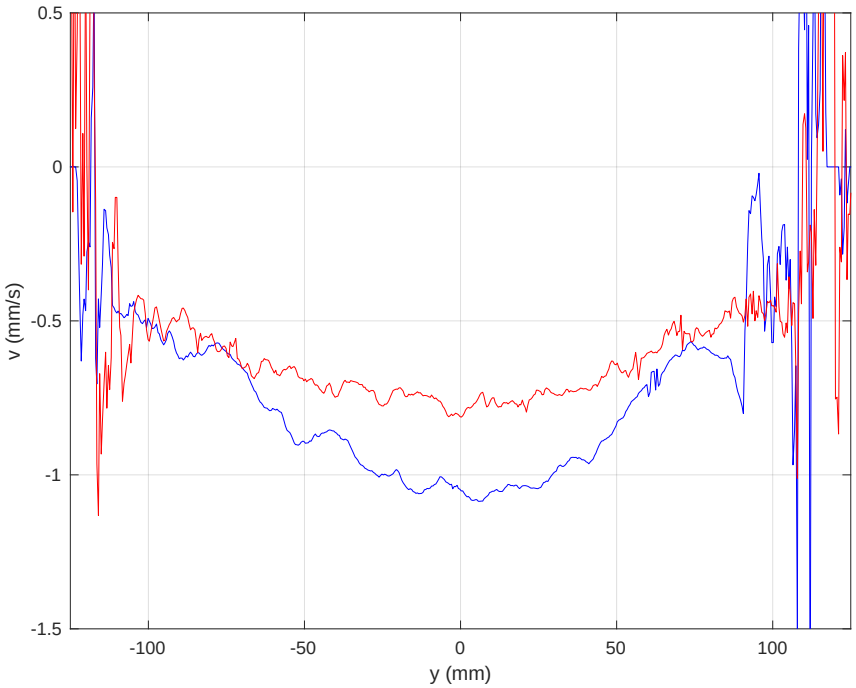

Figure 1.8: Velocity profiles of the v-component along y. Red and blue lines are the average of the measurements taken alternately with a transducer placed in A_1 and A_2 and E_1 and E_2, respectively.

Figures 1.6, 1.7 and 1.8 can be observed that the velocity direction corresponds to the orientation of flow behavior shown in Figure 1.3, in which both **B** and **D** and **A** and **E** profiles represents direction of the external vortex, and the central profile the variation of the velocity direction along y in $x = 0$.

1.2.2 PIV technique

The second method allows the measurement of the velocity field in the surface of the liquid metal through Particle Image Velocimetry, which has been recently used for the streamline visualization of the magnetohydrodynamic flow in a thin liquid metal layer driven by a moving permanent magnet (Samsami et al., 2014; Prinz et al., 2016). Similarly to this work, here we take the small gas bubbles (of size about 0.5 mm) produced at the interface between the liquid metal and the hydrochloric acid as tracers, by using a camera fixed on top and normal to the experimental device, as shown in Figure 1.1b). First, the video-camera was placed at a height of about $z = 50$ cm to record the complete surface

of the working fluid and analyse the entire flow pattern produced inside the container by a Lorentz force. Second, the central part of the fluid surface was captured to perform a more detailed analysis of the flow behavior in the quasi-stagnation zone mentioned in Section 1.1.2. For those experiments the camera was located at an approximate height of $z = 30$ cm. Both experiments can be visualized at certain time and quantified using the PIV technique.

For the analysis of the flow behavior, we used the experimental configuration mentioned in Figure 1.1 and the following characteristics in PIVLab program (Thielicke and Sontag, 2021): square interrogation areas of 64 pixels with 50% overlap in the plane $x - y$ and a standard correlation. For the results presented below, 100 steady-state data were averaged.

The PIV experimental results shown in Figure 1.9 correspond an uniformly applied direct current of 350 mA between the graphite electrodes. In Figure 1.9a), the velocity fields observed over the whole free-surface of the liquid metal, shows the formation of two external vortices that travel along the y-axis positively within values close to $x = 0$, while for values near to $x = -125$ and $x = 125$ (values where the electrodes are placed), the fluid recirculates along the y-axis in the negative direction. A internal dipole vortex is observed in the central part of this velocity fields with opposite direction of rotation with respect to the external vortex pattern. Further, a quasi-stagnation zone is observed at values around $x = 0$ and about values between $y \approx 0$ and $y \approx -20$. In fact, additional experiments were carried out in the region of the inner vortex to further analyze the flow behavior in quasi-stagnation zone (experimental results shown on the right-side of Fig. 1.9. The velocity field of the internal vortex can be observed in Figure 1.9d), in which both the stagnation points where there is a change of direction in the velocities, as well as the small velocities in the quasi-stagnation zone are observed. The streamlines shows in Figures 1.9b) and 1.9e) were obtained from the velocity fields shown in 1.9a) and 1.9d), respectively. In both Figures it can be observed the formation of the internal and external vortices. Although in Figure 1.9b), an asymmetrical flow is observed, when an analysis closer to the central zone (Fig. 1.9e) is performed, it is found that the flow pattern is mostly symmetrical about the $x-$axis.

The vorticity of the whole experimental region is shown in Figure 1.9c), where visualization reveals a symmetrical structure relative on the $y-$axis. In this picture, the most intense positive and negative vorticity is observed over the region where the magnet is placed. Here, the central zone shows the formation of nested dipole vortex whose magnitude of vorticity is similar to that of the external vortex. Finally, Figure 1.9f) shows the fluid vorticity on the central region, where we can appreciate the formation of three nested dipole vortices, that is, the external vortex on the edges of the magnet and the internal dipole vortices inside the magnet region. Specifically, the nested internal dipole is produced in the area with the strongest magnetic field and the elongation is on negative $y-$axis.

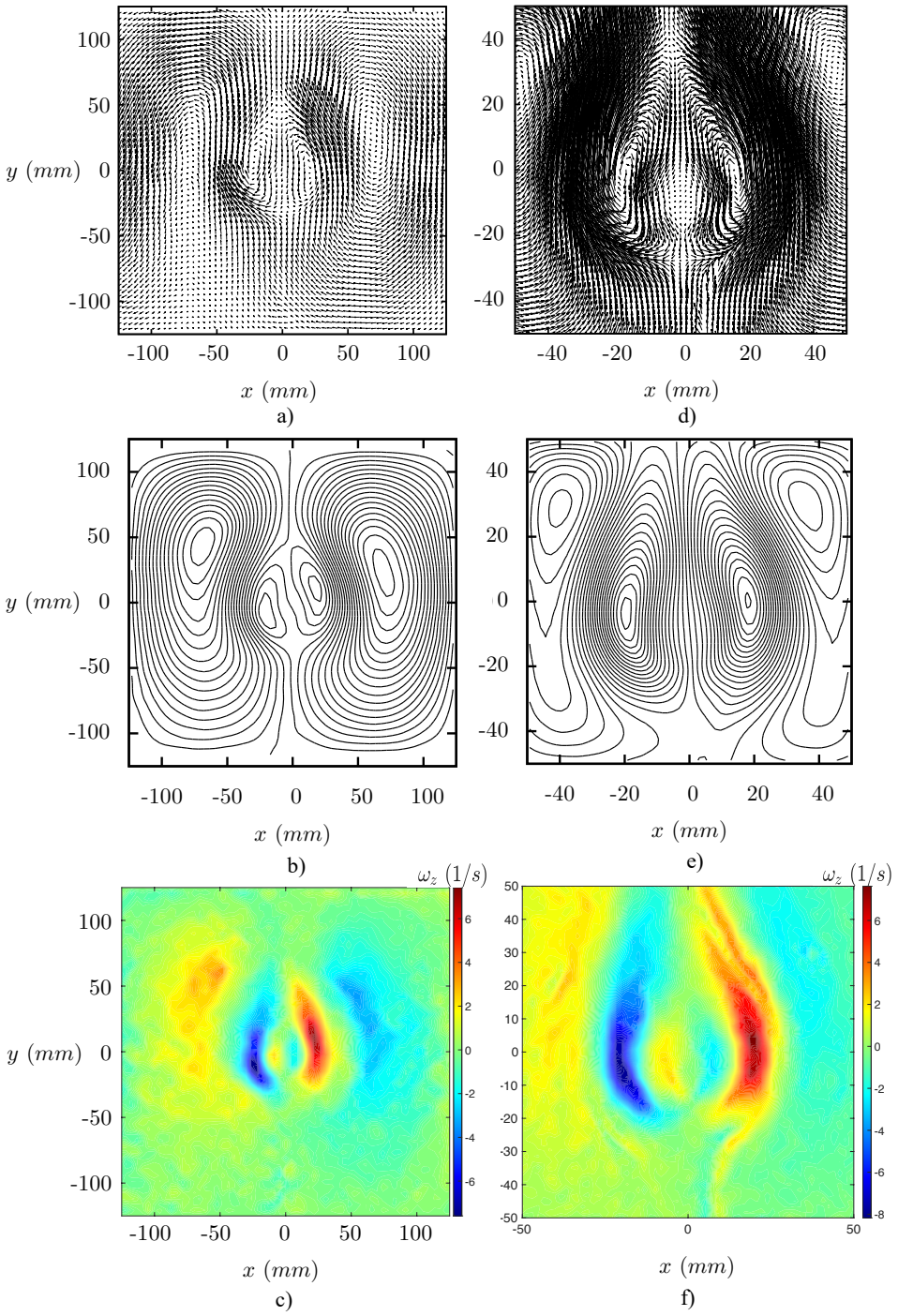

Figure 1.9: Experimental results, produced with a permanent magnet and a direct current of 350 mA, obtained with PIV technique for the whole domain (figures a, b and c) and the central zone with an area of 50 x 50 mm (figures d, e and f).

The experiments in the central domain (right-hand side of Fig. 1.9) were specifically performed to observe and analyze the flow behavior in the quasi-stagnation zone, so that the formation of two internal vortices that surround this region, is well defined. However, in the results where 100 data were averaged, only very small velocities were observed, i. e., no difference compared to the whole domain analysis was revealed. Nevertheless, when velocity fields were analyzed in this region at different instants of time, it was observed that the fluid motion not only had a reduction in the magnitude of the velocity, but also in this zone the velocities change the direction as shown in Figure 1.10, where velocity fields of four instant of time are shown. First, in Figure 1.10a) we can observe that the quasi-stagnation zone shows velocities with a positive tendency about to the $y-$axis. Second, in Figure 1.10b) it can be appreciated parallel velocities with respect to the $x-$axis. Third, the formation of two asymmetric nested vortices between internal vortices appears (see Fig. 1.10c). Four, in Figure 1.10d) the formation of a nested dipolar vortex inside the inner dipole vortex, is completely defined. This results reveals that flow pattern is composed of three nested dipole vortices. These are an external dipolar vortex, an internal dipolar vortex and a nested internal dipolar vortex as shown in Figure 1.10c). While, the left-hand side both of the external vortex and the nested-internal vortex rotate in counter-clockwise direction, the right-hand side of both vortices rotate in clockwise direction. The internal dipolar vortex rotate in opposite direction to the external dipolar vortex. More details of the formation of this vortices will be given in Chapter 3.

In order to compare the flow behavior of the quasi-stagnation region observed in the previous results, two more experiments where carried out, where we can visualize the results for an applied direct current of 650 mA in Figure 1.11 and for an applied direct current of 750 mA in Figure 1.12. The results at different instants of time of the experiment applying I =650 mA can be observed in Figure 1.11a). First, the velocities inside the quasi-stagnation zone have positive tendency about $y-$axis. Then, the velocities are almost parallel respect to the $x-$axis (see Fig. 1.11b)). Figure 1.11c) showing a reduction of velocities in the quasi-stagnation region, while Figure 1.11d) shows the formation of a symmetric internal nested dipolar vortex. In the same picture, the velocity fields reveal an elongation of the internal vortices in positive y-direction. A similar elongation of the internal vortices appears in the experimental results where we applied a current of 750 mA. In this visualizations, first, a reduction of velocities is observed in Figure 1.12a). Then in the quasi-stagnation zone of Figure 1.12b), positive $y-$direction velocities appear. Finally, in Figures 1.12c) and 1.12d), a symmetric internal nested dipolar vortex appear.

From the previous experimental results we can conclude that the motion of the liquid metal produced by Lorentz forces present a flow pattern formed by six vortices, two external vortices, two internal vortices and a nested internal dipolar vortex. In fact, the results presented in Figure 1.6 where we can observe five direction changes of velocity, in agreement with the observations shown in the PIV measurements.

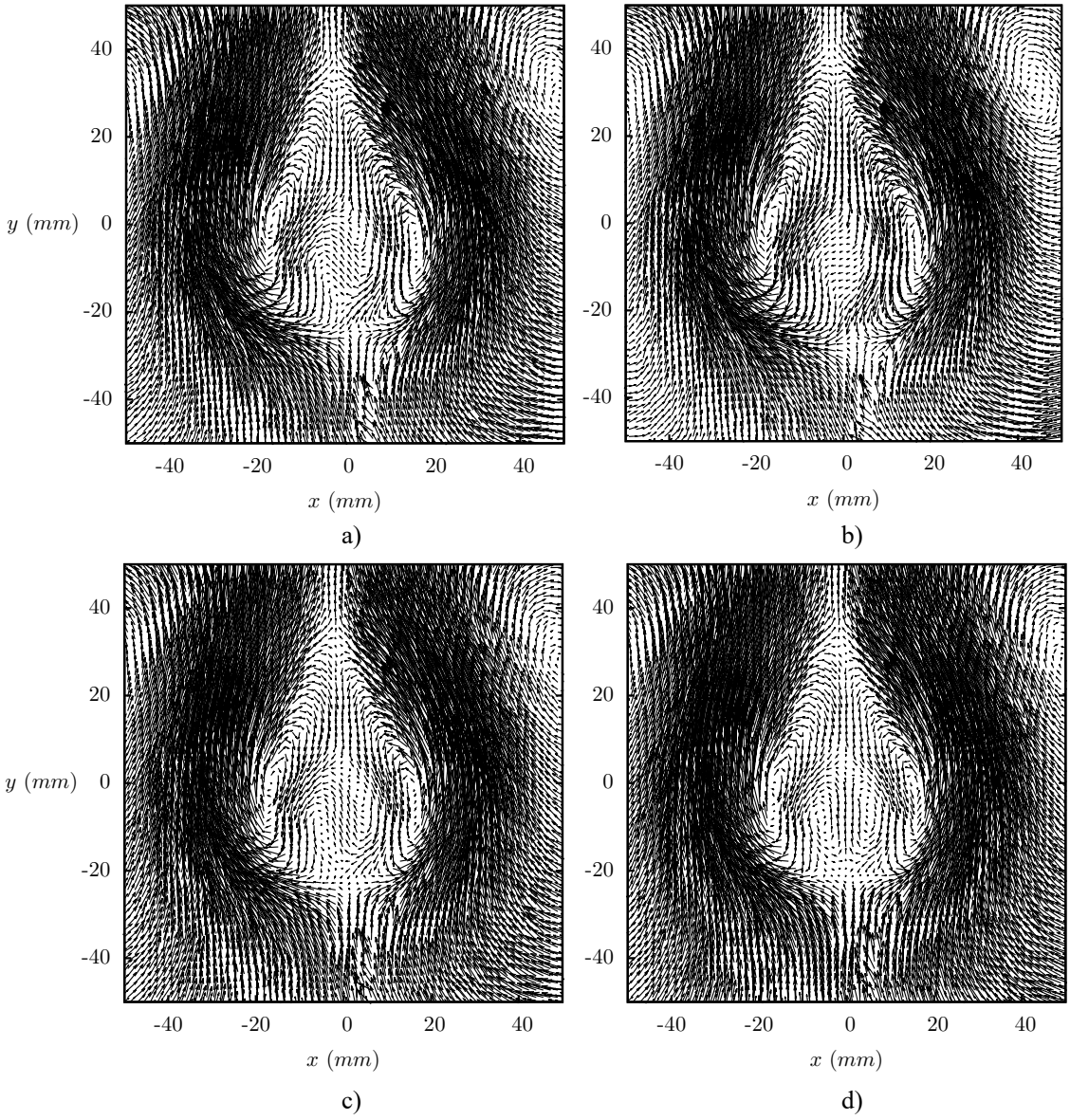

Figure 1.10: Four subsequent time instants of the PIV central experiment to analyze the quasi-stagnation zone. Applied electric direct current of 350 mA.

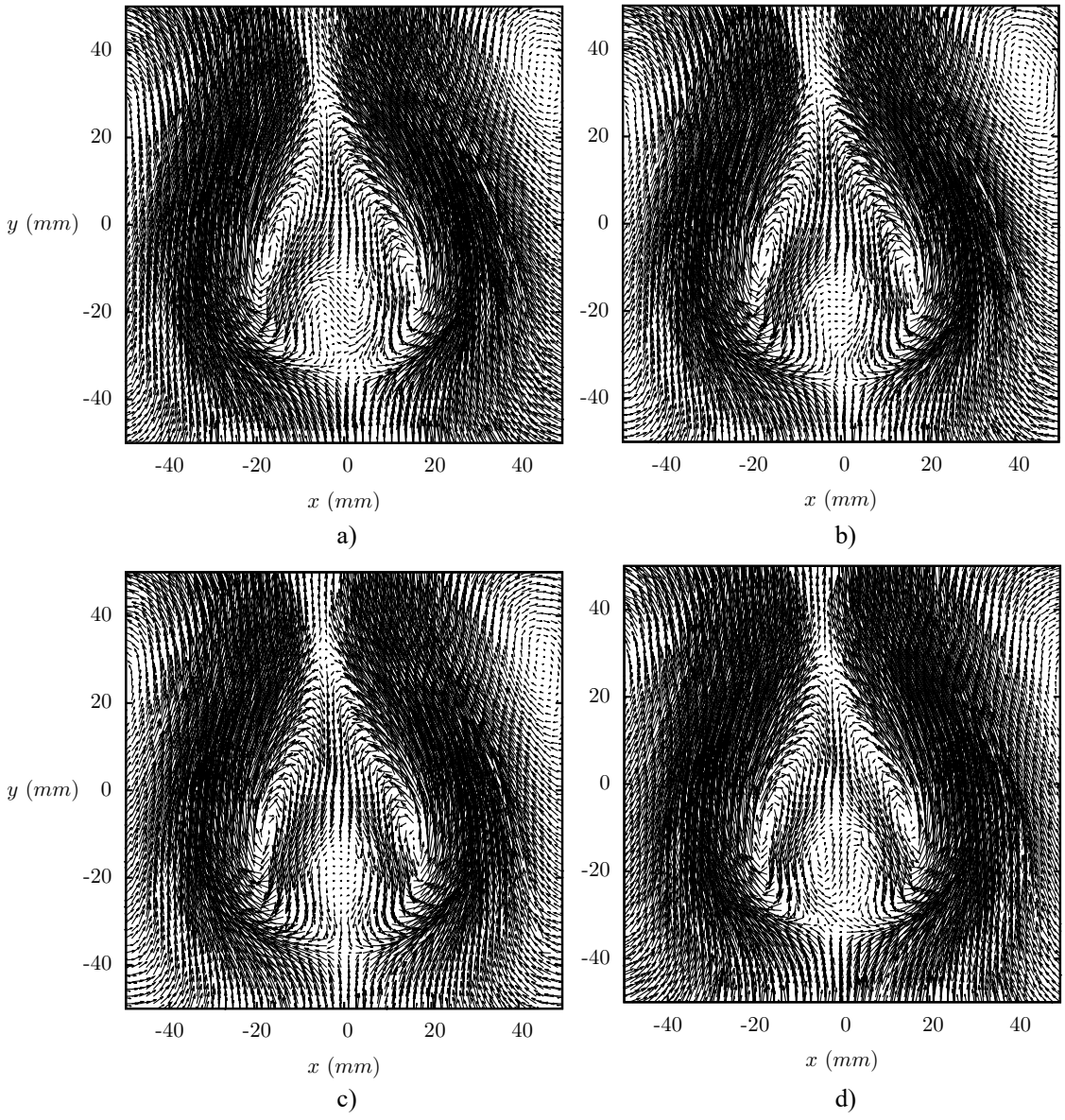

Figure 1.11: Four subsequent time instants of the PIV central experiment. Applied direct electric current of 650 mA.

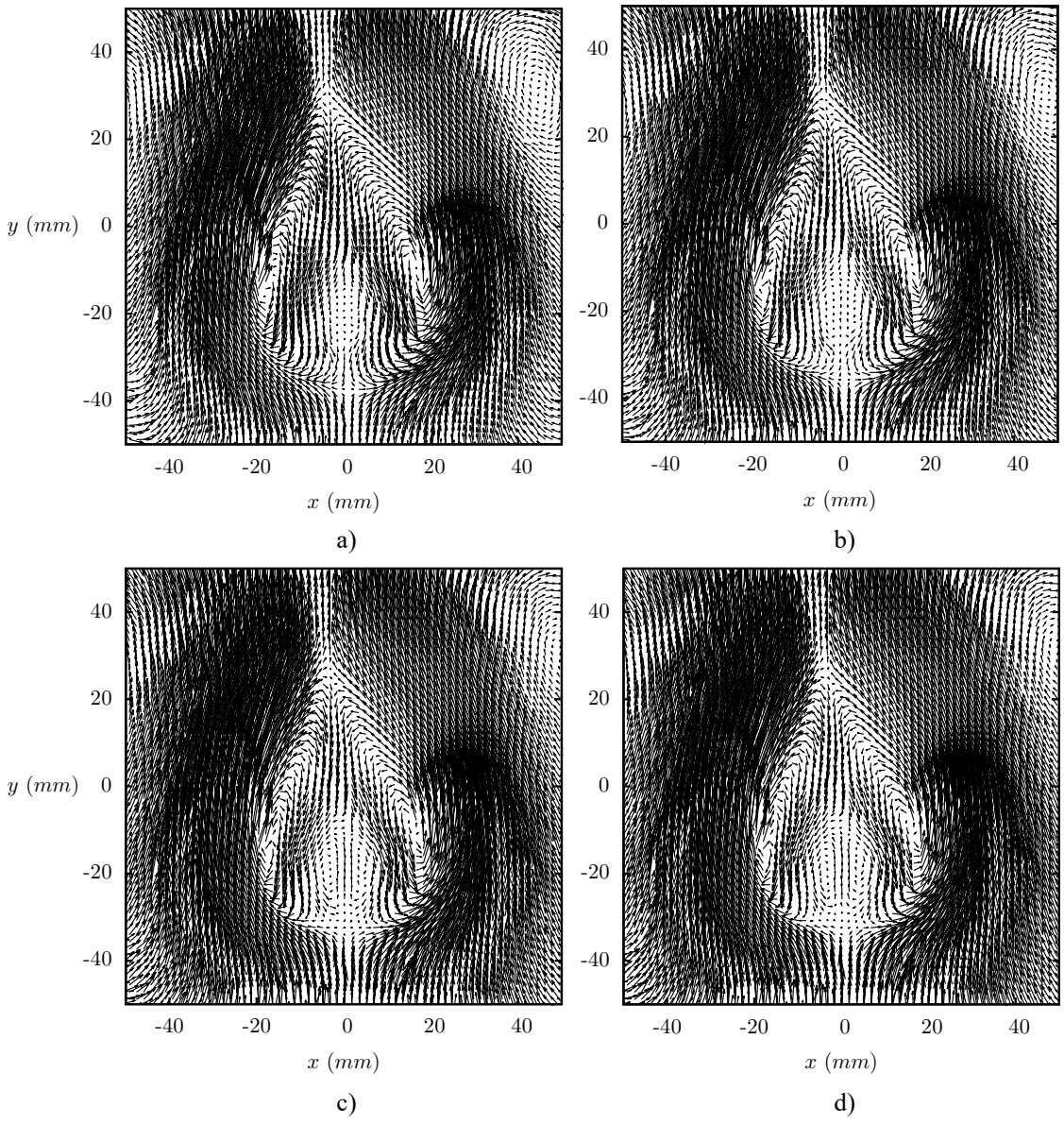

Figure 1.12: Four subsequent time instants of the PIV central experiment. Applied direct electric current of 750 mA.

Chapter 2

Two-dimensional analytical model

In this chapter, we establish the basic MHD equations from the coupling of the fluid mechanics with electromagnetic field equations. Particularly, we present the non-dimensional MHD equations in a purely two-dimensional approach. From this set of equations, an analytical solution is found for small Reynolds and Hartmann numbers of order 10. The results from this analytical solution are presented.

2.1 Background

The governing equations that describe the flow of an incompressible, electrically conducting fluid under the influence of magnetic fields involve the fundamental equations of fluid dynamics, as the continuity and Navier-Stokes equations, coupled with the Maxwell equations, Ohm's law and the equation for the Lorentz force. The fundamental MHD equations can be established in the so-called $\phi-$formulation, which implements the electric potential as electromagnetic variable; $j-$ formulation, based on the induced electric current density, proposed by Smolentsev et al. (2010), or $B-$formulation, based on the induced magnetic field, which is used in the present work.

2.1.1 Equations of fluid mechanics

From the fluid mechanics point of view, the most important physical quantities that define a fluid flow in space and time, are the density, viscosity, pressure, velocity and, temperature (Gary Leal, 2007). In several practical applications, both gases and liquids can be considered as incompressible fluids, which means that their density is constant. In particular, the eutectic GaInSn alloy used in the experimental conditions presented in this work can be assumed as incompressible. Thus, the mass conservation equation can be expressed as:

$$\nabla \cdot \mathbf{u} = 0, \tag{2.1}$$

where $\mathbf{u}$ is the velocity field. On the other hand, the liquid metal is a Newtonian fluid whose motion can be described by the Navier-Stokes equation, namely,

$$\rho \left(\frac{\partial \mathbf{u}}{\partial t} + (\mathbf{u} \cdot \nabla)\mathbf{u} \right) = -\nabla P + \eta \nabla^2 \mathbf{u} + \mathbf{f}, \tag{2.2}$$

where ρ, η, P, $\mathbf{f}$ are the mass density and dynamic viscosity of the fluid, pressure and external body forces, respectively. In the present case the external force for an electrically conducting fluid interacting with an electromagnetic field, is the so-called Lorentz force, expressed by $\mathbf{f} = \mathbf{j} \times \mathbf{B}$, where $\mathbf{j}$ is the electric current density, and $\mathbf{B}$ is the applied magnetic field. Then, the Navier-Stokes equation is rewritten as

$$\rho \left(\frac{\partial \mathbf{u}}{\partial t} + (\mathbf{u} \cdot \nabla)\mathbf{u} \right) = -\nabla P + \eta \nabla^2 \mathbf{u} + \mathbf{j} \times \mathbf{B}. \tag{2.3}$$

Additionally, energy conservation equation for a Newtonian fluid with electromagnetic interactions, takes the form:

$$\rho C_P \left(\frac{\partial T}{\partial t} + (\mathbf{u} \cdot \nabla)T \right) = \nabla \cdot (k \nabla T) + \frac{\mathbf{j}^2}{\sigma} + \Phi_\nu, \tag{2.4}$$

where C_P is the heat capacity at constant pressure, T the temperature, k the thermal conductivity, σ the electric conductivity of the medium, and Φ_ν the viscous dissipation function. The second term of the right-hand side of Equation (2.4) is the Joule dissipation owing to the electric currents circulating in the fluid. Since the density is considered constant, the Equation (2.4) is decoupled from the Equations (2.1) and (2.3), hence, the energy conservation equation (2.4) is not considered in this work. Evidently, Lorentz force appears in the Navier-Stokes equation, and introduces additional electromagnetic variables. For completing the system of equations, we have to consider the Maxwell equations and the Ohm's law which will be described in the next Subsection.

2.1.2 Maxwell equations

The laws of electromagnetism that describe the electromagnetic fields in different media can be mathematically expressed through the so-called Maxwell equations. These equations, together with the Lorentz force equation, establish the interactions of electromagnetic fields. In a homogeneous, isotropic and linear medium, the macroscopic Maxwell equations are written in differential form as

$$\nabla \cdot \mathbf{E} = \frac{\rho_e}{\epsilon}, \tag{2.5}$$

$$\nabla \cdot \mathbf{B} = 0, \tag{2.6}$$

$$\nabla \times \mathbf{E} = -\frac{\partial \mathbf{B}}{\partial t}, \tag{2.7}$$

$$\nabla \times \mathbf{B} = \mu \mathbf{j} + \mu \epsilon \frac{\partial \mathbf{E}}{\partial t}, \tag{2.8}$$

where Equation (2.5) is known as Gauss' law and relates the electric field, **E**, to the total electric charge density, ρ_e, and ϵ, the electric permittivity of the medium. Gauss' law for magnetism (Eq. 2.6) expresses the non-existence of magnetic monopoles or isolated magnetic charges, where **B** is the magnetic induction. Faraday's induction law (Eq. 2.7) establishes the possibility of generating electric fields from temporal variations of the magnetic field. Ampère-Maxwell law (Eq. 2.8) states that magnetic fields can be produced by means of electric currents and time variations of the electric fields. The original Ampère's law only contemplates the first right-hand side term of the Equation (2.8), while the second term represents the displacement current, known as the Maxwell correction term, fundamental in the description of radiative phenomena. In this equation, μ is the magnetic permeability of the medium, and, for the case of liquid metals, a very good approximation is done by setting $\mu = \mu_0$, where μ_0 is the vacuum permeability (Davidson, 2001).

In addition to Maxwell equations, we obtain the conservation equation for the electric current density applying the divergence operator to the Ampère-Maxwell law (Eq. 2.8) and using Equation (2.5) to yield:

$$\nabla \cdot \mathbf{j} + \frac{\partial \rho_e}{\partial t} = 0. \tag{2.9}$$

Additionally, we have to use Ohm's law, which is a constitutive equation that relates the electric current density with both, the electric and magnetic fields present in the medium, namely, in the liquid metal layer. In the laboratory frame of reference with respect to which the fluid moves with a velocity **u**, Ohm's law is expressed as

$$\mathbf{j} = \sigma(\mathbf{E} + \mathbf{u} \times \mathbf{B}) + \rho_e \mathbf{u}, \tag{2.10}$$

where the term $\rho_e \mathbf{u}$ is called convection current.

Finally, the Lorentz force **f** in a conductive fluid medium under the presence of the electric and magnetic fields is expressed as

$$\mathbf{f} = \rho_e \mathbf{E} + \mathbf{j} \times \mathbf{B}. \tag{2.11}$$

2.1.3 MHD approximation

In order to couple the fluid dynamics equations (no relativistic and invariant to Galilean transformations) with the electromagnetic field equations (relativistic and invariant to Lorentz transformations), we make use of the MHD approximation to make them compatible. In summary, the MHD approximation is based on the following assumptions (Shercliff, 1965):

1. Fluid velocity is much smaller than the velocity of light $|\mathbf{u}| \ll c^2$, i.e., relativistic phenomena are not considered.

2. Electric fields are of the order of magnitude of induced effects by the fluid motion, namely, $\mathbf{u} \times \mathbf{B}$.

3. The phenomena considered involve only variations at low frequencies, hence the displacement current (the last term in the Equation 2.8) is negligible compared to the conduction current density $\mathbf{j}$ in Ampère-Maxwell law. Electromagnetic radiation phenomena is not considered.

Under the MHD approximation, a magnetic field invariance is established in the different reference systems. Further, the term $\rho_e \mathbf{u}$ in the Ohm's law (Eq. 2.10), the Maxwell displacement current in Ampère-Maxwell law and the electric term in the Lorentz force are negligible as a result of the assumptions. The electromagnetic field equations under the MHD approximation take the form

$$\nabla \cdot \mathbf{B} = 0, \tag{2.12}$$

$$\nabla \times \mathbf{E} = -\frac{\partial \mathbf{B}}{\partial t}, \tag{2.13}$$

$$\nabla \times \mathbf{B} = \mu_0 \mathbf{j}, \tag{2.14}$$

$$\mathbf{j} = \sigma(\mathbf{E} + \mathbf{u} \times \mathbf{B}). \tag{2.15}$$

This set of equations is well known as the electromagnetic field equations in the quasi-static approximation (Hughes and Young, 1966). Under the MHD approximation, Equation (2.9) simplifies to

$$\nabla \cdot \mathbf{j} = 0, \tag{2.16}$$

which establishes the conservation of the electric charge (Davidson, 2001). The equations for electromagnetic field (2.12 - 2.15) and the fluid mechanics Equations (2.1) and (2.3) form a complete system that can be solved for describing the behavior of an electrically conductive fluid under the presence of a magnetic field, providing suitable initial and boundary conditions are given.

2.2 Fundamental MHD equations

Equations (2.12 - 2.15) can be combined to obtain the induction equation for the magnetic field that describes the transport of magnetic field by convection and diffusion (Müller and Bühler, 2001). First, we substitute the electric field $\mathbf{E}$ obtained from Ohm's law (Eq.

2.15) into the Equation (2.13); Faraday's law (Eq. 2.14) is used to eliminate the electric current density $\mathbf{j}$, considering Equation (2.12) and that the fluid is incompressible (Eq. 2.1). The resulting expression of the transport of magnetic field is

$$\frac{\partial \mathbf{B}}{\partial t} + (\mathbf{u} \cdot \nabla)\mathbf{B} = \lambda \nabla^2 \mathbf{B} + (\mathbf{B} \cdot \nabla)\mathbf{u}, \tag{2.17}$$

where $\lambda = 1/\mu_0 \sigma$ is the magnetic diffusivity, which is a property of the conducting medium. In order to solve the system of equations for the experimental conditions presented in the Chapter 1, we will express in dimensionless form the Equations (2.1) and (2.3). Particularly, in Equation (2.3), the Lorentz force generates fluid motion as a result of the interaction of the electric current with the magnetic field in the liquid metal. According to Faraday's induction law, when the eutectic liquid metal has a relative motion with respect to the applied magnetic field, an electromotive force, that induces the circulation of an electric current in the liquid metal, is generated. Therefore, in the GaInSn alloy layer there is a total electric current density, which is the applied current plus the induced current

$$\mathbf{j} = \mathbf{j}^0 + \mathbf{j}^i, \tag{2.18}$$

where $\mathbf{j}^0$ and $\mathbf{j}^i$ are the applied and induced electric currents, respectively. In accordance with Ampère's law, these currents generate magnetic fields, therefore, the total magnetic field is the applied one ($\mathbf{B}^0$) plus the field induced by the current circulating in the fluid ($\mathbf{b}$), that is,

$$\mathbf{B} = \mathbf{B}^0 + \mathbf{b}. \tag{2.19}$$

The induced currents $\mathbf{j}^i$ produce electromagnetic induced forces that act in the opposite direction to the Lorentz force produced by the interaction of applied magnetic field and electric current. Therefore, while applied forces drive the motion of the fluid, induced forces act to brake it.

In order to present the dimensionless form of the governing equations, we follow the dimensionless procedure presented by Figueroa et al. (2009), which consider the parameters that can be controlled externally, such as the magnetic field strength and the applied current density, in addition to the properties of the liquid metal such as density, kinematic viscosity, magnetic permeability and electrical conductivity. Taking into account the above properties, we can present the following dimensionless variables, denoted with an asterisk:

$$\mathbf{u}^* = \frac{\mathbf{u}}{u_0}, \qquad P^* = \frac{P}{\rho u_0^2},$$

$$\mathbf{j}^* = \frac{\mathbf{j}}{j^0}, \qquad \mathbf{B}^{0*} = \frac{\mathbf{B}^0}{B_m},$$

$$\mathbf{b}^* = \frac{\mathbf{b}}{RmB_m}, \qquad x^* = \frac{\mathbf{x}}{L},$$

$$t^* = \frac{t}{L^2/\nu}, \qquad u_0^* = \frac{\nu}{L},$$

where L is the side length of the magnet, which is the characteristic length; $u_0 = \nu/L$ is the viscous velocity; $Rm = \mu_0 \sigma L U_0$ is the dimensionless parameter called magnetic Reynolds number, where $U_0 = j^0 B_m L^2/\rho\nu$ is the characteristic velocity; and B_m is the maximum magnetic field strength. When we use all these variables, the continuity, Navier-Stokes and magnetic induction equations can be expressed in dimensionless form as

$$\nabla \cdot \mathbf{u} = 0, \tag{2.20}$$

$$\frac{\partial \mathbf{u}}{\partial t} + (\mathbf{u} \cdot \nabla)\mathbf{u} = -\nabla P + \nabla^2 \mathbf{u} + Re(\mathbf{j} \times \mathbf{B}^0) + ReRm(\mathbf{j} \times \mathbf{b}), \tag{2.21}$$

$$Rm\frac{\partial \mathbf{b}}{\partial t} = \nabla^2 \mathbf{b} + (\mathbf{B}^0 \cdot \nabla)\mathbf{u} - (\mathbf{u} \cdot \nabla)\mathbf{B}^0 + Rm(\mathbf{b} \cdot \nabla)\mathbf{u} - Rm(\mathbf{u} \cdot \nabla)\mathbf{b}, \tag{2.22}$$

where

$$Re = \frac{U_0 L}{\nu}, \tag{2.23}$$

represents the Reynolds number Re, that relates the inertial forces and viscous forces, in turn, the magnetic Reynolds number Rm, gives an estimation of the ratio of the magnetic field induced by the fluid motion and the applied external field B^0. In most liquid metals flows Rm is very small, i.e., Rm is much less than unity, which means that the magnetic field induced by the fluid motion is much smaller than the applied magnetic field. This assumption reduces Equations (2.21) and (2.22) so that the governing equations that describe the motion of a viscous, incompressible and electrically conductive fluid under the presence of a magnetic field are

$$\nabla \cdot \mathbf{u} = 0, \tag{2.24}$$

$$\frac{\partial \mathbf{u}}{\partial t} + (\mathbf{u} \cdot \nabla)\mathbf{u} = -\nabla P + \nabla^2 \mathbf{u} + Re(\mathbf{j} \times \mathbf{B}^0), \tag{2.25}$$

$$\nabla^2 \mathbf{b} = (\mathbf{u} \cdot \nabla)\mathbf{B}^0 - (\mathbf{B}^0 \cdot \nabla)\mathbf{u} \tag{2.26}$$

$$\nabla \cdot \mathbf{b} = 0, \qquad \nabla \times \mathbf{b} = \frac{1}{N}\mathbf{j}^i, \tag{2.27}$$

$$\nabla \cdot \mathbf{B}^0 = 0, \qquad \nabla \times \mathbf{B}^0 = 0, \tag{2.28}$$

where N is the interaction parameter or Stuart number, which estimates the ratio of Lorentz forces to inertial forces, and is given by

$$N = \frac{\sigma L B^{02}}{\rho U_0}. \tag{2.29}$$

This parameter can also be expressed as $N = Ha^2/Re$. Equations (2.27) and (2.28) are the result of the substitution of Equations (2.18) and (2.19) into Gauss' law and Ampère's law.

2.3 Two-dimensional approximation

In fluid dynamics, several flow situations can be analyzed using two-dimensional approximations, when the variations in the direction normal to the plane of motion is very small. For instance, a fluid flow that is confined in a Hele-shaw cell can be experimentally analyzed using a two-dimensional approach, since the separation between the two plates of the cell is very small compared to the length and width of the cell(Klaasen et al., 2014). Also, in fluid motion generated by electromagnetic forces under strong magnetic fields, the velocity component in the same direction in which the magnetic field is applied can be neglected, since it is almost suppressed due to magnetic effects (Sommeria, 1988, 1986). On the other hand, the geometric confinement of fluids in very thin layers, in which the height of the fluid layer is much smaller than the other dimensions of the container, promotes the damping of fluid motion in the normal direction to the layer. Therefore, this assumption allows modeling the fluid behavior using a quasi-two-dimensional approach. In Afanasyev and Korabel (2006), the authors mentioned that, although the quasi-two-dimensional model is a simplification, the results of the approximation are in very good agreement with those obtained experimentally. In previous investigations, theoretical and experimental studies of flows produced by electromagnetic forces in thin layers of electrolytes and liquid metals have been performed. The behavior of electromagnetically driven flows can be modeled analytically or numerically in two-dimensions (Salas et al., 2001; Cuevas et al., 2002) or quasi-two-dimensionally (Figueroa et al., 2009, 2011; Lara et al., 2017). Since the results of these approximations are in good agreement with the experimental observations, in this chapter, a two-dimensional model is developed and solved analytically for the case of a flow produced by electromagnetic forces under a non-uniform magnetic field in a thin liquid metal layer. In Chapter 3, we use a quasi-two-dimensional approximation to obtain numerical solutions that can describe more features of the flow under different conditions (Lara et al., 2017). In order to obtain a purely two-dimensional approximation, the dependence on the $z-$coordinate is neglected, so that the velocity field is

$$\mathbf{u} = [u(x, y, t), v(x, y, t), 0]. \tag{2.30}$$

In this approximation, we consider only the component of the magnetic field normal to the $(x - y)$ plane. Therefore, the applied and induced magnetic fields are, respectively, represented by

$$\mathbf{B}^0 = [0, 0, B_z^0(x, y)], \tag{2.31}$$

$$\mathbf{b} = [0, 0, b_z(x, y)]. \tag{2.32}$$

From Ampère's law and the Equation (2.27b), we can calculate the induced currents in the same plane of the flow. So that the total current density (applied plus induced) is expressed in dimensionless terms as

$$\mathbf{j} = [1 + j_x^i(x, y, t), j_y^i(x, y, t), 0], \tag{2.33}$$

where the unit term in the $x-$component represents the applied current density, normalized with its magnitude. From these assumptions, the two-dimensional model that represents the flow of a liquid metal layer due to the interaction of an applied current and a localized magnetic field can be reduced to (Figueroa, 2006):

$$\frac{\partial u}{\partial x} + \frac{\partial v}{\partial y} = 0, \tag{2.34}$$

$$\frac{\partial u}{\partial t} + u\frac{\partial u}{\partial x} + v\frac{\partial u}{\partial y} = -\frac{\partial P}{\partial x} + \frac{\partial^2 u}{\partial x^2} + \frac{\partial^2 u}{\partial y^2} + Rej_y^i B_z^0, \tag{2.35}$$

$$\frac{\partial v}{\partial t} + u\frac{\partial v}{\partial x} + v\frac{\partial v}{\partial y} = -\frac{\partial P}{\partial y} + \frac{\partial^2 v}{\partial x^2} + \frac{\partial^2 v}{\partial y^2} - ReB_z^0 - Rej_x^i B_z^0, \tag{2.36}$$

$$\frac{\partial^2 b_z}{\partial x^2} + \frac{\partial^2 b_z}{\partial y^2} - u\frac{\partial B_z^0}{\partial x} - v\frac{\partial B_z^0}{\partial y} = 0. \tag{2.37}$$

Once b_z is determined, from Ampère's law (Eq. 2.27b) the components of the induced current can be calculated by

$$j_x^i = N\frac{\partial b_z}{\partial y}, \qquad j_y^i = -N\frac{\partial b_z}{\partial x}. \tag{2.38}$$

The closed system of Equations (2.34 - 2.38) will now be solved analytically. In the following section, the procedure for obtaining the analytical solution is presented, and later the numerical strategy to solve the model is also described.

2.4 Analytical model

Analytical models are a basic tool in fluid mechanics, since they allow reproducing, under certain conditions, different physical features of the flows. Under two-dimensional approximations, Moffatt and Toomre (1967) and Cuevas et al. (2002) studied analytically the magnetic braking in electrically conducting fluids. The authors studied the effect of a transverse magnetic field on the development of a jet, and on steady streaming vortices generated by oscillatory viscous flow over a wavy wall, respectively. In both cases, it was found that the magnetic field tends to annihilate the fluid motion. Another example in which an analytical solution is developed for a boundary layer flow under an applied magnetic field was presented by Cuevas and Ramos (1997). The authors demonstrated that, if the magnetic field is very intense, the fluid motion is damped until being completely annihilated. On the other hand, analytical models have also been used as fundamental tools for understanding the flow dynamics generated in liquid metals (Pothérat et al., 2000) and electrolytes (Pérez-Barrera et al., 2016) by means of electromagnetic forces. In all these studies, the mathematical treatments are directed to analyze specific flow characteristics since, as it is well known, applicability of analytical solutions is limited to simplified situations of the fluid dynamics and electromagnetic equations, thus, they do not allow to explore completely the flow behavior. Nevertheless, they are a valuable tools for the understanding of the basic physics of different phenomena, as well as a validation tool for more complex solutions, such as those provided by numerical codes. In this project, we developed an analytical model in two dimensions for describing the flow generated in a liquid metal layer by the interaction of a direct electric current and the magnetic field produced by a single permanent magnet. The governing equations (Eqs. 2.34 - 2.38) are solved through the perturbation method; first, for it is required to rewrite the Equations (2.35) and (2.36) using the definition of vorticity:

$$\omega_z = \frac{\partial v}{\partial x} - \frac{\partial u}{\partial y}, \tag{2.39}$$

where ω_z is the $z-$component of the vorticity. In this way, the momentum equation can be written as the vorticity transport equation, namely,

$$\frac{\partial \omega_z}{\partial t} + u\frac{\partial \omega_z}{\partial x} + v\frac{\partial \omega_z}{\partial y} = \frac{\partial^2 \omega_z}{\partial x^2} + \frac{\partial^2 \omega_z}{\partial y^2} - Re\frac{\partial B_z^0}{\partial x} - Re\frac{\partial (j_x^i B_z^0)}{\partial x} - Re\frac{\partial (j_y^i B_z^0)}{\partial y}. \tag{2.40}$$

Applying the electric charge conservation $\nabla \cdot \mathbf{j}^i = 0$, in Equation (2.40), the expression takes the form

$$\frac{\partial \omega_z}{\partial t} + u\frac{\partial \omega_z}{\partial x} + v\frac{\partial \omega_z}{\partial y} = \frac{\partial^2 \omega_z}{\partial x^2} + \frac{\partial^2 \omega_z}{\partial y^2} - Re\frac{\partial B_z^0}{\partial x} - Re\left(j_x^i \frac{\partial B_z^0}{\partial x} + j_y^i \frac{\partial B_z^0}{\partial y}\right). \tag{2.41}$$

In the last term of Equation (2.41), the induced currents are replaced by Equations (2.38), so that the vorticity equation is given by

$$\frac{\partial \omega_z}{\partial t} + u\frac{\partial \omega_z}{\partial x} + v\frac{\partial \omega_z}{\partial y} = \frac{\partial^2 \omega_z}{\partial x^2} + \frac{\partial^2 \omega_z}{\partial y^2} - Re\frac{\partial B_z^0}{\partial x} - Ha^2\left(\frac{\partial b_z}{\partial y}\frac{\partial B_z^0}{\partial x} - \frac{\partial b_z}{\partial x}\frac{\partial B_z^0}{\partial y}\right). \quad (2.42)$$

On the right-hand side term of this equation, the third term represents the applied Lorentz force that produces the fluid motion, while the terms in parenthesis represent the induced electromagnetic forces acting in the opposite direction of the produced motion.

2.4.1 Applied magnetic field

In Equation (2.42), the magnetic field is modeled using the equation provided by Good and Nelson (1971), which describes the field produced by a point magnetic dipole located at the origin of the reference system. Since a two-dimensional model is considered, we only take into account the dominant contribution of the magnetic field produced by the ideal dipole in the normal direction to the $x-y$ plane, in which the fluid layer is located. Then, the two-dimensional point magnetic dipole can be expressed in dimensional form as

$$\mathrm{B}_z^0(x,y) = \frac{\mu_0}{2\pi}\frac{m}{x^2+y^2} + \mu_0 m\delta(x)\delta(y), \quad (2.43)$$

where B_z^0 is the $z-$component of the magnetic field, μ_0 is the magnetic permeability and m denotes the dipole moment pointing in the $z-$direction. The first right-hand side term in Equation (2.43) represents the contribution of the magnetic field outside the origin where the dipole is located, while the second term considers the value of the field at the origin. The Dirac delta function takes into account the singularity of the dipole field. The magnetic field B_z^0 written in dimensionless form is normalized by $\mathrm{B}_m = \mu_0 m/L^2$, where L is a characteristic length. For practical purposes, we assume that is $\mathrm{B}_m = 1$ so that the characteristic length is chosen as $L = \sqrt{\mu_0 m}$ (Cuevas et al., 2006). Therefore, the dimensionless magnetic field for a point dipole at the origin is

$$\mathrm{B}_z^0(x,y) = \frac{1}{2\pi}\frac{1}{x^2+y^2} + \delta(x)\delta(y). \quad (2.44)$$

In Equation (2.44) only the second right-hand side term gives a non-zero contribution to the magnetic field value. On the other hand, note that this equation does not fulfill the curl-free condition (Eq. 2.28b), since it only considers the normal component of the magnetic field. However, Equation (2.44) provides a good description of the field for a finite magnetic dipole.

2.4.2 Boundary and initial conditions

Physically, the working fluid is contained in a rectangular box. Nevertheless, we assume that the fluid is in an infinite domain to simplify the mathematical problem. This assumption allows us to consider that far away from the origin, the magnetic field produced

by the dipole is negligible, therefore, there is no electromagnetic force to produce motion, and then the fluid remains static. Under this assumption, we consider that far away from the origin, the induced magnetic field is zero. Then at infinity:

$$u \to 0, \quad v \to 0, \quad P \to \text{constant}, \quad b_z \to 0 \quad \text{as } x, y \to \pm\infty. \tag{2.45}$$

On the other hand, the magnetic field has a finite value at the point where the ideal dipole is located. Hence, the velocity, pressure and induced magnetic field are also finite, namely,

$$u \to \text{ finite}, \quad v \to \text{ finite}, \quad P \to \text{ finite}, \quad b_z \to \text{ finite} \quad \text{as } x, y \to 0. \tag{2.46}$$

Initially, the fluid is at rest. Therefore, the initial condition is

$$u = v = 0, \quad P = \text{constant}, \quad b_z = 0 \text{ at } t = 0. \tag{2.47}$$

2.4.3 Analytical solution

For the analytical solution, Equation (2.42) is solved using the expansions of the variables in terms of Reynolds and Hartmann parameters. Considering that the Reynolds number is very small ($Re \ll 1$) and the product of Reynolds times Hartmann is small, we can carry out the expansion of variables as

$$\xi_g = \xi_g^{(0)} + ReHa^0\xi_g^{(1,0)} + ReHa^2\xi_g^{(1,2)} + \mathcal{O}(Re^2Ha^2), \tag{2.48}$$

where ξ_g can be replaced by the velocity components (u, v), vorticity (ω_z), induced magnetic field (b_z) or pressure (P), and the superscript represents the order of approximation in each parameter. For instance, the expansion for vorticity is expressed as

$$\omega_z = \omega_z^{(0)} + ReHa^0\omega_z^{(1,0)} + ReHa^2\omega_z^{(1,2)} + \mathcal{O}(Re^2Ha^2). \tag{2.49}$$

In Equation (2.49), the terms at $\mathcal{O}(Re^2Ha^2)$ or greater can be neglected, since their contribution is very small. Therefore, we only solve for the first three terms of the series.

A. Zero-order solution

At zero-order, the vorticity satisfies

$$\frac{\partial\omega_z^{(0)}}{\partial t} + u^{(0)}\frac{\partial\omega_z^{(0)}}{\partial x} + v^{(0)}\frac{\partial\omega_z^{(0)}}{\partial y} = \frac{\partial^2\omega_z^{(0)}}{\partial x^2} + \frac{\partial^2\omega_z^{(0)}}{\partial y^2}. \tag{2.50}$$

In this case, it does not exist a source term that promotes motion of the fluid, so that it is kept at rest. Consequently, the solution at this order is

$$\omega_z^{(0)} = 0, \qquad u^{(0)} = 0, \qquad v^{(0)} = 0. \tag{2.51}$$

At $\mathcal{O}(Re^0 Ha^0)$ the solution of the pressure is a constant; and the induced magnetic field and induced currents are

$$b_z^{(0)} = 0, \qquad j_x^{i(0)} = 0, \qquad j_y^{i(0)} = 0. \tag{2.52}$$

B. First-order solution

The vorticity equation at $\mathcal{O}(ReHa^0)$ is given by

$$\frac{\partial \omega^{(1,0)}}{\partial t} = \frac{\partial^2 \omega_z^{(1,0)}}{\partial x^2} + \frac{\partial^2 \omega_z^{(1,0)}}{\partial y^2} + \frac{\partial B_z^0}{\partial x}, \tag{2.53}$$

where the last right-hand side term is a source that produces motion in the fluid. The positive sign in the derivative of the applied electromagnetic term is the result of imposing a negative magnetic field in order to reproduce an applied field with a positive and negative distribution, similar to that measured experimentally. Taking into account that only the delta function term in Equation (2.44) gives a non-zero contribution in the $z-$component of the magnetic field, we solve Equation (2.53) through the Green's function method in an infinite domain ($-\infty < x < \infty$ and $-\infty < y < \infty$) for $t > 0$, using as the initial condition $w_z^{(1,0)} = 0$ at $t = 0$ (Özişik, 1993). Then, the solution of Equation (2.44) is:

$$\omega_z^{(1,0)} = -\frac{1}{2\pi} \frac{x}{x^2 + y^2} e^{-\frac{x^2+y^2}{4t}}. \tag{2.54}$$

A similar solution is presented in Salas et al. (2001). The steady-state solution can be computed from Equation (2.54) when $t \to \infty$, which is expressed by

$$\omega_z^{(1,0)} = -\frac{1}{2\pi} \frac{x}{x^2 + y^2}. \tag{2.55}$$

Both the solution for unsteady and steady-state vorticity have a singularity at the origin that does not allow to satisfy the boundary condition shown in Equation (2.46), this feature is a consequence of the point dipole magnetic field used for the solution of Equation (2.53). Nevertheless, in the corresponding results for this section, it will be shown that, although the solution has a singularity at the origin, the analytical and experimental comparisons are in good qualitative agreement. Once the vorticity is known, we can obtain the stream function at $\mathcal{O}(ReHa^0)$ by solving the equation

$$\frac{\partial^2 \psi^{(1,0)}}{\partial x^2} + \frac{\partial^2 \psi^{(1,0)}}{\partial y^2} = -\omega_z^{(1,0)}. \tag{2.56}$$

Applying the boundary conditions (Eqs. 2.45−2.46), the solution for Equation (2.56) is

$$\psi^{(1,0)} = -\frac{x}{8\pi}\Big[1 - \ln(x^2 + y^2)\Big]. \tag{2.57}$$

Further, we can use the stream function definition

$$u = \frac{\partial \psi}{\partial y}, \qquad v = -\frac{\partial \psi}{\partial x}, \tag{2.58}$$

for obtaining the velocity components

$$u^{(1,0)} = \frac{1}{4\pi}\frac{xy}{x^2 + y^2}, \tag{2.59}$$

$$v^{(1,0)} = \frac{1}{8\pi}\left[1 - \ln(x^2 + y^2) - \frac{2x^2}{x^2 + y^2}\right]. \tag{2.60}$$

These expressions do not satisfy all the boundary conditions, since they present the same singularity at the origin derived from the applied magnetic field used for the solution of Equation (2.53). On the other hand, the condition at infinity is not satisfied due to a problem intrinsic to the approximation $Re \ll 1$ (Figueroa, 2006). For the problem we are analyzing, it is difficult to specify the region of study in which the solution is valid, and to be able to define it requires a more detailed analysis. Despite the limitations of this analytical solution, the results obtained with this approach are interesting to analyze.

The equation for pressure at $\mathcal{O}(ReHa^0)$ is given by

$$\frac{\partial^2 P^{(1,0)}}{\partial x^2} + \frac{\partial^2 P^{(1,0)}}{\partial y^2} = \frac{\partial B_z^0}{\partial y}. \tag{2.61}$$

This expression is solved analogously to Equation (2.53), resulting in

$$P^{(1,0)} = \frac{1}{2\pi}\frac{y}{x^2 + y^2}. \tag{2.62}$$

Once the velocity components are calculated, the induced magnetic field can be determined from

$$\frac{\partial^2 b_z^{(1,0)}}{\partial x^2} + \frac{\partial^2 b_z^{(1,0)}}{\partial y^2} = u^{(1,0)}\frac{\partial B_z^0}{\partial x} + v^{(1,0)}\frac{\partial B_z^0}{\partial y}. \tag{2.63}$$

Here, for simplicity, we use a Gaussian distribution for approximating the $z-$component of the applied magnetic field through the equation

$$\mathrm{B}_z^0(x, y) = \frac{n}{\pi} e^{-n(x^2+y^2)} \text{ for } n > 0, \tag{2.64}$$

since this is a good approximation of the product of the Dirac delta functions presented in Equation (2.44). Besides, Equations (2.44 and 2.64) have a similar distribution around the origin, and the integration of both expressions into the infinite domain is equal to 1. Hence, taking into account a negative magnetic field, the solution for Equation (2.63) is

$$b_z^{(1,0)} = -\frac{y}{16\pi^2(x^2+y^2)}\Big\{\big[1-n(x^2+y^2)\big]Ei\big[-n(x^2+y^2)\big] \\ -e^{-n(x^2+y^2)}\ln(x^2+y^2)\Big\}, \tag{2.65}$$

where the Ei function is defined as

$$Ei = -\int_{-\Gamma}^{\infty}\frac{e^{-t}}{t}dt, \text{ for } \Gamma > 0. \tag{2.66}$$

The induced magnetic field (Eq. 2.65) has a good behavior at infinity, but diverges at the origin, similar to the solutions of the other variables. From the solution of the induced field, and using Ampère's law (Eq. 2.38), we can calculate the induced currents at $\mathcal{O}(ReHa^0)$ as

$$j_x^{i(1,0)} = -\frac{Ne^{-n(x^2+y^2)}}{16\pi^2(x^2+y^2)^2}\Big\{\big[y^2+2ny^2(x^2+y^2)-x^2\big]\ln(x^2+y^2) \\ -e^{n(x^2+y^2)}Ei\big[-n(x^2+y^2)\big]\big[y^2+n(x^2+y^2)^2-x^2\big] \\ -2ny^2(x^2+y^2)\Big\}, \tag{2.67}$$

$$j_y^{i(1,0)} = -\frac{Nxye^{-n(x^2+y^2)}}{8\pi^2(x^2+y^2)^2}\Big\{n(x^2+y^2)+e^{n(x^2+y^2)}Ei\big[-n(x^2+y^2)\big] \\ -\big[1+n(x^2+y^2)\big]\ln(x^2+y^2)\Big\}. \tag{2.68}$$

The expressions obtained for the induced current density (Eqs. 2.67−2.68) do not satisfy the boundary condition at the origin, since its solution is derived from the induced magnetic field. However, the results for the induced current that we will be shown later, are a good qualitative representation of the phenomena at hand.

C. Second-order solution

The second part of the analytical model consists of solving Equation (2.42), considering the induced electric currents at $\mathcal{O}(ReHa^0)$. Therefore, the contribution of the vorticity at $\mathcal{O}(ReHa^2)$ is obtained through Equation (2.42), reduced to

$$\frac{\partial^2 \omega_z^{(1,2)}}{\partial x^2} + \frac{\partial^2 \omega_z^{(1,2)}}{\partial y^2} = \frac{\partial b_z^{(1,0)}}{\partial y}\frac{\partial B_z^0}{\partial x} - \frac{\partial b_z^{(1,0)}}{\partial x}\frac{\partial B_z^0}{\partial y}, \tag{2.69}$$

where the fluid motion is produced by the induced magnetic field at $\mathcal{O}(ReHa^0)$ (Eq. 2.65). However, to solve Equation (2.69), the value of $b_z^{(1,0)}$ is only replaced by

$$b_z^{(1,0)} = \frac{y}{16\pi^2(x^2+y^2)}, \tag{2.70}$$

because the second right-hand side term of Equation (2.65) is negligible with respect to the first right-hand side term of the induced magnetic field. However, the negative sign of the second term is considered in this solution. The applied magnetic field is replaced by Equation (2.64). Applying the boundary conditions (Eqs. 2.45−2.46) and the computed expressions for the applied and induced magnetic fields, the solution for the vorticity at $\mathcal{O}(ReHa^2)$ is

$$\omega_z^{(1,2)} = -\frac{nx}{32\pi^3}\left\{\frac{1}{x^2+y^2}e^{-n(x^2+y^2)} + nEi\big[-n(x^2+y^2)\big]\right\}. \tag{2.71}$$

From Equation (2.71), we can obtain the stream function at $\mathcal{O}(ReHa^2)$

$$\frac{\partial^2 \psi^{(1,2)}}{\partial x^2} + \frac{\partial^2 \psi^{(1,2)}}{\partial y^2} = -\omega_z^{(1,2)}. \tag{2.72}$$

Applying the boundary conditions (Eqs. 2.45−2.46), the solution is given by

$$\begin{aligned}\psi^{(1,2)} = \frac{xe^{-n(x^2+y^2)}}{256\pi^3(x^2+y^2)}\Big\{&1 + n(x^2+y^2)\\ &+n(x^2+y^2)\big[n(x^2+y^2)+2\big]e^{n(x^2+y^2)}Ei\big[-n(x^2+y^2)\big]\Big\}.\end{aligned} \tag{2.73}$$

Once the stream function is known, we can calculate the velocity components so that

$$\begin{aligned}u^{(1,2)} = \frac{xye^{-n(x^2+y^2)}}{128\pi^3(x^2+y^2)^2}\Big\{&-1 + n(x^2+y^2)\\ &+e^{n(x^2+y^2)}n^2(x^2+y^2)^2Ei\big[-n(x^2+y^2)\big]\Big\},\end{aligned} \tag{2.74}$$

$$\begin{aligned}v^{(1,2)} = -\frac{e^{-n(x^2+y^2)}}{256\pi^3(x^2+y^2)^2}\Big\{&3nx^4 + y^2 + ny^4 + x^2(-1+4ny^2)\\ &+e^{n(x^2+y^2)}n(x^2+y^2)^2\big[2+n(3x^2+y^2)\big]Ei\big[-n(x^2+y^2)\big]\Big\}.\end{aligned} \tag{2.75}$$

On the other hand, the induced magnetic field at $\mathcal{O}(ReHa^2)$ satisfies the equation

$$\frac{\partial^2 b_z^{(1,2)}}{\partial x^2} + \frac{\partial^2 b_z^{(1,2)}}{\partial y^2} = u^{(1,2)} \frac{\partial B_z^0}{\partial x} + v^{(1,2)} \frac{\partial B_z^0}{\partial y}, \tag{2.76}$$

where the applied magnetic field is replaced by Equation (2.64). The solution for Equation (2.76) is

$$\begin{aligned} b_z^{(1,2)} = \frac{nye^{-2n(x^2+y^2)}}{512\pi^4(x^2+y^2)} \Big\{ & 3 + 4e^{2n(x^2+y^2)} \big[-1 + n(x^2+y^2) \big] Ei\big[-2n(x^2+y^2) \big] \\ & + e^{n(x^2+y^2)} \big[4 + n(x^2+y^2) \big] Ei\big[-n(x^2+y^2) \big] \Big\}. \end{aligned} \tag{2.77}$$

Once the induced magnetic field is known, the induced current density can be calculated from Equation (2.38), resulting in

$$\begin{aligned} j_x^{i(1,2)} = \frac{nNe^{-n(x^2+y^2)(2+x^2+y^2)}}{512\pi^4(x^2+y^2)^2} \Big\{ & 3x^2 e^{n(x^2+y^2)^2} + 16y^2 e^{n(x^2+y^2)} - 11y^2 e^{n(x^2+y^2)^2} \\ & + 4nx^2y^2 e^{n(x^2+y^2)} - 4nx^2y^2 e^{n(x^2+y^2)^2} + 4ny^4 e^{n(x^2+y^2)} - 4ny^4 e^{n(x^2+y^2)^2} \\ & + 4e^{n(x^2+y^2)(2+x^2+y^2)} \big[nx^4 + y^2 + ny^4 + x^2(-1+2ny^2) \big] Ei\big[-2n(x^2+y^2) \big] \\ & - e^{n(x^2+y^2)(1+x^2+y^2)} \big[nx^4(-1+2ny^2) + y^2(4+7ny^2+2n^2y^4) \\ & + x^2(-4+6ny^2+4n^2y^4) \big] Ei\big[-n(x^2+y^2)^2 \big] \Big\}, \end{aligned} \tag{2.78}$$

$$\begin{aligned} j_y^{i(1,2)} = \frac{nNxye^{-n(x^2+y^2)(2+x^2+y^2)}}{256\pi^4(x^2+y^2)^2} \Big\{ & -8e^{n(x^2+y^2)} + 7e^{n(x^2+y^2)^2} - 2nx^2 e^{n(x^2+y^2)} \\ & + 2nx^2 e^{n(x^2+y^2)^2} - 2ny^2 e^{n(x^2+y^2)} + 2ny^2 e^{n(x^2+y^2)^2} \\ & - 4e^{n(x^2+y^2)(2+x^2+y^2)} Ei\big[-2n(x^2+y^2) \big] \\ & + e^{n(x^2+y^2)(1+x^2+y^2)} \big[2 + n(x^2+y^2) \big]^2 Ei\big[-n(x^2+y^2)^2 \big] \Big\}. \end{aligned} \tag{2.79}$$

The pressure equation can be known once the induced current density is found. However, the pressure at $\mathcal{O}(ReHa^2)$ is not solved due to its high complexity.

D. Superposition of the solutions

Finally, the flow patterns produced by the interaction of the applied and induced Lorentz forces and the localized magnetic field is obtained by the superposition of the previous solutions (Eqs. 2.57 and 2.73), that is

$$\psi = Re\psi^{(1,0)} + ReHa^2\psi^{(1,2)}, \tag{2.80}$$

Then, the total stream function is expressed by

$$\psi = Re\frac{x}{8\pi}\Bigg\{ -1 + \ln(x^2+y^2) + Ha^2\frac{e^{-n(x^2+y^2)}}{32\pi^2(x^2+y^2)}\Big\{1 + n(x^2+y^2) \\ +n(x^2+y^2)\big[n(x^2+y^2)+2\big]e^{n(x^2+y^2)}Ei\big[-n(x^2+y^2)\big]\Big\}\Bigg\}. \tag{2.81}$$

Equation (2.81) can be used for computing the flow streamlines produced by electromagnetic forces, both in liquid metals and electrolytes. For liquid metals, we consider the total stream function (Eq. 2.81), while, for electrolytes we only consider the first order term of Equation (2.80), since in a low conductivity fluid the Hartmann number is very small, and induced currents can be neglected.

2.4.4 Results

The solutions at $\mathcal{O}(ReHa^0)$ and $\mathcal{O}(ReHa^2)$, and their superposition, are presented below in order to compare and analyze the flow patterns for the different orders of approximation. The parameters used in the analytical expressions were $Re = 0.1$ and $Ha = 15$. The domain presented in the graphs is the square $-2 \leq (x, y) \leq 2$, although, in some cases, a close-up is performed in the geometric center to improve the visualization of the flow.

A. At $\mathcal{O}(ReHa^0)$

The analytical expressions for the variables presented at $\mathcal{O}(ReHa^0)$ can reproduce some features of the flow behavior generated by an electromagnetic force interacting with a negative point magnetic dipole in low conductivity fluids, for instance, in an electrolyte. The velocity field calculated with the velocity Equations (2.59) and (2.60) is shown in Figure 2.1a), in which a dipolar vortex is clearly observed, i.e., a pair of vortices rotating in opposite direction, the left-vortex rotates counterclockwise, and the right-vortex rotates clockwise. The point magnetic field is located at the geometric center, where the velocity magnitude is maximum since the Lorentz force is concentrated at this point, and is directed in the positive $y-$direction. The streamlines for the flow field can be observed in Figure 2.1b), in which it is shown that the vortices are symmetrical in both $x-$ and $y-$axes. In this flow, convective effects are negligible, and it is dominated completely by the diffusive effects for a $Re \ll 1$.

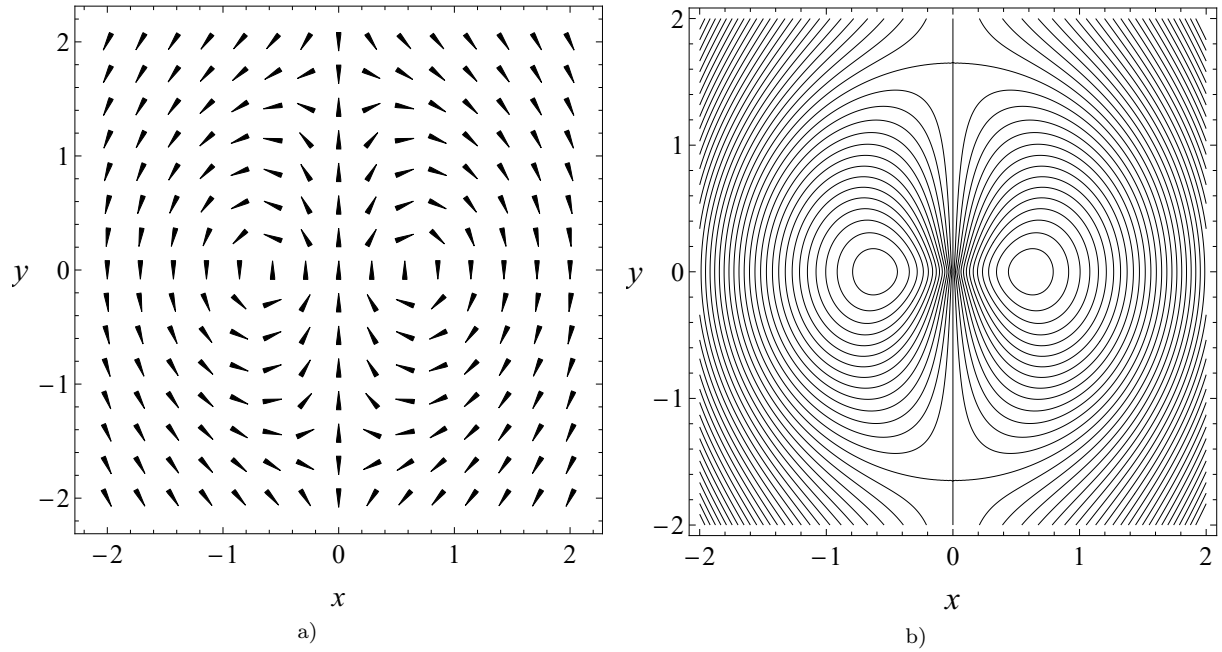

Figure 2.1: Analytical solution at $\mathcal{O}(ReHa^0)$ of the fluid motion generated by a uniform current in the $x-$direction interacting with a point magnetic dipole located at the origin. a) Velocity vector field and b) Streamlines produced by a Lorentz force in a low conductivity fluid. $Re = 0.1$.

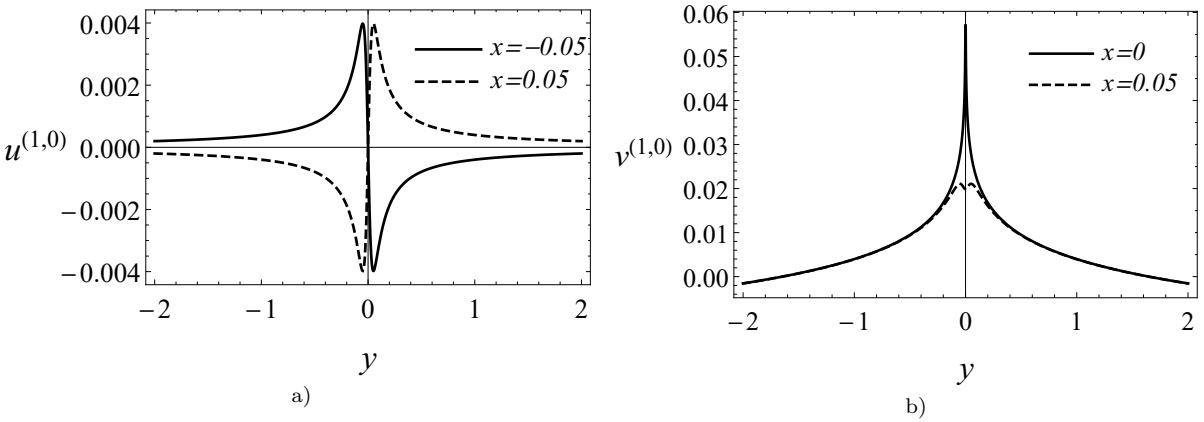

Figure 2.2: Velocity profiles at $\mathcal{O}(ReHa^0)$. a) $u-$component and b) $v-$component of the velocity as functions of y, for fixed x. $Re = 0.1$.

Figure 2.2a) shows the velocity profiles of the $u-$component as a function of the vertical $y-$coordinate, for two fixed x values. For $x = 0.05$, the change in the sign of the velocity is because the right vortex rotates clockwise and, as a consequence, the velocity profile shows negative values for negative y values. Then, it crosses the geometric center and acquires positive values for positive y values. It is worth noting that the larger absolute values for this component are located near the origin, and then vanish as $|y|$ tends to zero. The profile $x = -0.05$ shows the inverse behavior as its $x = 0.05$ counterpart,

because it describes the behavior of the $u-$component of the left vortex, which rotates counterclockwise.

The velocity profiles of $v-$component as a function of the $y-$coordinate, for two different fixed x values are shown in Figure 2.2b). For both profiles, the velocity tends to decrease as we move away from the point magnetic field, and increases its magnitude until reaching a maximum at the geometric center. In the corresponding profile for $x = 0.05$, we can observe a local maximum at $y = 0$, owing to the changes in the velocity direction when crossing to the right vortex. For higher x values, the profile behavior is similar to the profile of $x = 0.05$. Unlike the $u-$component profiles, these profiles have the same behavior for equal distances in the corresponding negative $x-$direction.

B. At $\mathcal{O}(ReHa^2)$

At $\mathcal{O}(ReHa^2)$, the analytical solution can reproduce the flow behavior produced by induced electromagnetic forces in high conductivity fluids, such as liquid metals. At this order, the velocity Equations (2.74) and (2.75) are used for obtaining the velocity field shown in Figure 2.3a), in which counter-rotating vortices are observed. The left vortex rotates clockwise, whereas the right vortex rotates counterclockwise. In the geometric center there is a singularity, as the one that exists in the applied magnetic field. The induced Lorentz force takes negative values on the $y-$direction due to the induced electric currents that travel in the opposite directions to the applied currents. The streamlines are shown in Figure 2.3b), where a symmetrical vortex, in both the $x-$axis and the $y-$axis, is observed.

The velocity profiles of the $u-$component as a function of the $y-$axis, for two fixed x values, are shown in Figure 2.4a). Along the $y-$axis, the profile $x = 0.05$ becomes larger as x approaches zero, then it crosses the geometric center, and decreases to negative values. The change in the velocity direction of the profile is owing to right-vortex rotating counterclockwise. The profile $x = -0.05$ is inverse to the profile $x = 0.05$ because it describes the behavior of left-vortex, which rotates clockwise. The profiles shown in Figures 2.2a) and 2.4a), for the $u-$components of the velocity are inverse for the same x value because the Lorentz forces that generate the motion of the vortices shown in Figures 2.1a) and 2.3a), are opposite. In Figure 2.4b) it is shown the $v-$component of the velocity as a function of y, for constant x values. Here, both profiles present a symmetry on the $y-$axis, reaching a maximum velocity for $y = 0$. Near the origin, the velocity takes negative values. The velocity tends to zero as we move away from the point magnetic field.

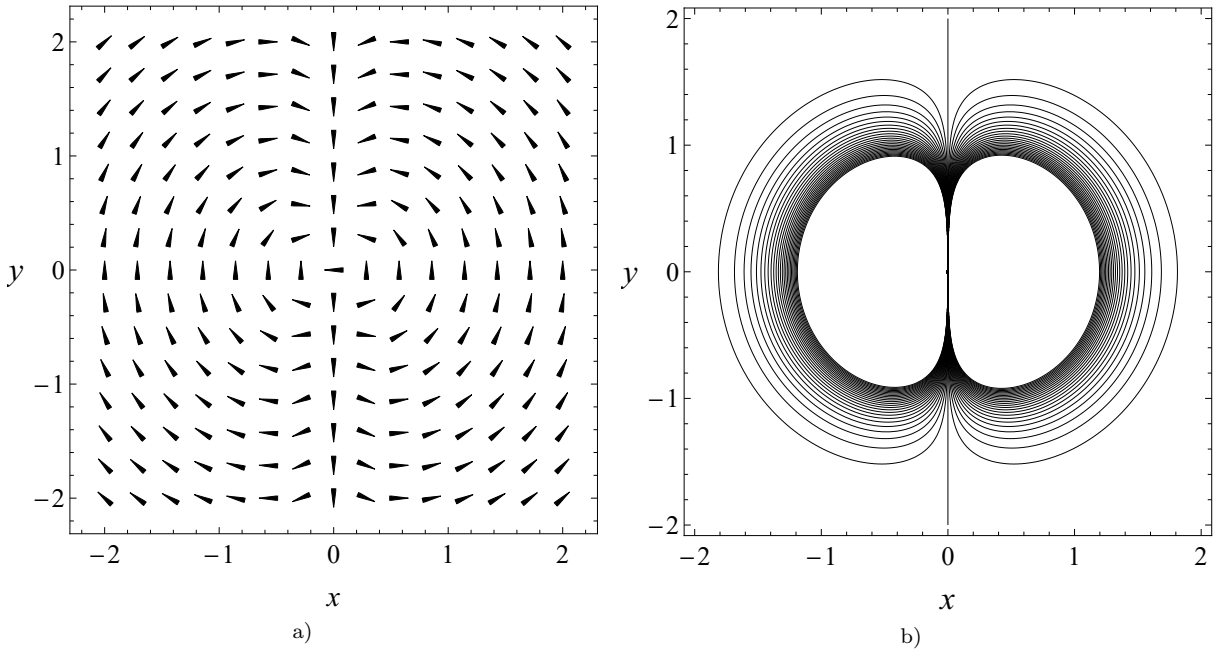

Figure 2.3: Analytical solution at $\mathcal{O}(ReHa^2)$ of the fluid motion generated by a uniform current in the $x-$direction interacting with a point magnetic dipole located at the origin. a) Velocity vector field and b) Streamlines produced by an induced Lorentz force in a high conductivity fluid. $Re = 0.1$, $Ha = 15$.

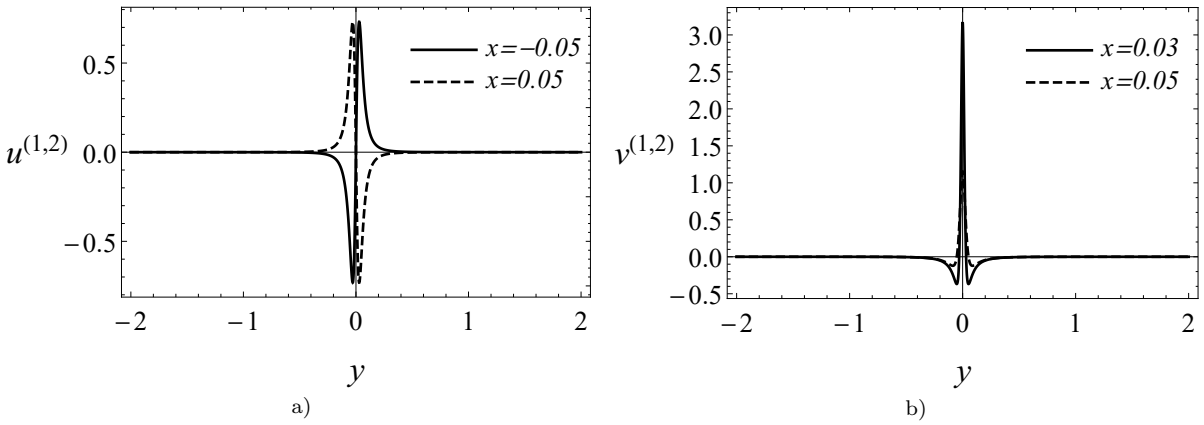

Figure 2.4: Velocity profiles at $\mathcal{O}(ReHa^2)$. a) $u-$component and b) $v-$component of the velocity as functions of y, for fixed x. $Re = 0.1$, $Ha = 15$.

C. Superposition of the solutions

The superposition of the solutions at $\mathcal{O}(ReHa^0)$ and $\mathcal{O}(ReHa^2)$ are the analytical result that describes the flow pattern generated by both, applied and induced electromagnetic forces in a high conductivity fluid, namely, a liquid metal. The velocity field is calculated through the superposition of analytical Equations (2.59) and (2.7) for the $u-$component of the velocity, and Equations (2.60) and (2.75) for the $v-$component of the velocity. Unlike

the simple dipole produced by a localized Lorentz force in a low-conductivity fluid, a more complex structure is generated in a high-conductivity fluid. In Figure 2.5a) the velocity field is shown, it can be observed the formation of four vortices, two counter-rotating external vortices directed in positive $y-$direction, and a nested counter-rotating internal dipole. The external left-vortex rotates counterclockwise, and the external right-vortex rotates clockwise. The internal vortices rotate in opposite direction to the external ones. The streamlines computed from the velocity field are shown in Figure 2.5b), in which a pair of nested dipoles are shown. Nested dipolar vortices present a symmetry in both x and y axes, since in the analytical model, the diffusive effects completely dominate the flow.

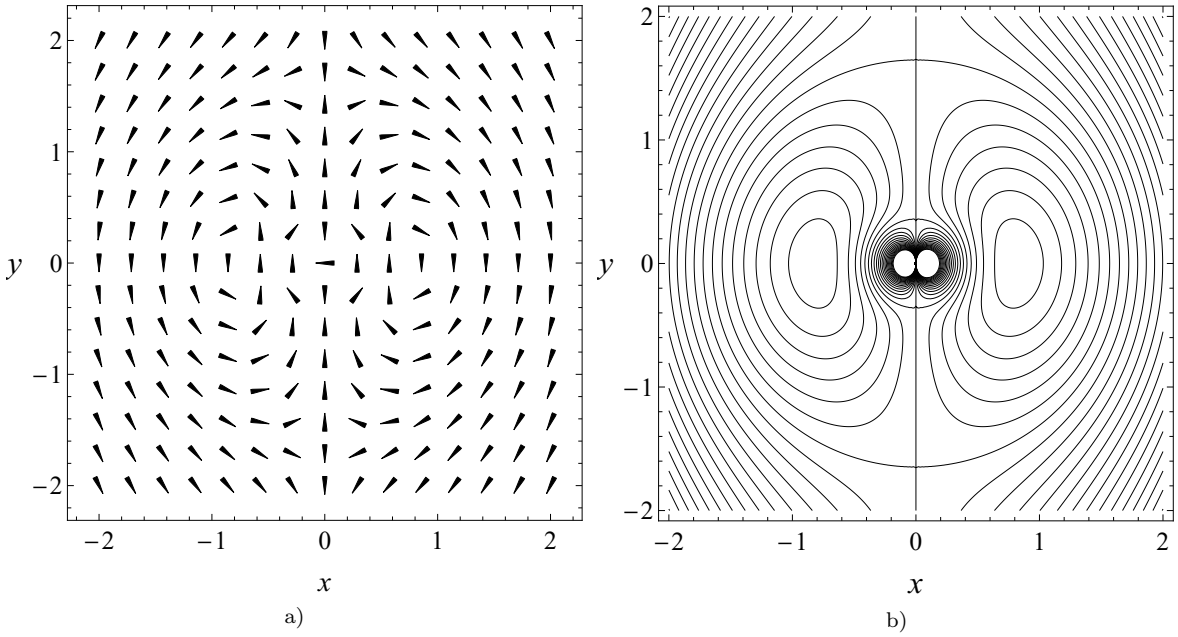

Figure 2.5: Analytical solution of the flow pattern generated in a high conductivity flow by electromagnetic forces under a point magnetic dipole. a) Velocity field and b) Streamlines. $Re = 0.1$, $Ha = 15$.

From the results at $\mathcal{O}(ReHa^0)$ and $\mathcal{O}(ReHa^2)$, we can conclude that the induced Lorentz force travels in the opposite direction to the applied Lorentz force, i.e., it opposes to the motion of the fluid. Therefore, while the external dipole is generated by the applied electromagnetic force, resulting from the interaction of the applied current with a negative point magnetic dipole; the internal dipole is produced by the induced Lorentz force generated by the interaction of the induced currents with the applied magnetic field.

In Figure 2.6, it is shown the $u-$component of the velocity as a function of x and y, respectively. Both components show equal maximum values for the same values of x and y. If we observe the profile for $y = -0.05$ or $x = -0.05$, the profiles exhibit null values away from the point magnetic field, and near the origin, the velocity takes negative maximum values in the third quadrant, then it crosses the geometric center and takes positive maximum

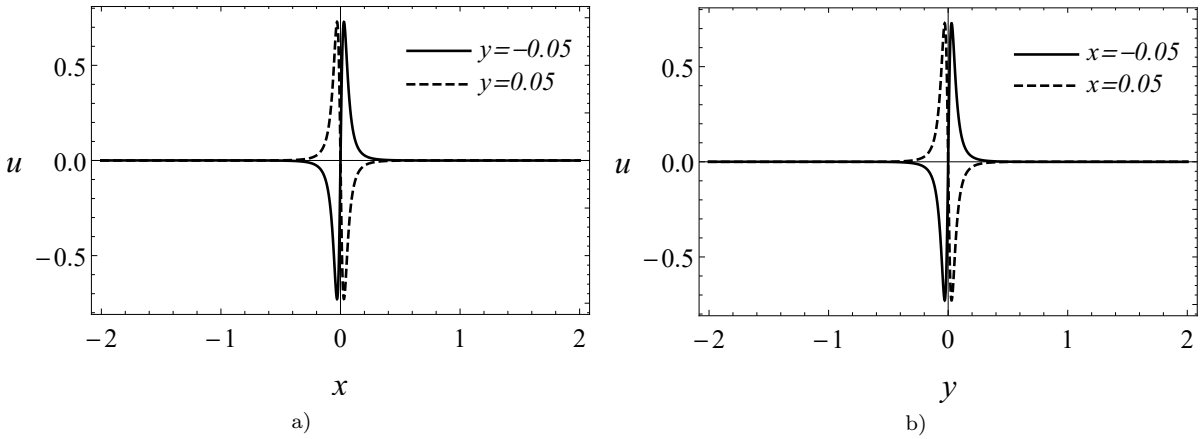

Figure 2.6: Velocity profiles of the flow pattern generated in a liquid metal. a) $u-$component of the velocity as a function of x for two fixed y values. b) $u-$component of the velocity as a function of y for constant x values. $Re = 0.1$, $Ha = 15$.

values in the first quadrant. Likewise, we can observe that, in the two Figures, the velocity profiles are inverse for the same value of either x or y, but with a negative direction.

The $v-$component of the velocity as a function of x and y is shown in Figures 2.7a) and 2.7b), respectively. Figure 2.7a) shows the profile $v(x)$ for two fixed y values, in which the velocity component is almost zero far away from the point magnetic field. Near the origin, the velocity is positive. For $x = 0$ the $v-$component of the velocity takes its maximum value. The profile $v(y)$ (Fig. 2.7b) takes negative values in the region of the magnetic field. For $y = 0$ the velocity component has its maximum positive value for both $x = 0.03$ and $x = 0.05$. For describing the velocity behavior at values of $y \leq 0.35$ and $y \geq 0.35$, we perform a close-up (Fig. 2.7c) to the center of Figure 2.7b). Positive velocities can be observed for those values of y. The velocity profile observed in Figure 2.7b) presents a similar change in direction and behavior such as the experimental profile $v(y)$ obtained with the UDV method. For $y = 0$, the qualitative behavior of the analytical and experimental profiles is different, owing to the singularity present at the geometric center in the analytical solution.

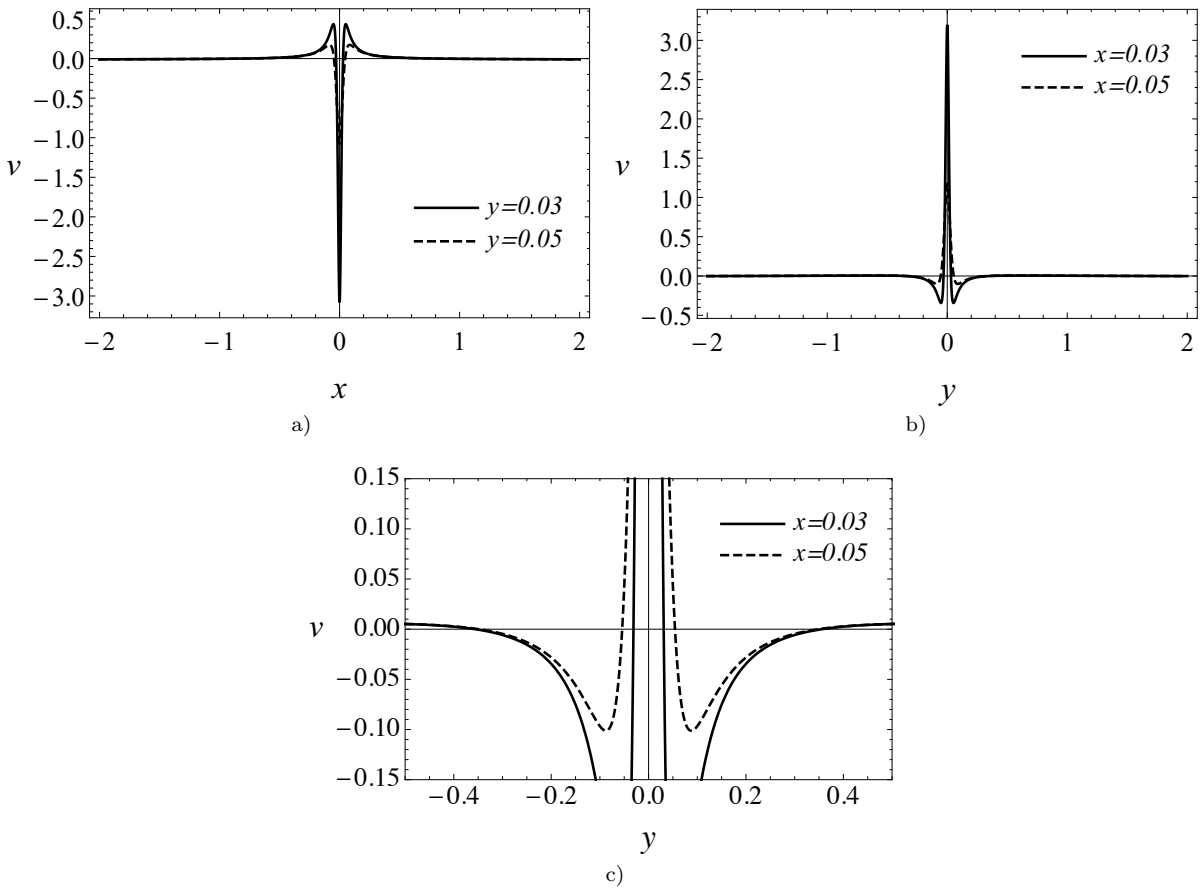

Figure 2.7: Velocity profiles of the flow pattern generated in a liquid metal. a) $v-$component of the velocity as a function of x for two fixed y values. b) $v-$component of the velocity as a function of y for constant x values. c) Close-up to the central region of b). $Re = 0.1$, $Ha = 15$.

Figure 2.8 shows isolines of vorticity of the flow obtained by means of the superposition of Equations (2.55) and (2.71), in which we can observe symmetry in both x and y axes, since as it was commented before at these orders of solution the diffusive effects dominate the flow.

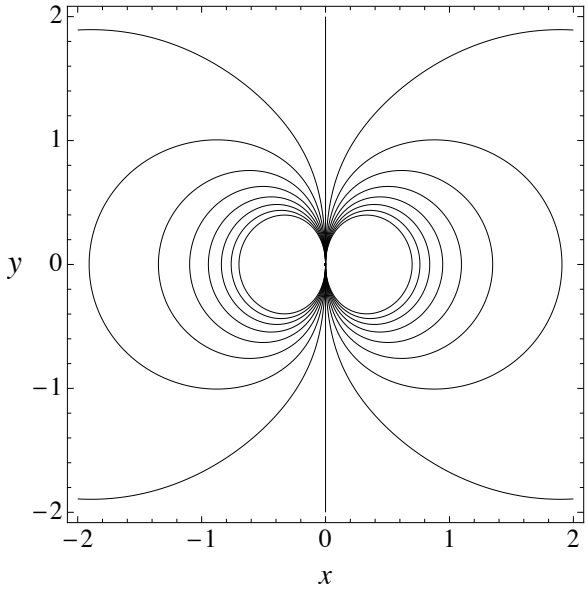

Figure 2.8: Isolines of vorticity obtained from the analytical solution. $Re = 0.1$, $Ha = 15$.

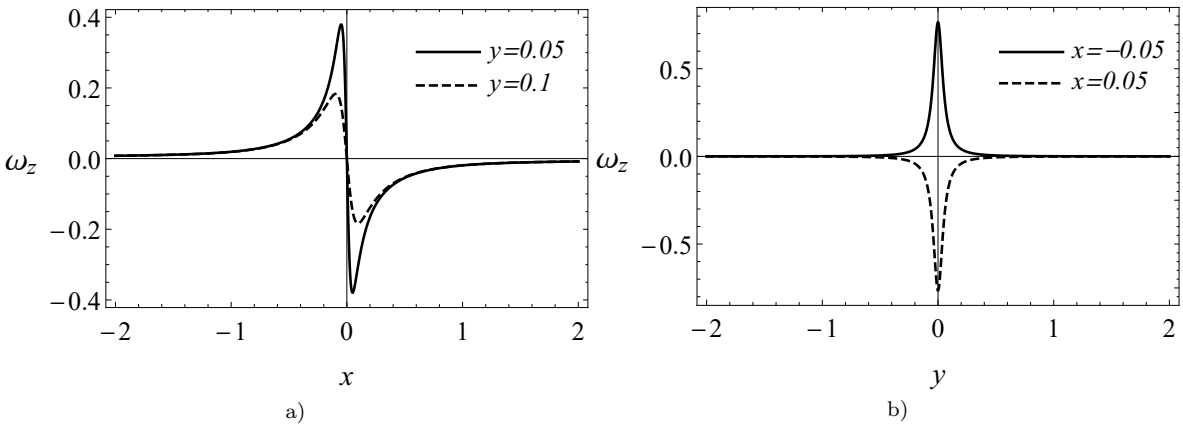

Figure 2.9: a) Vorticity as a function of x for two constant y values. b) Vorticity as a function of y for two fixed x values. $Re = 0.1$, $Ha = 15$.

In Figure 2.9a) we can observe the vorticity ω_z as a function of x for fixed y values. For $y = 0.05$, the vorticity passes from positive to negative values as the geometric center is crossed. The change of direction in the vorticity is produced by the direction of the vortex rotation. The profile for the same magnitude, but with opposite direction follows the same trajectory. Figure 2.9b) shows the vorticity as a function of y for two different x values.

In $y = 0$, the vorticity achieves the maximum magnitude. The profiles for $x = -0.05$ and $x = 0.05$ are inverse, since they refer to the left and right vortices, respectively.

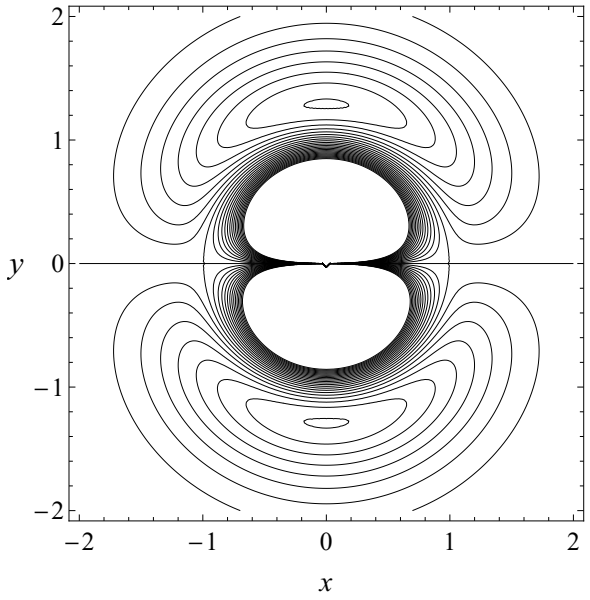

Figure 2.10: Analytical solution for isolines of the induced magnetic field on the $x - y$ plane. $Re = 0.1$, $Ha = 15$.

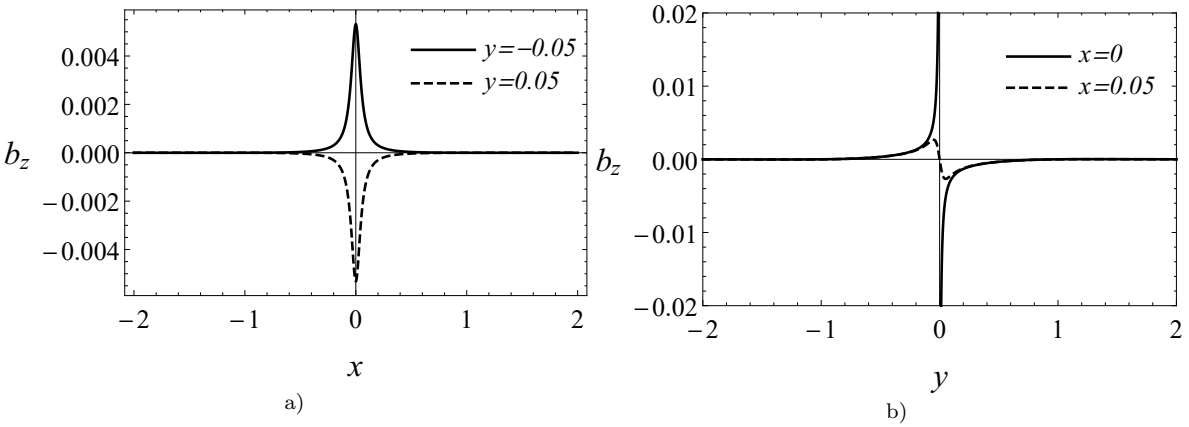

Figure 2.11: a) Variation of induced magnetic field, b_z as a function of x for y =constant, and b) b_z as function of y for x =constant. $Re = 0.1$, $Ha = 15$.

The isolines of the induced magnetic field on the $x - y$ plane are shown in Figure 2.10, where we observe the nested formation of four closed current trajectories. Figures 2.11a) and 2.11b) show the induced field, b_z, profiles as a function of x or y, respectively. In both Figures, we observe that the induced magnetic field present the maximum magnitude in the periphery of the origin. In addition, b_z is symmetric on the $x-$axis; for equal, but

opposite y values, the profile is inverse. In Figure 2.11b) the profiles are symmetrically inverse with respect to the $y-$axis.

The vector field of induced currents obtained with the superposition of Equations (2.67) and (2.68), for j_x, and Equations (2.78) and (2.79), for j_y, is shown in Figure 2.12. Here, the upper external trajectory rotates counterclockwise, while the lower external trajectory rotates clockwise. The internal trajectories rotate in opposite direction to the external ones since the direction of current rotation depends on both, the orientation of the applied magnetic field and the applied electric current. In this case, we imposed a negative and positive magnetic field in the solution at first and second order, respectively. So that the positive direction of the external dipole rotation is due to the interaction of the negative magnetic field and the fluid motion (produced by the interaction between the applied electric current and the negative magnetic field). The negative direction of the current rotation in the central dipole is due to the interaction of the positive magnetic field and the fluid motion (produced by the interaction between the applied electric current and the positive magnetic field). The induced currents produce induced Lorentz forces that oppose to the applied ones. In fact, induced Lorentz forces can generate a magnetic braking that is very noticeable in the region where the applied magnetic field is more intense.

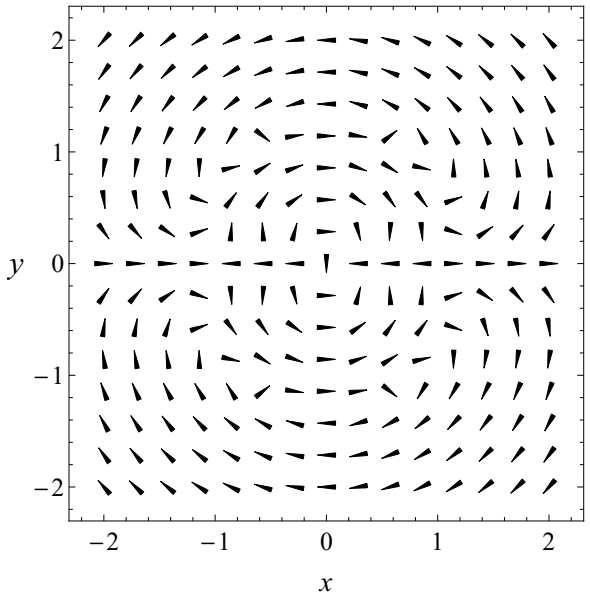

Figure 2.12: Vector field of the induced current density. $Re = 0.1$, $Ha = 15$.

Chapter 3

Quasi-two-dimensional numerical model

In Chapter 2, we presented analytic solutions describing the flows generated electromagnetically for very small Reynolds numbers. Although the analytical results showed reasonable qualitative agreement with the experiments, the model presents severe limitations when dealing with larger Reynolds numbers. On the other hand, the analytical solution also has a singularity at the origin, and the region of application is limited to a radius R. In order to overcome these limitations, in this Chapter, a quasi-two-dimensional numerical model, which avoids these types of problems, is proposed. This increases the range of Reynolds numbers that can be analyzed, so that qualitative and quantitative comparisons between theoretical and experimental results are improved. In addition to taking into account the convective term in the quasi-two-dimensional model, the friction caused by the bottom wall of the container is also considered. From the numerical results for the velocity field, the Lagrangian trajectories are calculated, which are compared qualitatively with the experimental visualizations, finding a reasonable agreement.

3.1 Quasi-two-dimensional approximation

Quasi-two-dimensional (Q2D) models for shallow fluid layers have been successfully applied to study the vortex dynamics in both hydrodynamic (Satijn et al., 2001; **?**) and magnetohydrodynamic flows (Sommeria, 1988; Figueroa et al., 2009, 2014; Lara et al., 2017; Figueroa et al., 2017). We are particularly interested in simulating the motion in a thin liquid metal layer driven by electromagnetic forces under non-uniform magnetic fields, in such a way that a Q2D model is appropriate for flows whose fluid depth is very small compared to the characteristic lateral dimensions. In these models, governing equations are integrated in the vertical direction, namely, along the applied magnetic field lines (Bühler, 1996; Smolentsev, 1997), where the friction effects due to the boundary layer at the bottom of the container are considered through a linear term in the momentum balance equations (see Eqs. 3.5 - 3.6). The present model is based on the averaging approach presented by Figueroa et al. (2009), in which many experimental characteristics, such as a uniform free surface, the Hartmann and viscous boundary layers, and both the dependence on the $z-$coordinate, and the accurate distribution of magnetic field produced by a square permanent magnet, are considered. In this model, the dimensionless dominant contribution of the magnetic field (Figueroa et al., 2009) is given by

$$\mathcal{B}_z^0(x,y,z) = \mathscr{B}_z^0(x,y)g(z). \tag{3.1}$$

As it was previously mentioned, Equation (3.1) reproduces the variation of the magnetic field $\mathscr{B}_z^0(x,y)$ in the $x-y$ plane, uniformly polarized in the normal direction (McCaig, 1977). The term $g(z) = \exp(-\gamma\varepsilon z)$, obtained experimentally, models the variation of the magnetic field in the normal direction (see more details in Subsection 1.1.1).

On the other hand, we assume that the transport of momentum is mainly driven by diffusion in the normal direction, so that the dimensionless velocity components, and the induced electric current present in the phenomenon of study, can be expressed as

$$\mathbf{u}(x,y,z,t) = [\overline{u}(x,y,t)\hat{f}, \overline{v}(x,y,t)\hat{f}, 0], \tag{3.2}$$

$$\mathbf{j}^i(x,y,z,t) = [\overline{j_x^i}(x,y,t)\hat{f}, \overline{j_y^i}(x,y,t)\hat{f}, 0], \tag{3.3}$$

where $\overline{u}$ and $\overline{v}$ are the mean velocity components in the $x-y$ plane, $\overline{j_x^i}$ and $\overline{j_y^i}$ are the mean induced currents in the same plane, while $\hat{f}$ is a function that depends on x, y and z, and reproduces the variation of the velocity profile and vorticity through the layer thickness.

Substituting Equations (3.1 – 3.3) into Equations (2.24 – 2.26), considering that the induced magnetic field is purely two-dimensional (Eq. 2.32) to satisfy the condition $\nabla \cdot \mathbf{b} = 0$, and averaging along the height of the fluid layer, the governing equations, in the Q2D approximation, are found to be (Figueroa, 2010)

$$\frac{\partial u}{\partial x} + \frac{\partial v}{\partial y} = 0, \tag{3.4}$$

$$\frac{\partial u}{\partial t} + u\frac{\partial u}{\partial x} + v\frac{\partial u}{\partial y} = -\frac{\partial P}{\partial x} + \nabla^2 u + \frac{u}{\tau} + \alpha Re^* j_y^i \mathscr{B}_z^0, \tag{3.5}$$

$$\frac{\partial v}{\partial t} + u\frac{\partial v}{\partial x} + v\frac{\partial v}{\partial y} = -\frac{\partial P}{\partial y} + \nabla^2 v + \frac{v}{\tau} - \alpha Re^* \mathscr{B}_z^0 - \alpha Re^* j_x^i \mathscr{B}_z^0, \tag{3.6}$$

$$\frac{\partial^2 b_z}{\partial x^2} + \frac{\partial^2 b_z}{\partial y^2} - \alpha\left(u\frac{\partial \mathscr{B}_z^0}{\partial x} + v\frac{\partial \mathscr{B}_z^0}{\partial y}\right) = 0, \tag{3.7}$$

where the overline on top of the velocity components was dropped for simplicity. The pressure P is normalized by ρu_0^2 (see Section 2.2). For numerical purposes, the Reynolds number in Equations (3.5) and (3.6) is defined as $Re^* = U_0 L/\nu$, where the characteristic velocity $U_0 = j^0 B_m L^2/\rho\nu$ comes from a balance between viscous and Lorentz forces, L is the characteristic side length of the magnet, j_0 is the applied current density, and B_m is the maximum magnetic field strength measured on the surface of the permanent magnet.

In Equations (3.5) and (3.6) there is a linear friction term that accounts for the effects generated both by the Hartmann boundary layer within the zone of the magnetic field, and by the viscous boundary layer where the magnetic field is negligible. The dimensionless time scale, τ, involves the decay of vorticity due to Hartmann and viscous effects, and its inverse is given by

$$\tau^{-1} = \frac{\gamma(1 - e^{-\gamma\varepsilon^2})}{\frac{1}{\gamma}(1 - e^{-\gamma\varepsilon^2}) + \frac{\gamma\varepsilon^4}{2}e^{-\gamma\varepsilon^2} - \varepsilon^2}. \tag{3.8}$$

The factor, α, in Equations (3.5 – 3.7) is calculated as

$$\alpha = \frac{1}{\gamma\varepsilon}(1 - e^{-\gamma\varepsilon^2}), \tag{3.9}$$

and represents the attenuation of the magnetic field in the normal direction. On the other hand, Equations (3.5) and (3.6) are complemented with the induction equation (Eq. 3.7) under a quasi-static approximation for the only induced magnetic field component, b_z. Equation (3.7) is normalized by RmB_m, where the magnetic Reynolds number is defined as $Rm = \mu_0\sigma U_0 L$, and μ_0 is the magnetic permeability of free space. After determining b_z, the induced currents are obtained through Ampère's law:

$$j_x^i = \frac{Ha^2}{Re^*}\frac{\partial b_z}{\partial y}, \qquad j_y^i = -\frac{Ha^2}{Re^*}\frac{\partial b_z}{\partial x}. \tag{3.10}$$

As it was previously stated, the Hartmann number is defined as $Ha = B_m L\sqrt{\frac{\sigma}{\rho\nu}}$. The system of Equations (3.4 – 3.10) was used to analyze numerically the electromagnetically driven flow at different depths in the shallow liquid metal layer. In the following Section, we present the numerical method used to solve this model.

3.2 Boundary conditions and numerical implementation

The rectangular domain used in the numerical simulations has the same dimensions as the experimental equipment into which the liquid metal is poured (see Section 1.1). The walls of the container, which are in contact with the shallow layer, are represented as four Dirichlet boundaries with non-slip conditions, namely, the velocity components vanish at the walls, that is, $u = 0$ and $v = 0$. As initial condition, the fluid is at rest. Furthermore, we assume that the induced magnetic field is equal to zero at a long enough finite distance from the permanent square magnet, therefore we assume that $b_z = 0$ at the walls. In numerical solutions, the origin $(0, 0)$ is located at the geometric center of the container, so that the coordinates at a height of 3.5 mm are within the range $-12.5 < x < -12.5$ and $-12.5 < y < 12.5$, which represents the entire area where the liquid metal layer is

confined between the electrodes (see Fig. 1.1b).

Once the boundary conditions were established, the set of Equations (3.4 – 3.10), along the magnetic field distribution given by the analytic expression by McCaig (1977), were solved numerically using the finite volume method as described by **?**, and extended to consider MHD flows. A second-order spatial discretization for a staggered grid, as the one shown in Figure 3.1, was used in the computations. Here, the velocity components u and v, the induced magnetic field, and the induced electric currents were defined at the face of the control volumes (solid black lines), while the applied magnetic field and pressure, were calculated at the center of the control volumes. With this type of grid, the nonphysical oscillations arising when calculating the pressure and velocity components at the same spatial position (checkerboard effect) are solved.

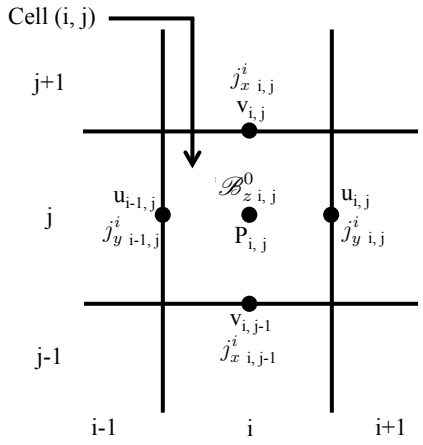

Figure 3.1: Sketch of the staggered grid used in the computations. It shows the mesh used to calculate the scalar variables. Notice that the u and v velocity components (as well as the electric currents) are displaced half a control volume in the $x-$ and $y-$directions, respectively.

The non-linear part of the equations, namely, the convective terms, are calculated on the faces of the volumes using a central average value. The discretization of the diffusive term was done by central differences. The Euler method was used for time discretization. Overall, spatial terms were second-order accurate, whereas the temporal scheme provides first order approximation. This type of discretization is the simplest, and requires less computational effort to obtain converged solutions than higher-order approximations. The numerical solution satisfies the boundary conditions and the initial condition in $t = 0$, $u = v = 0$ and $P = 0$.

In order to decouple the pressure and velocity fields in the system of Equations (3.4 – 3.6), a SIMPLEC method, as it is described by **?**, is carried out. Since the numerical results are to be compared (both qualitatively and quantitatively) with experimental observations

and measurements, vector fields, streamlines and velocity profiles will be presented and discussed.

3.3 Numerical results

The experimental and analytical results presented in previous Chapters allow to understand the general behavior of the flow, that is, the formation of two pairs of nested vortices, showing a region of quasi-stagnation in the central part. One of the main ingredients of the studied phenomena is that the fluid motion is generated by electromagnetic forces produced by the interaction of the applied magnetic field with the injected electric current. In addition, it is known that induced electric currents interacting with the applied magnetic field produce Lorentz forces that oppose the fluid motion. In a general way, with these ingredients it is possible to have a reasonable physical understanding of the flow pattern. Nevertheless, in order to have a deeper understanding of the flow and to be able to consider more realistic conditions close to the experiments carried out, numerical simulation results are required.

The numerical simulations were performed by varying the applied electric current in the range from 250 mA to 1 A, for two applied maximum magnetic field values of $B^0_{z,m} = 0.218$ T and $B^0_{z,m} = 0.181$ T. By combining both parameters, simulations were obtained at two different heights of the liquid metal layer. These numerical results can be compared with the experiments obtained using the two measurement techniques. As already mentioned in Chapter 1, the UDV technique allowed to one velocity component of the flow in the bulk of the fluid layer, at a height of 3.5 mm. In turn, the PIV technique allowed to obtain the velocity field on the surface of the liquid metal layer, at a height of 5.5 mm. The numerical solutions will be presented with the set of dimensionless parameters Re and Ha, where the Reynolds number is calculated as $Re = U_{max}L/\nu$; here, U_{max} is the resulting maximum velocity of the numerical solution. In addition, the applied electric current, I, will also be reported in the numerical results. The selected mesh for all simulations was $nx = 201$ and $ny = 201$, whereas the time-step chosen was $\Delta t = 6.5\text{x}10^{-7}$. In this way, all residual quantities were kept very small.

Figure 3.2 shows two visualizations of the numerical solution of the flow motion for an applied electric current of 350 mA and a magnetic field strength of $B^0_{z,m} = 0.218$. Figures 3.2a) and 3.2b) show the vector velocity field and streamlines, respectively. In both results, the formation of a pair of symmetric dipole vortices with respect to the $y-$axis, with a quasi-stagnation zone in the center of the inner dipolar vortex, are observed. In the velocity field, we can observe that the rotation of the right external vortex is clockwise, while the left external vortex rotates counterclockwise. The pair of internal vortices rotate in the opposite direction to the external ones. In this picture, we can also observe that the maximum magnitude of the velocity is located in the outer part of the internal vortices, while the lowest velocities are located in the quasi-stagnation region. On the walls, the

velocity vanishes due to the imposed non-slip condition. Both the formation of the four recirculations and their core can be clearly seen in the streamlines shown in Figure 3.2b).

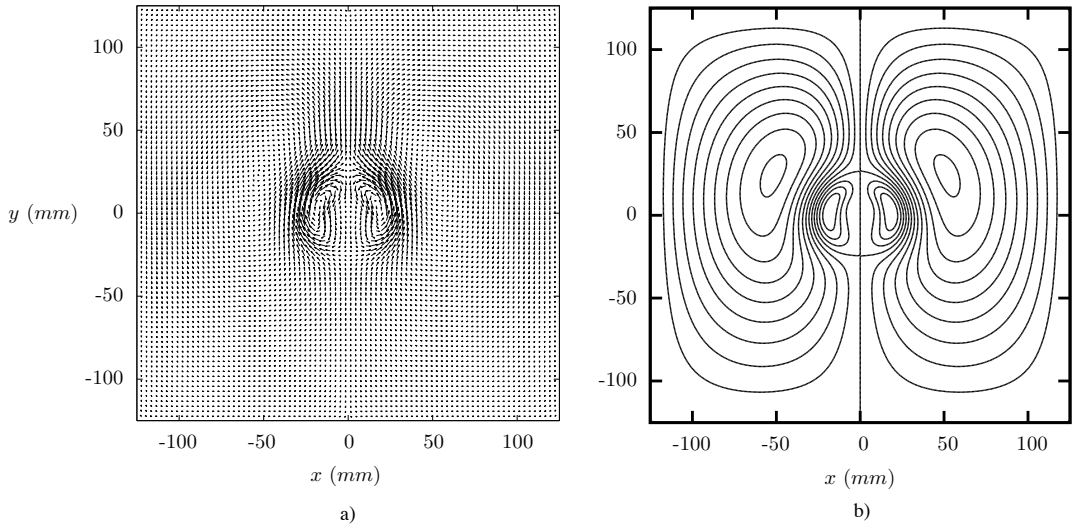

Figure 3.2: a) Velocity vector field and b) streamlines of fluid motion driven by electromagnetic forces obtained numerically. $I = 350$ mA, $z = 3.5$ mm, $B^0_{z,m} = 0.218$, $Re = 112$, $Ha = 221$ and $N = 436$.

The central velocity profiles obtained from the velocity vector field (Fig. 3.2a) are shown in Figure 3.3. The $v-$component velocity profile as a function of x position, for $y = 0$, is presented in Figure 3.3a), in which we can observe a perfectly symmetrical profile that satisfies no-slip condition at the walls. The curve reaches a local negative minimum near $x \approx \pm 120$ mm, increases and crosses by zero at $x \approx \pm 55$ mm until reaching global maximum velocities at $x \approx \pm 30$ mm, then it decreases and vanishes at $x \approx \pm 20$, continues to decrease reaching a global minimum value at $x \approx \pm 13$ and it increases again reaching a local maximum value at $x = 0$. The changes of direction of the $v-$component velocity profile are due to the direction of rotation of the four vortices. Further, the curve shows that the highest velocity magnitudes are found in the boundary between the internal vortices and the external ones.

Figure 3.3b) shows the $v-$component velocity profile as a function of the y position for $x = 0$. Here, the velocity at the walls vanishes owing to the boundary condition mentioned in Section 3.2. From bottom to top, the curve has positive values in a range from $y = -125$ mm to $y \approx -28$ mm, reaching a local maximum at $y \approx -45$ mm, then it decreases until a minimum local value at $y \approx -14$ mm. In the central part of the container, the magnitude of the velocity is reduced until a local maximum is reached at $y \approx 5$ mm. The velocity decreases, reaching a global minimum value at $y \approx 15$ mm, increases its value and crosses zero at $y \approx 23$ mm, then it reaches a global maximum value at $y \approx 50$.

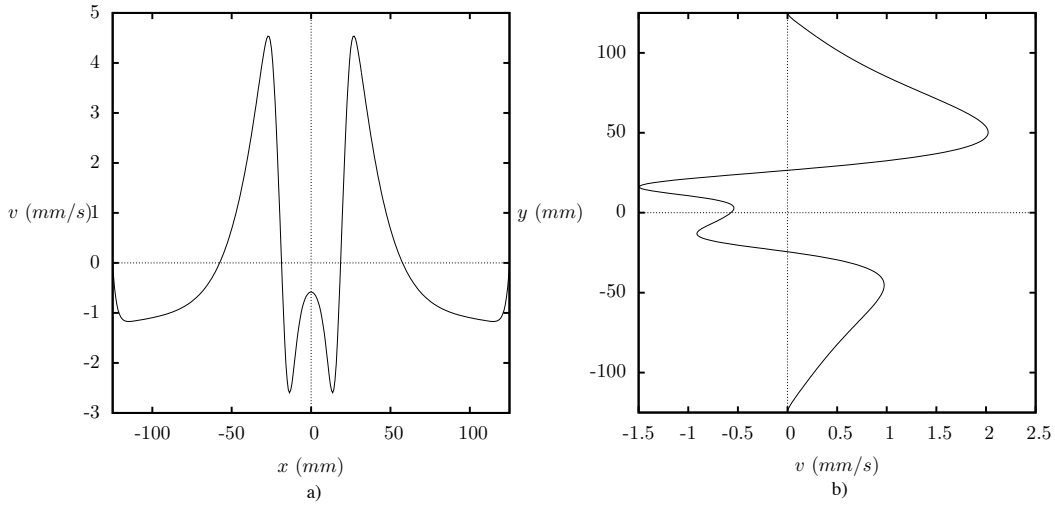

Figure 3.3: $v-$component velocity profiles a) along x for $y = 0$ and b) along y for $x = 0$, $z = 3.5$ mm; $I = 350\ mA$, $Re = 112$, $Ha = 221$ and $N = 436$.

Unlike the velocity of the v component along the $x-$axis, this velocity profile does not show symmetry along the y coordinate since both, the applied electromagnetic force and the induced Lorentz force of higher magnitude are included in the equation for this velocity component, causing a preferential flow direction and, thus, the observed asymmetry along the $y-$axis.

Both, Figure 3.3a) and 3.3b) show a velocity reduction in the central part of the container, where the magnetic field is stronger. This decrease in velocity is also observed experimentally, as shown in the experimental section of the present document, and it is caused by the interaction between the fluid in motion (produced by the applied electromagnetic forces) and the induced electric currents that interact with the applied magnetic field, and produce induced Lorentz forces that are oppose the applied electromagnetic force.

In order to understand the phenomenon under study in more detail, two particular quasi-two-dimensional numerical simulations of the flow, separating the distribution of the magnetic field produced by a square-shaped permanent magnet (see Subsection 1.1.1) were carried out[1]. Namely, in the first simulation, only the positive orientation of the field was applied, while, for the second one, a negative magnetic field distribution was taken into account. The results are presented in Figure 3.4, on the left-hand side, the numerical results in which a positive magnetic field and an applied electrical current of 350 mA interact, are shown. On the right-hand side, the results obtained for the same applied current, but with a purely negative field distribution, are shown.

[1]These simulations were suggested by Dr. Aldo Figueroa.

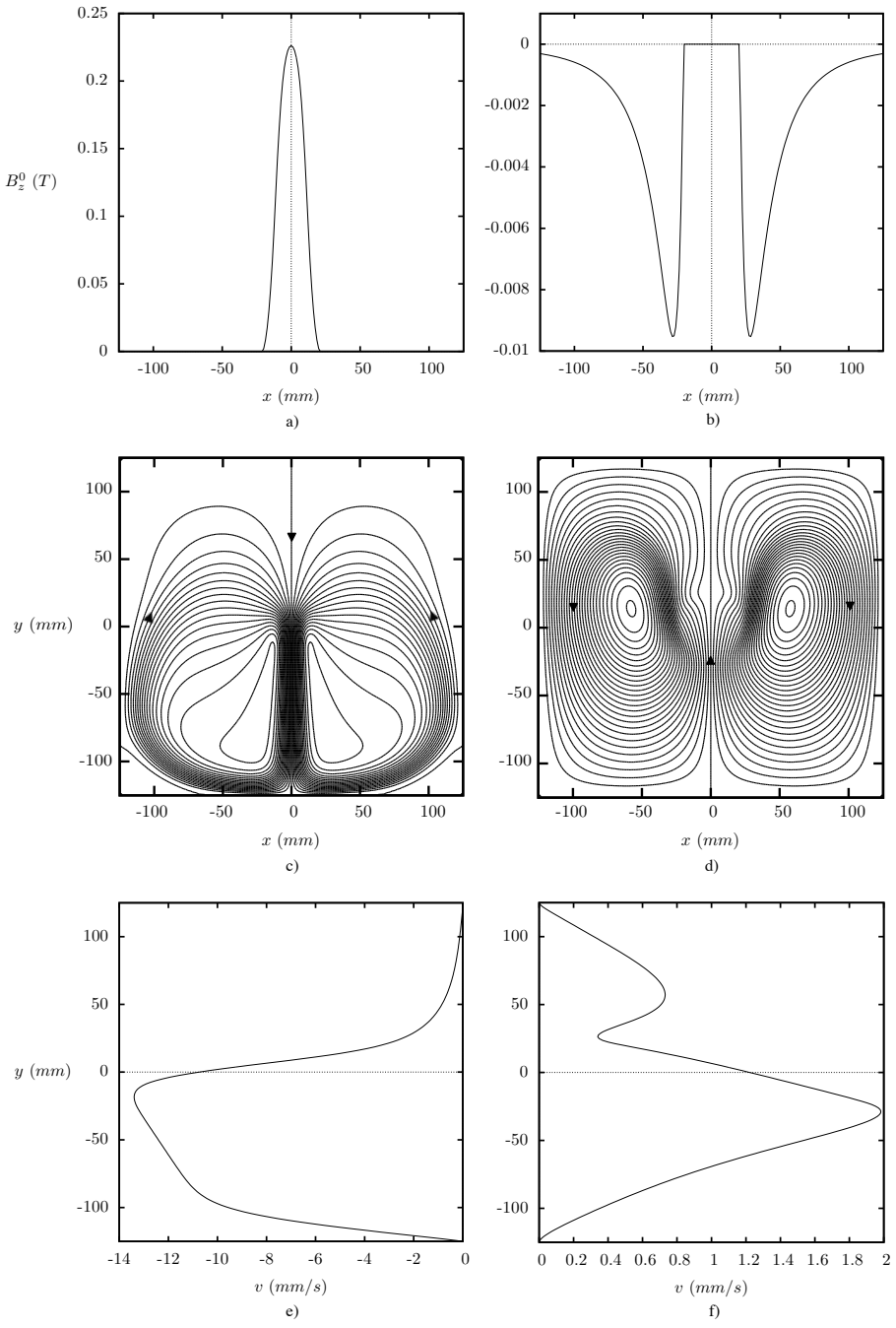

Figure 3.4: Numerical results of the flow pattern produced by electromagnetic forces generated by a separated magnetic field distribution. (Top row) a) Positive and b) negative part of the magnetic field distribution. (Middle row) Flow patterns generated by Lorentz forces produced by the c) positive and d) negative magnetic field. (Bottom row) $v-$component velocity profiles along y for $x = 0$ extracted from the flow patterns produced by the e) positive and f) negative magnetic field distributions. $I = 350$ mA, $Ha = 221$.

Figure 3.4a) shows the cross-section of the positive magnetic field distribution in dimensional parameters. Notice that the maximum intensity of the magnetic field ($B_z^0 = 0.218$ T) is located in the center of the container, at $x = 0$, and moving away from this point the field decays quickly, both for positive and negative x values, until becoming zero approximately at $x = \pm 19$ mm. In Figure 3.4b), the negative magnetic field distribution in the cross-section is shown; here, we can observe that the profile has two minimum values ($B_z^0 = -0.0095$ T) approximately at $x = \pm 27$ mm, as $|x|$ increases, the curve decreases quickly and takes very small values at the walls of the container. Since only negative values for the magnetic field are considered in this case, a zero value was assigned in the central region of the plot. In this way, the profile presented in Figure 3.4b) is the complement of the magnetic field curve presented in Figure 3.4a). Both Figures 3.4a) and 3.4b), added together, are the reproduction of the magnetic field distribution produced by a permanent square magnet. Figure 3.4c) shows the numerically obtained streamlines for the behavior of a flow generated in a layer of liquid metal due to the interaction of a direct electric current (applied from left to right) with the distribution of a positive magnetic field (Figure 3.4a). In this simulation, the formation of a dipolar vortex, with higher velocities in the central part of the container (around $x = 0$), is observed. The interaction of the electric current and magnetic field produces a Lorentz force in the negative y direction which, in turn, elongates the vortices in this direction (arrows indicate the direction of fluid motion). It is well known that, if a fluid of high electrical conductivity moves in the presence of a magnetic field, induced electromagnetic forces (opposite to the applied electromagnetic forces) are produced. In the case of the motion in the liquid metal layer, the induced Lorentz forces are present in the system, and oppose the fluid motion, thus reducing the velocities and, due to the mass conservation, the fluid recirculates to the region where the fluid motion is driven, that is, where the magnetic field is stronger and the applied electromagnetic forces are produced. The motion of the liquid metal layer under a negative magnetic field distribution (see Fig. 3.4b), generates two vortices with a reduction of the velocity around $x = 0$ and the values about $y \approx 5$ mm and $y \approx 40$ mm as it is observed in Figure 3.4d) where the vortices travel in positive y-direction in the central part and in negative y-direction near to the walls as the arrows on the picture indicate. Figures 3.4e) and 3.4f) show the $v-$component velocity profile as a function of y for $x = 0$. The maximum velocity is located at $y \approx -13$ mm where the motion is generated with the positive magnetic field, whereas the maximum velocity value is observed at $y \approx -28$ mm for the flow produced with the negative magnetic field. Notice that the positive magnetic field produces velocities two orders of magnitude higher than its negative counterpart.

The direction of the applied and induced Lorentz forces are shown in Figure 3.5. In the top part, the magnetic field distribution B_z^0 along x can be observed. Here, the circles shows the negative and positive distributions existing in a magnet with north orientation in the central zone.

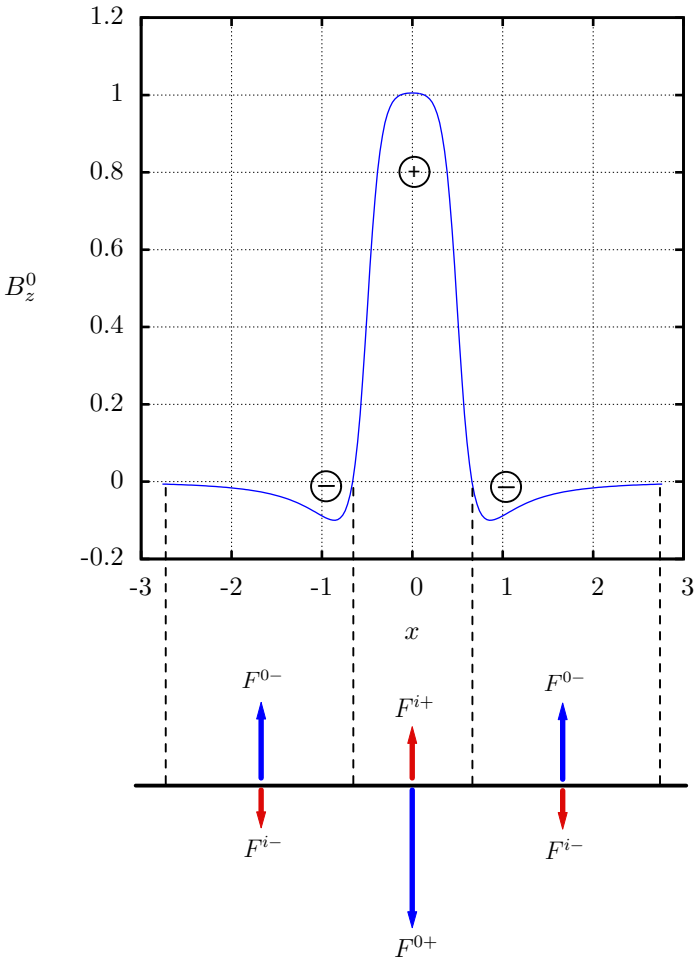

Figure 3.5: Diagram of the direction of applied and induced Lorentz force produced in the different magnetic field distributions. Blue arrows represent the applied Lorentz forces, while Red arrows are the induced electromagnetic forces.

3.4 Two-dimensional idealized numerical model

Quasi-two-dimensional approximations are a set of equations that, under certain considerations, allow us to understand characteristics of the flow behavior produced under strong magnetic fields (**?**), or in shallow fluid layers (Figueroa et al., 2014), while two-dimensional approximations can be used to study the vortex dynamics in some cases in the oceans and in the atmosphere, because the existing motions in these phenomena are predominantly horizontal (Cruz-Gómez et al., 2013). The two-dimensional approximation can also be used to analyze some experiments performed in laboratory neglecting the effect of the bottom friction. For the present numerical study, we employ a purely two-dimensional approximation that solves the mass conservation equation, and the momentum conser-

vation equation plus an external Lorentz force, to understand the fluid flow driven by electromagnetic forces under a non-uniform magnetic field in a liquid metal layer. Equations (2.34 – 2.36), obtained and presented in Chapter 2, are rewritten below for the simplified two-dimensional case

$$\frac{\partial u}{\partial x} + \frac{\partial v}{\partial y} = 0, \tag{3.11}$$

$$\frac{\partial u}{\partial t} + u\frac{\partial u}{\partial x} + v\frac{\partial u}{\partial y} = -\frac{\partial P}{\partial x} + \frac{\partial^2 u}{\partial x^2} + \frac{\partial^2 u}{\partial y^2} + Rej_y^i \mathscr{B}_z^0(x,y), \tag{3.12}$$

$$\frac{\partial v}{\partial t} + u\frac{\partial v}{\partial x} + v\frac{\partial v}{\partial y} = -\frac{\partial P}{\partial y} + \frac{\partial^2 v}{\partial x^2} + \frac{\partial^2 v}{\partial y^2} - ReB_z^0 - Rej_x^i \mathscr{B}_z^0(x,y). \tag{3.13}$$

Similarly to the quasi-two-dimensional model, the dominant magnetic field component ($\mathscr{B}_z^0(x,y)$) along the normal $z-$direction is the only one considered. The expressions that describe the non-homogeneous distribution of a single permanent magnet were shown in Equations (1.3 – 1.4) in Chapter 1. To complete the system of equations we must solve the induction equation

$$\frac{\partial^2 b_z}{\partial x^2} + \frac{\partial^2 b_z}{\partial y^2} - u\frac{\partial \mathscr{B}_z^0}{\partial x} - v\frac{\partial \mathscr{B}_z^0}{\partial y} = 0, \tag{3.14}$$

and, in turn, from Ampère's law (Eq. 2.27b), the components of the induced currents present in Equations (3.12 – 3.13) are

$$j_x^i = N\frac{\partial b_z}{\partial y}, \qquad j_y^i = -N\frac{\partial b_z}{\partial x}, \tag{3.15}$$

where the Stuart number is expressed as $N = Ha^2/Re$, as in Chapter 2. The system of Equations (3.11 – 3.14) is solved numerically under the same conditions as the quasi-two-dimensional numerical model exposed in the Section 3.1 in a square domain corresponding to the dimensions of the experimental device. The 2D magnetic field distribution is modeled from the analytic expression by McCaig (1977). The governing equations were solved using a Finite Volume Method and a SIMPLEC algorithm (**?**), with no-slip boundary conditions at the walls of the square frame, and a fluid at rest as initial condition.

3.5 Two-dimensional numerical results

As it was previously mentioned, the purely two-dimensional numerical model is used in order to analyze the flow pattern produced by strong electromagnetic forces in a shallow liquid metal layer in an idealized way, that is, neglecting the bottom friction effects. Due to the dimensionality used to obtain the equations of the model, we can intensify or decrease the Lorentz forces by adjusting the Reynolds (Re) and Hartmann (Ha) numbers present in Equations (3.12 – 3.13). The two-dimensional numerical simulations were carried out

using $Re = 50$ and $Ha = 250$. For these values, the flow behavior is shown in Figure 3.6, where we can observe the velocity vector field (Figs. 3.6a and 3.6b) and streamlines (Figs. 3.6c and 3.6d) for the full domain (left column) and central region (right column) of the container.

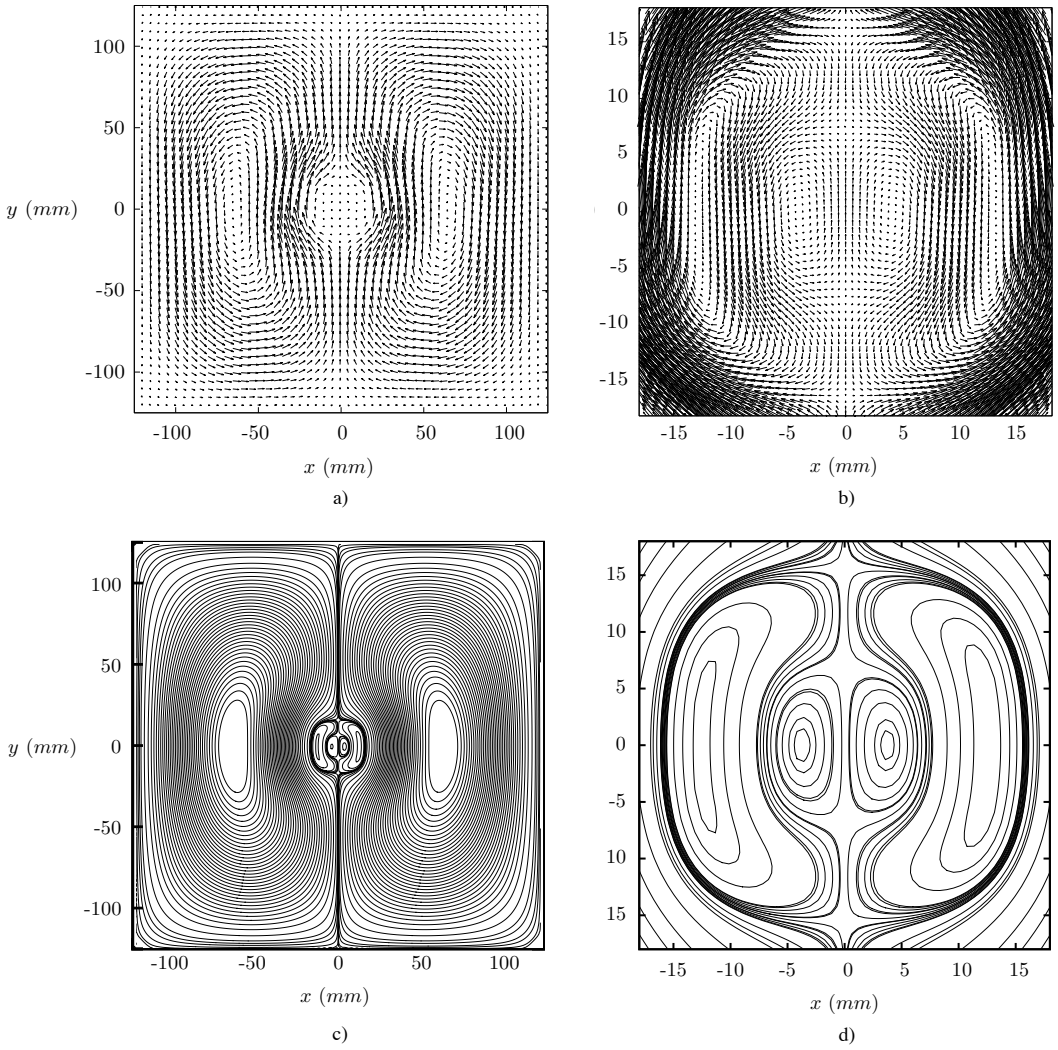

Figure 3.6: Velocity vector field (top row) and streamlines (bottom row) of the six vortex pattern predicted by the two-dimensional numerical model with $Re = 50$ and $Ha = 250$. The left column shows the full domain of the container, while the right column is the amplification of the flow region of the nested internal dipolar vortex.

Figure 3.6c) shows the formation of three nested dipolar vortices. This pattern is the result of the changes of the velocity direction shown in the Figure 3.6a), where the rotation of the external vortices points in $y-$direction, that is, the external right-vortex rotates clockwise, while its left counterpart rotates counter-clockwise. The rotation of the pair

of internal vortices is opposite to the rotation of the external vortices. The rotation of the pair of the innermost internal central vortices is on the same direction as the external vortices. The flow pattern of the nested internal and central vortices is clearly shown in Figure 3.6d).

In Figure 3.7 the central velocity profile for both coordinate axes is shown. Figure 3.7a) shows the $v-$component velocity profiles along $x-$axis for $y = 0$, in which, we can observe zero velocities at $x = \pm 125$ mm, because the non-slip condition imposed at the walls of the container. From left to right, first the velocity profile takes negative values reaching a minimum value at $x \approx -98$ mm, then increases, vanishes at $x \approx -64$ mm and reaches a positive maximum velocity at $x \approx -34$ mm. For the following values of x the curve decreases, crosses zero at $x \approx -13$ mm and continues decreasing until reaching a local minimum value at $x \approx -10$ mm, after this point, the velocity increases again, crosses zero at $x \approx -4$ mm and, at $x = 0$, the curve reaches a local maximum value. It can be observed that the $v-$component velocity profile is symmetric along of the $x-$axis. The $v-$component velocity profiles along $y-$axis for $x = 0$ are shown in Figure 3.7b), where the velocity at the walls is also zero due to the previously mentioned no-slip condition. From bottom to top, the profile takes positive values until reaching a maximum value at $x \approx -54$ mm, then decreases, crosses zero at $x \approx -16$ mm, continues decreasing and reaches $x \approx -12.5$ mm, where it presents a local minimum, from this point forward, the curve increases again, crosses zero at $x \approx 7$ mm and reaches another maximum local value at $x = 0$. This figure also shows that the $v-$component of the velocity is symmetric along the $y-$axis. Both, Figure 3.7a) and Figure 3.7b), show the change of the velocity direction according to the rotation of the six-vortex pattern shown in Figure 3.6.

The three nested dipolar vortices pattern in the two-dimensional numerical model is driven, initially, by applied electromagnetic forces generated through the interaction of the applied electric current and the magnetic field produced by a square-shaped permanent magnet with positive and negative distribution. The fluid in motion, generated by the applied Lorentz forces, interacts with the applied magnetic field producing induced electric currents. In turn, the induced currents interact with the applied magnetic field, producing induced electromagnetic forces opposite to the applied Lorentz forces. Under these physical foundations, and using Figure 3.5, it is possible to understand in detail the formation and direction of the rotation of the vortices shown in Figure 3.6c), where we can observe that the rotation of the external vortices is the results of the interaction between the applied electric current and the negative distribution of the magnetic field (generated at the edges of the magnet). This interaction produces applied electromagnetic forces, (F^{0-}), along the $y-$direction. In turn, the induced electric currents (generated by the fluid in motion and the applied magnetic field) interact with the applied magnetic field, producing induced Lorentz forces, (F^{i-}), opposite to the applied electromagnetic forces, i.e., in the negative y-direction. Since in the edges the induced forces have a small magnitude, they do not modify the fluid motion. In the area where the magnetic field distribution is positive, a pair of dipolar vortices is observed for values of $Re = 50$

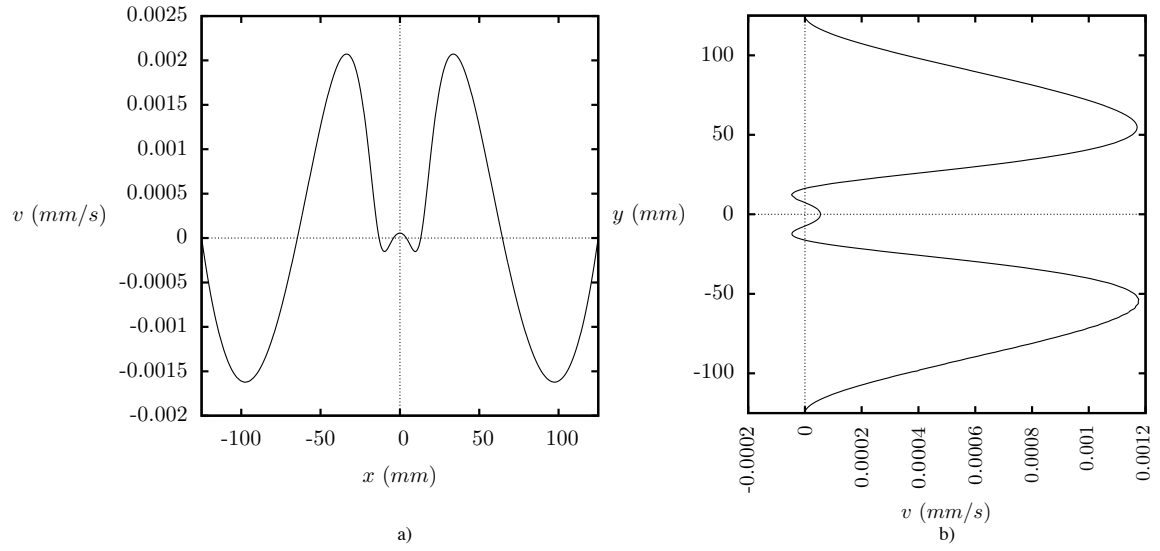

Figure 3.7: $v-$component velocity profile a) for $y = 0$ as a function of x and b) for $x = 0$ as a function of y obtained by a two-dimensional numerical simulation. $Re = 50$, $Ha = 250$.

and $Ha = 250$. Here, the intermediate vortex is driven by the applied electromagnetic force, (F^{0+}), produced by the interaction of the electric current and the positive magnetic field, while the central internal vortex is generated by the induced electromagnetic force, (F^{i+}), produced by the interaction of the induced electric current, and the applied magnetic field. Unlike the quasi-stagnation zone located in the central part of the flow pattern obtained from the quasi-two-dimensional model, in the two-dimensional simulations the viscous or Hartmann frictions that oppose to the fluid motion are negligible. Thus, when we apply a large Hartmann number, the induced electromagnetic forces are larger than the applied forces, producing a change in direction of the velocity, resulting in the generation of a central internal dipolar vortex where the magnetic field is more intense.

In previous works, flow patterns similar to those reported in this model have been found. For instance, in the two-dimensional numerical simulations of the flow of an electrically conductive fluid by means of electromagnetic forces produced by the interaction of induced electric currents with a non-uniform magnetic field (Cuevas et al., 2006), we can observe the formation of a pattern of dipolar vortices for values in the range $7 < Ha < 50$, and a pair of nested dipole vortices for values in the interval $50 \leq Ha \leq 100$. The continuation of the study of the creeping flow past a magnetic obstacle is presented in **?**, where the value of the Hartmann number is increased up to $Ha = 125$, giving as a result of the simulation, a pattern of three nested dipolar vortices very similar to those presented in Figure 3.6c). Although, in this project the initial motion of the fluid is not generated in the same way as in the work presented by **?**, the change of velocity direction in the central part of the flow pattern generates a pair of internal central vortices to fulfill the

mass conservation equation ($\nabla \cdot \mathbf{u} = 0$).

The $v-$component velocity profiles for different values of x and y are shown in Figure 3.8. The profiles for $y = \pm$ 50 mm can be observed in Figure 3.8a), which shows that, for both values of y, the curves are approximately equal. Both have maximum negative values in $x \approx \pm 99$ mm and maximum positive values in $x \approx \pm$ 14 mm; in $x = 0$ the profile decreases reaching a local minimum. The same velocity profile for $y = \pm 100$ mm is shown in Figure 3.8b), the curve shows two negative minimum values at $x \approx \pm$ 93 mm, and a positive maximum value at $x = 0$. The profile for $y = 100$ mm has the same slopes as the profile for $y = -100$ mm, but larger absolute values in the vicinity of the global extrema, in both the positive and negative part; this curve only shows one change of the velocity direction, therefore we are observing only the external recirculations of the flow pattern. Figure 3.8c) shows the $v-$component velocity profile as a function of y for $x = \pm 50$ mm. Here, both curves have the same slopes and show a positive maximum value at $y = 0$; the profile for $x = 50$ mm has slightly greater values than the curve for $x = -50$ mm. The same velocity profile for $x = \pm 100$ mm is shown in Figure 3.8d), in which both curves take a positive maximum value at $y = 0$. Unlike the profiles shown in Figure 3.8c), these curves have larger magnitudes of the velocity near the walls of the container. The shape of both profiles for $x = \pm 100$ mm is similar to that of a Poiseuille flow. The trajectory of the curves obtained for the values $x = \pm 50$ mm and $y = \pm 50$ mm are located near the zone where the magnetohydrodynamic flow occurs, while the profiles in Figures 3.8a) and 3.8b) show a hydrodynamic behavior. All the $v-$component velocity profiles are symmetrical along the $x-$ and $y-$axes passing through the origin, as can be seen in Figures 3.8a) and 3.8 b), and 3.8c) and 3.8d), respectively. Notice that the difference between the curves shown in the Figures 3.8b) and 3.8c) is on the closest value to the origin of x and y.

Figure 3.9 shows isolines of vorticity for the whole domain, in which we observe three nested dipolar vortices; the red color represents positive values of the vorticity, while the blue color implies negative values. This observation is in qualitative agreement with experimental results.

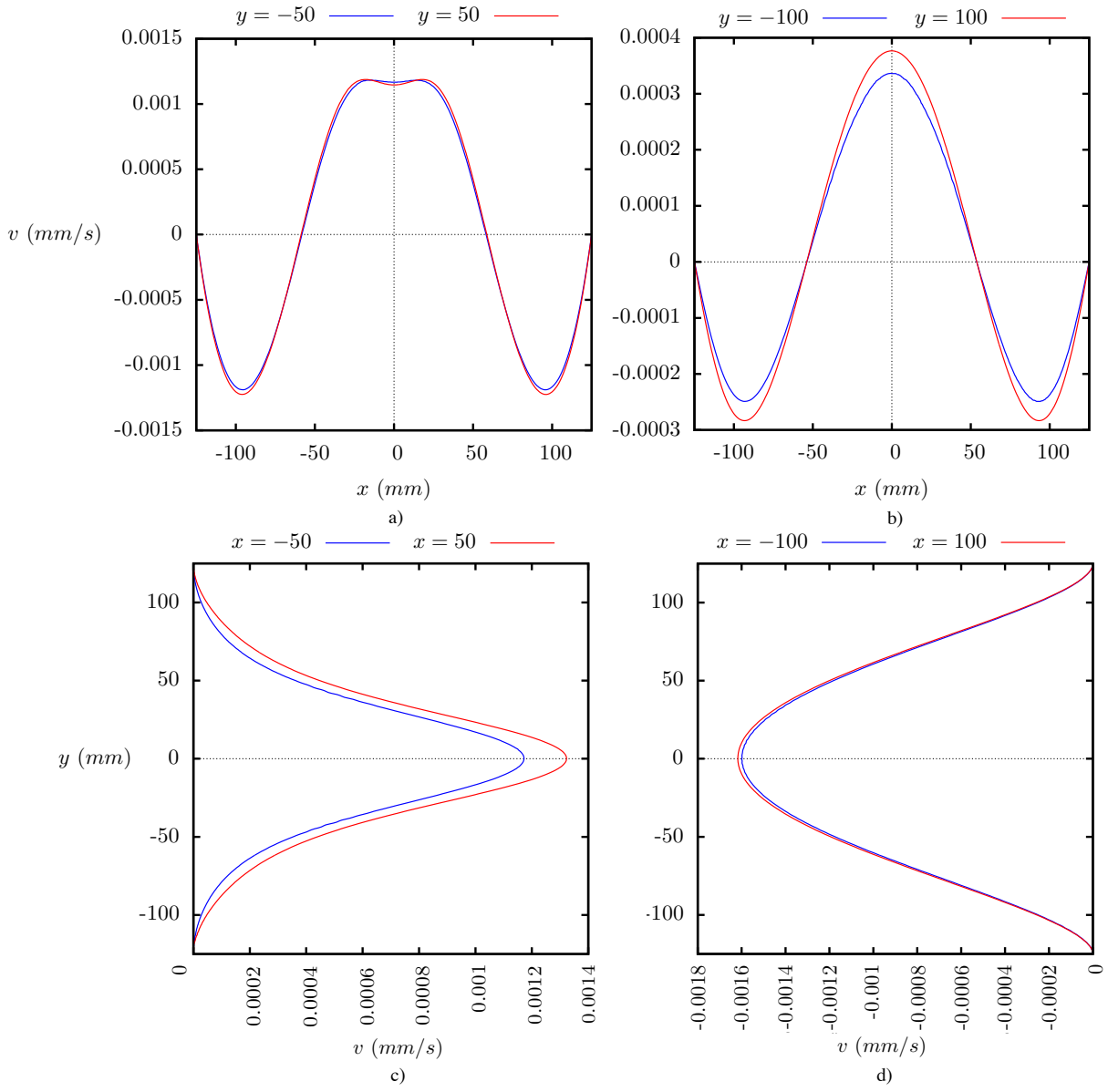

Figure 3.8: $v-$component velocity profile along x (top row) for a) $y = \pm 50$ mm and b) $y = \pm 100$ mm, and along y (bottom row) for c) $x = \pm 50$ mm and d) $x = \pm 100$ mm. $Re = 50$, $Ha = 250$. Results obtained with the two-dimensional numerical simulation.

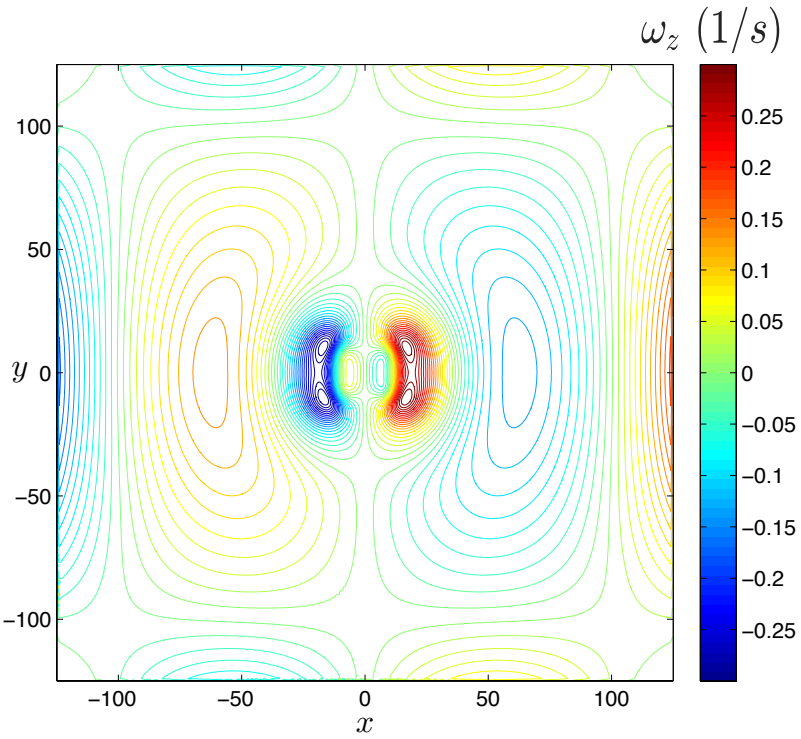

a)

Figure 3.9: Isolines of vorticity for the whole domain. $Re = 50$, $Ha = 250$. Results obtained with the two-dimensional numerical simulation.

3.6 Numerical and experimental comparison

Figure 1.3b) in Chapter 1, shows a picture of the full experimental flow domain when a DC current of 500 mA is applied in the liquid metal layer, arrows are superimposed to display the flow structure and give an idea of the size of different regions, the same vortex pattern is observed when applying different direct electrical currents between 250 mA and 1A. Visualization reveals the formation of a symmetrical structure relative to y-axis with two external recirculation zones (highlighted with white arrows) flowing in counter-clockwise and clockwise directions on the left and right sides of the flow domain, respectively. Nested within these recirculation zones, a steady vortex dipole is found (red arrows) which presents opposite sense of circulation with respect to the external vortices.

This flow structure originates two stagnation points (crosses in Fig. 1.3b) located on the symmetry axis. Further, in the center of the vortex dipole, initially a low velocity zone is formed in the region of maximum magnetic field strength. A similar velocity field obtained at the interface between the liquid metal and the acid using the PIV method is displayed in Figures shown in Chapter 1, Subsection 1.2.2. For a electric direct current of 500 mA, the maximum Hartmann number is $Ha = 184$ while the Reynolds number calculated with the maximum measured velocity within the magnet zone is $Re = 105$. Therefore, the interaction parameter takes a value of $N = 322$ which indicates the complete dominance of Lorentz forces over inertia inside the magnet region.

Figures 3.10a) and 3.10b) show the streamlines at the interface between the liquid metal and the acid layers obtained through experimental data from PIV measurements and numerical simulation, respectively, for the same case shown in Figure 1.3b) (*i.e.* $Re = 105$ and $N = 322$). Although in general there is a qualitative agreement, numerical results show a more symmetric structure and well defined stagnation points. Notice also that experimental and numerical results capture the elongation of vortex structures in the positive y-direction.

In Figure 3.11, the vorticity distribution obtained from experimental and numerical results that correspond to the case of Fig. 1.3b), are shown. Experimental data reveal a spreading of vorticity larger than numerical results as well as higher vorticity intensities in the external vortices compared with the numerical simulation.

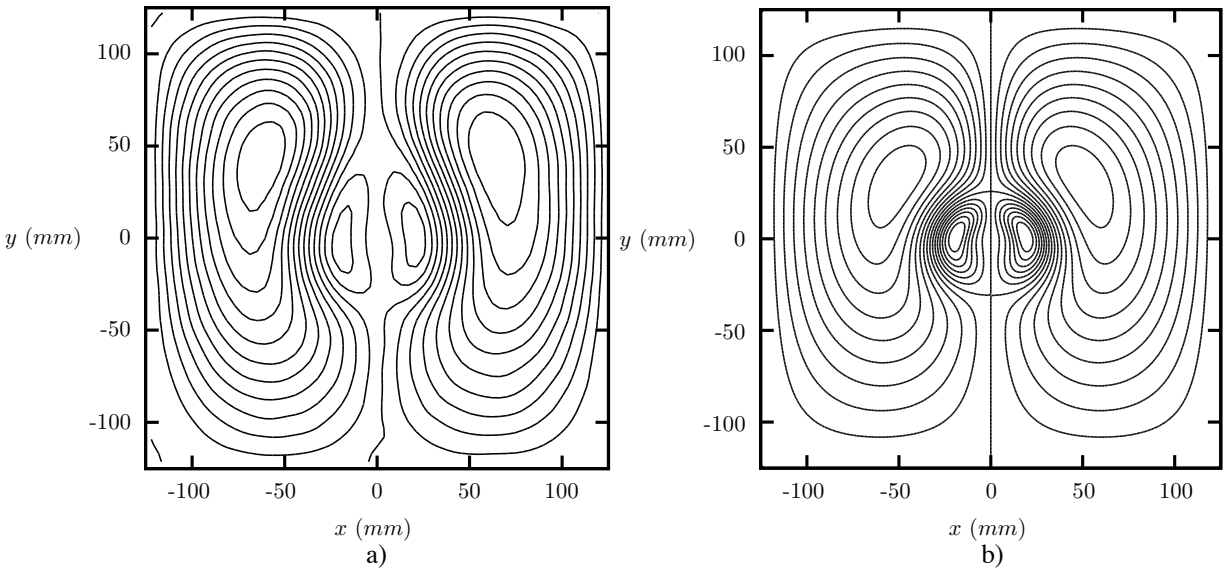

Figure 3.10: Streamlines corresponding to an applied current of 500 mA at the interface between the liquid metal and the acid layers. a) Experimental data from PIV. b) Numerical simulation. $Re = 105$ and $N = 322$.

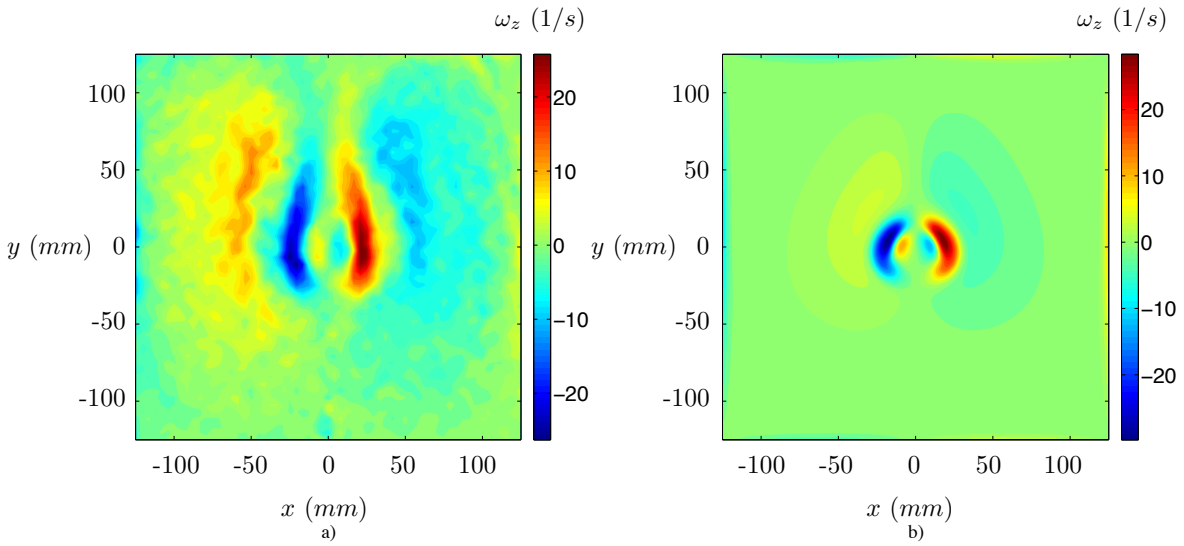

Figure 3.11: Vorticity distribution for an applied current of 500 mA at the interface between the liquid metal and the acid layers. a) Experimental PIV data. b) Numerical simulation. $Re = 105$ and $N = 322$.

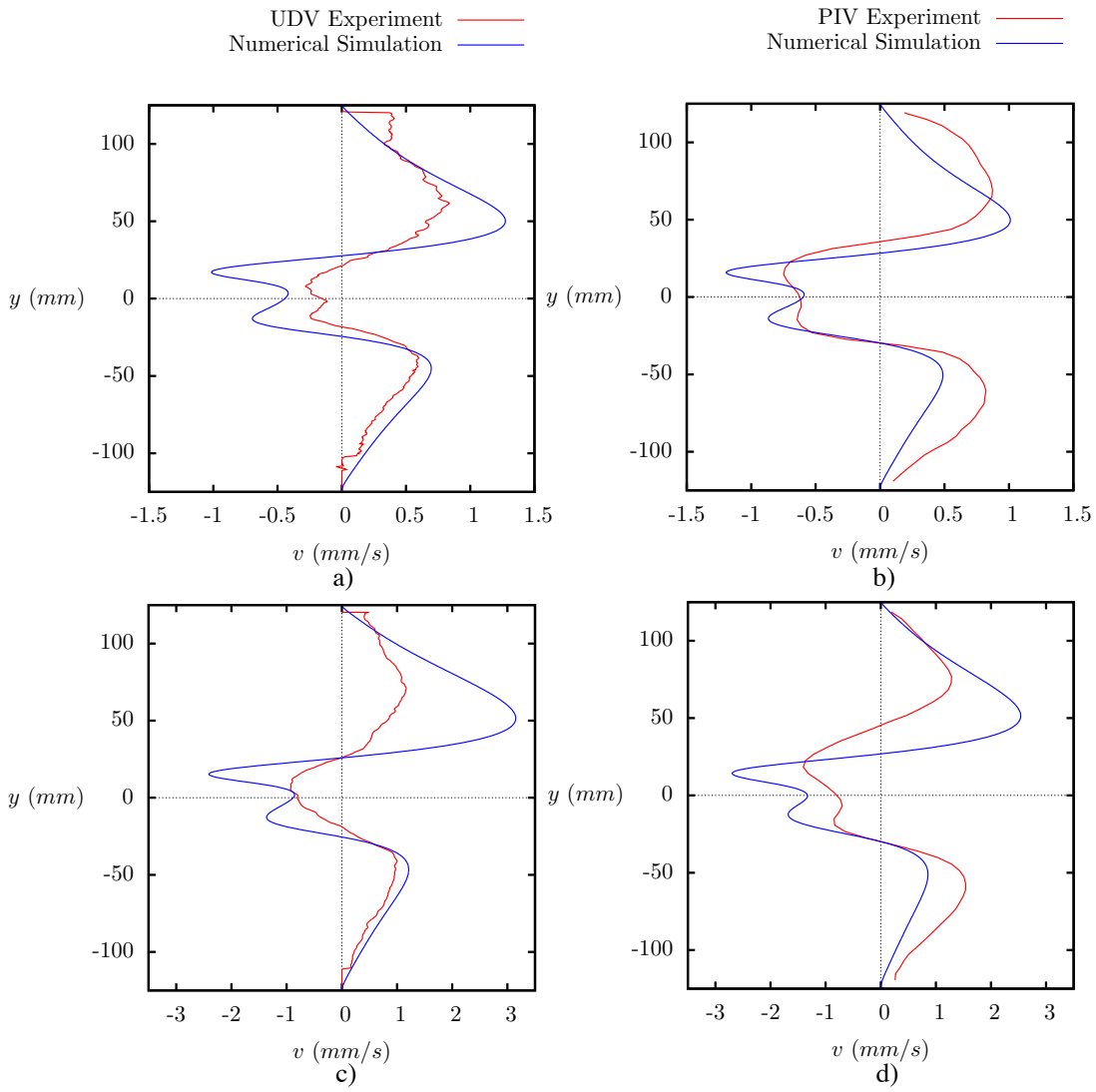

Figure 3.12: Velocity profiles along the symmetry y-axis as a function of the y-coordinate. On the left column, UDV experimental results are compared with the profile calculated numerically for a) 250 mA ($Re = 19$, $N = 2570$) and c) 500 mA ($Re = 82$, $N = 596$). On the right column, PIV results are compared with the numerical profiles for b) 250 mA ($Re = 49$, $N = 691$) and d) 500 mA ($Re = 105$, $N = 322$).

Figure 3.12 shows the comparison of the velocity profiles along the y-axis ($x = 0$) obtained through both experimental methods with profiles calculated from the numerical model. The left column compares the UDV experimental profiles with profiles calculated numerically. In Figure 3.12a) the applied current is 250 mA, corresponding to $Re = 19$ and $N = 2570$, while in Figure 3.12c) is 500 mA, that leads to $Re = 82$ and $N = 596$. In turn, the right column compares PIV profiles for 250 mA ($Re = 49$, $N = 691$) and 500 mA ($Re = 105$, $N = 322$) with numerical profiles (see Figs. 3.12b) and 3.12d). It is observed that both UDV and PIV results coincide in the general trend of velocity in the central region. Except in Fig. 3.12c), we can observe the reduction of velocity in the central zone where the magnetic field is stronger, indicating that magnitudes of applied and induced forces are comparable. Note that the lowest velocity is reached exactly at $y = 0$ and that stagnation points predicted numerically coincide with the experimental UDV measurements, while for PIV results the prediction coincides only for $y < 0$. Differences between experimental profiles obtained with each method are expected since measurements are taken at different heights from the bottom wall. On the other hand, the numerical simulation reproduces the order of magnitude and main characteristics of the velocity profiles although overestimates the velocity magnitude in some regions, particularly for $y > 0$.

The explanation of the flow structure must consider the superposition of diverse electromagnetic forces produced by the interaction of applied and induced currents with the non-homogeneous magnetic field (see Figure 3.5). The action of the applied current with the positive magnetic field in the center of the magnet produces a Lorentz force in the negative $y-$direction that promotes the formation of the inner vortex dipole. In turn, the applied current and the negative magnetic field strength at the edges of the magnet produce applied Lorentz forces in the positive $y-$direction that originates the external vortices. But currents induced by the fluid motion also have an effect as they interact with the applied field giving rise to induced forces that oppose the applied ones. In fact, induced forces, in the central region where the magnetic field is stronger, have greater magnitude than the applied Lorentz forces which generates the formation of nested internal dipolar vortex whose velocities are very low.

This study can be further explored by comparing more experimental and numerical results, for example to analyze the results presented in Chapter 1 where the formation of six vortices is clearly observed experimentally for an applied direct electric current of 350 mA, 650 mA or 750 mA.

As future observations, various experiments can be carried out analyzing only the region of the nested internal dipole vortex where the lowest recorded velocities are found, in this way what was commented in Chapter 1 could be reaffirmed and two other stagnation points can be accurately observed, which would delimit the internal dipole vortex with the nested internal dipole vortex. In addition, experiments to analyze the flow pattern at the same height of layer with the UDV and PIV techniques can be implemented.

Theoretically, the purely two-dimensional model can be compared with the quasi-two-dimensional model. Although, within the quasi-dimensional simulation a more precise mesh or a longer time can be simulated. Three-dimensional (3D) simulations considering a fully 3D magnetic field could be developed to compare with the experiments in which different direct electric currents are applied. In fact, a 3D simulation of some of the experimental results presented in this thesis was performed by (Prinz, 2019), finding a good agreement. This will enrich the observations made and improving the physical understanding of this kind of flows.

Conclusions

In this thesis, we analyzed experimentally, analytically and numerically the vortex flow in a thin liquid metal layer in a rectangular container, promoted by the interaction of a uniform DC current with a dipolar magnetic field produced by a permanent magnet of small size compared with the container. An experimental setup was developed in order to study the flow and two different measurement techniques were implemented. On the one hand, UDV technique was used for obtaining velocity profiles of one velocity component along the container. This technique was selected since it is one of the most utilized for measurements in non-transparent fluids. On the other hand, a PIV setup was performed to visualize and obtain the velocity field on the free surface of the liquid metal layer on top of which an acid layer allowed the formation of bubbles that served as tracers. A theoretical model was developed and solved analytically in order to analyze the system at creeping flow conditions. The analytical solution reproduces qualitatively the flow structures found from the experimental observations. The numerical solution of the conservation equations in a two-dimensional and quasi-two-dimensional approximations was implemented. It was found that the quasi-two-dimensional numerical solutions reproduce mostly all of the features of the flow qualitatively and quantitatively when we observe the flow pattern in the whole container. The interaction parameter of the flow is very high ($N \gg 1$) so that Lorentz forces dominate over inertia in the region over the magnet. Unlike the flow of a low conductivity liquid, where the applied Lorentz force gives rise to a well-known vortex dipole, in a liquid metal, applied and induced forces originate a different vortex flow structure. It consists of two external vortices surrounding an inner vortex dipole with a central zone where velocity is substantially reduced (quasi-stagnation zone). The existence of nested internal dipolar vortex with low-velocities is an important feature that distinguishes this vortex structure from classical ones where the maximum velocity is reached precisely in the vortex dipole axis. The interplay of the applied and induced electric currents with positive and negative field intensities in the center and edges of the magnet, respectively, determines the flow structure. The velocity profile along the symmetry axis was obtained from UDV measurements, while the velocity field in the liquid metal surface was captured by Particle Image Velocimetry (PIV). Results from quasi-two-dimensional numerical simulation grasp the main features of the flow pattern, although differences with experimental results were found in some regions. This could indicate limitations of the numerical approach and the existence of three-dimensional effects not considered in the model, although differences with PIV results may also be related to the inaccuracy introduced by tracking the dragged bubbles in the liquid metal surface. It should be mentioned that Prinz et al. (2016) have pointed out that the use of gas bubbles

as tracers is insufficient to describe the flow structures in the wake of a magnetic obstacle flow due to important three-dimensional effects.

Considering previous numerical studies of creeping flows past a magnetic obstacle (Cuevas et al., 2006; **?**), the observation of the flow patterns described in the present work could be expected in experiments similar to those reported by Samsami et al. (2014), as long as the proper values of Re and N are used.

Finally, many improvements can be made in the future both experimentally and numerically, for example, velocity measurement comparisons for the same height of the liquid metal layer both with UDV and PIV techniques. In addition, 3D simulations could be developed to compare different applied direct electric currents and, thus, enrich the physical understanding of this kind of flows.

Bibliography

Afanasyev, Y. D. and Korabel, V. N. (2004), 'Starting vortex dipoles in a viscous fluid: Asymptotic theory, numerical simulations, and laboratory experiments', *Phys. Fluids* **16**, 3850–3858.

Afanasyev, Y. D. and Korabel, V. N. (2006), 'Wakes and vortex streets generated by translating force and force doublet: laboratory experiments', *J. Fluid Mech.* **553**, 119–141.

Alboussière, T. (2004), 'A geostrophic-like model for large Hartmann number flows', *J. Fluid Mech.* **521**, 125–154.

Alemany, A., Moreau, R., Sulem, P. L. and Frisch, U. (1979), 'Influence of an external magnetic field on homogeneous mhd turbulence', *J. Méc.* **18**, 277–313.

Alzabut, J., Nadeem, S., Noor, S. and Eldin, S. M. (2023), 'Numerical analysis of magnetohydrodynamic convection heat flow in an enclosure', *Results in Physics* **51**, 106618.

Andreev, O., Kolesnikov, Y. and Thess, A. (2009), 'Application of the ultrasonic velocity profile method to the mapping of liquid metal flows under the influence of a non-uniform magnetic field', *Exp. Fluids* **46**, 77–83.

Batchaev, A. M. and Ponomarev, V. M. (1989), 'Experimental and theoretical investigation of kolmogorov flow in a cylindrical surface', *Izvestiya Akademii Nauk SSR, Mekhanika Zhidkosti i Gaza* **5**, 25–31.

Beltrán, A. (2010), Flow Dynamics in magnetic obstacle, PhD thesis, UNAM.

Bondarenko, N. F. and Gak, M. Z. (1978), 'Application of magnetohydrodynamic effects in electrolytes for modeling eddy hydrodynamic processes', *Atmospheric and Oceanic Physics* **14** (2), 146–150.

Bondarenko, N. F., Gak, M. Z. and Dolzhanskiy, F. V. (1979), 'Laboratory and theoretical models of plane periodic flow', *Atmospheric and Oceanic Physics* **15** (10), 711–716.

Brito, D., Nataf, H.-C., Cardin, P., Aubert, J. and Masson, J. (2001), 'Ultrasonic doppler velocimetry in liquid gallium', *Exp. Fluids* **31**, 653–663.

Bühler, L. (1996), 'Instabilities in quasi-two-dimensional magnetohydrodynamics flows', *J. Fluid Mech.* **326**, 125–150.

Bühler, L., Brinkmann, H.-J. and Mistrangelo, C. (2020), 'Experimental investigation of liquid metal pipe flow in a strong non-uniform magnetic field', *Magnetohydrodynamics* **56**, 131–138.

Cherkaoui, I., Bettaibi, S., Barkaoui, A. and Kuznik, F. (2022), 'Magnetohydrodynamic blood flow study in stenotic coronary artery using lattice boltzmann method', *Computer Methods and Programs in Biomedicine* **221**, 106850.

Cramer, A., Zhang, C. and Eckert, S. (2004), 'Local flow structures in liquid metals measured by ultrasonic doppler velocimetry', *Flow Meas. Instrum.* **15**, 145–153.

Cruz-Gómez, R. C., Zavala-Sanzón, L. and Pinilla, M. A. (2013), 'Generation of isolated vortices in a rotating fluid by means of an electromagnetic method', *Exp. Fluids* **54(8)**, 1–11.

Cuevas, S. and Ramos, E. (1997), 'Steady streaming in oscillatory viscous flow under a transverse magnetic field', *Phys. Fluids* **9**, (5) 1430–1434.

Cuevas, S., Sierra, F. Z. and Avramenko, A. (2002), 'Magnetic damping of steady streaming vortices in an oscillatory viscous flow over a wavy wall', *Magnetohydrodynamics.* **38**, 4 (345–358).

Cuevas, S., Smolentsev, S. and Abdou, M. (2006), 'Vorticity generation in the creeping flow past a magnetic obstacle', *Phys. Rev. E* **74**, 056301(1–10).

Davidson, P. A. (1995), 'Magnetic damping of jets and vortices', *J. Fluid Mech.* **229**, 153–186.

Davidson, P. A. (2001), *Introduction to magnetohydrodynamics flows*, Cambridge.

Dolzhanskii, F. V., Krymov, V. A. and Manin, D. Y. (1990), 'Stability and vortex structures of quasi-two-dimensional shear flows', *Soviet Physics Uspekhi* **33** (7), 495–520.

Dolzhanskii, F. V., Krymov, V. A. and Manin, D. Y. (1992), 'An advanced experimental investigation of quasi-two-dimensional shear flows', *J. Fluid Mech.* **241**, 705–722.

Dong, J., Zhu, Y., Liu, Z. and Wang, M. (2021), 'Liquid Metal-Based Devices: Material Properties, Fabrication and Functionalities', *Nanomaterials* **11**(12).

Dovzhenko, V. A., Novikov, Y. V. and Obuhkov, A. M. (1979), 'Modeling the vortex generation process in an axially symmetrical azimuthal field by a magnetohydrodynamic method', *Atmospheric and Oceanic Physics* **15** (11), 834–836.

Dovzhenko, V. A., Obuhkov, A. M. and Ponomarev, V. M. (1981), 'Generation of vortices in an axisymmetric shear flow', *Izvestiya Akademii Nauk SSR, Mekhanika Zhidkosti i Gaza* No. 4, 27–36.

Figueroa, A. (2006), Generación de vorticidad mediante fuerzas magnéticas, Master's thesis, UNAM.

Figueroa, A. (2010), Dynamics of electromagnetically driven vortices, PhD thesis, UNAM.

Figueroa, A., Cuevas, S. and Ramos, E. (2011), 'Electromagnetically driven oscillatory shallow layer', *Phys. Fluids* **23**, 013601.

Figueroa, A., Cuevas, S. and Ramos, E. (2017), 'Lissajous trajectories in electromagnetically driven vortices', *J. Fluid Mech.* **815**, 415–434.

Figueroa, A., Demiaux, F., Cuevas, S. and Ramos, E. (2009), 'Electrically driven vortices in a weak dipolar magnetic field in a shallow electrolytic layer', *J. Fluid Mech.* **641**, 245–261.

Figueroa, A., Meunier, P., Cuevas, S., Villermaux, E. and Ramos, E. (2014), 'Chaotic advection at large péclet number: electromagnetically driven experiments, numerical simulations, and theoretical predictions', *Phys. Fluids* **26**, 013601.

Gary Leal, L. (2007), *Advanced Transport Penomena*, Cambridge.

Good, R. H. and Nelson, T. J. (1971), *Classical theory of electric and magnetic fields*, Academic Press.

Hamid, S. H. A., Hussam, W. K., Pothérat, A. and Sheard, G. J. (2015), 'Spatial evolution of a quasi-two-dimensional kŕmán vortex street subjected to a strong uniform magnetic field', *Phys. Fluids* **27**, 053602.

Hickie-Bentzen, A., Tasnim, S. H. and Mahmud, S. (2023), 'Magnetohydrodynamic thermal diode using natural convection of in-ga-sn alloy in a square enclosure with an insulating body', *Thermal Science and Engineering Progress* **39**, 101736.

Hughes, W. and Young, F. (1966), *The Electromagnetodynamics of Fluid*, John Wiley and Sons.

Kim, M.-g., Alrowais, H., Pavlidis, S. and Brand, O. (2017), 'Size-Scalable and High-Density Liquid-Metal-Based Soft Electronic Passive Components and Circuits Using Soft Lithography', *Advanced Functional Materials* **27**(3), 1604466.

Klaasen, B., Verhaeghe, F., Blanpain, B. and Fransaer, J. (2014), 'A study of gas bubbles in liquid mercury in a vertical hele-shaw cell', *Exp. Fluids* **55**, 1652(2–13).

Klein, R., Pothérat, A. and Alferenok, A. (2009), 'Experiment on a confined electrically driven vortex pair', *Phys. Rev. E* **79**, 016304.

Klüber, V., Bühler, L. and Mistrangelo, C. (2020), 'Numerical investigation of liquid metal flow in square channels under inclined magnetic fields for fusion relevant parameters', *Magnetohydrodynamics* **56**, 149–156.

Kolesnichenko, I., Khripchenko, S., Buchenau, D. and Gerbeth, G. (2005), 'Electrovortex flows in a square layer of liquid metal', *Magnetohydrodynamics.* **41**, 39–51.

Krymov, V. A. (1989), 'Stability and supercritical regimes of quasi-two-dimensional shear flow in the presence of external friction (experiment)', *Izvestiya Akademii Nauk SSR, Mekhanika Zhidkosti i Gaza* No. 2, 12–18.

Lara, C. G. (2013), Estudio teórico-experimental de la agitación electromagnética de flujos en aguas someras, PhD thesis, UNAM.

Lara, C. G., Figueroa, A. and Cuevas, S. (2017), 'Nested dipolar vortices driven by electromagnetic forces in a thin liquid metal layer', *Magnetohydrodynamics.* **4**, 1–10.

Li, K., Turcotte, K. and Veres, T. (2019), Stretchable strain sensors based on thermoplastic elastomer microfluidics embedded with liquid metal, *in* '2019 IEEE SENSORS', pp. 1–4.

Liu, Y., Wang, Q., Jia, Y. and Zhu, P. (2020), 'A Frequency- and Polarization-Reconfigurable Slot Antenna Using Liquid Metal', *IEEE Transactions on Antennas and Propagation* **68**(11), 7630–7635.

Manin, D. Y. (1989), 'Stability and Supercritical Regimes of Quasi-Two-Dimensional Flow in the Presence of External Friction (Theory)', *Izvestiya Akademii Nauk SSR, Mekhanika Zhidkosti i Gaza* No. 2, 19–26.

McCaig, M. (1977), *Permanent Magnets in Theory and Practice*, Wiley.

McClung, S. N., Saeedi, S. and Sigmarsson, H. H. (2018), 'Band-Reconfigurable Filter With Liquid Metal Actuation', *IEEE Transactions on Microwave Theory and Techniques* **66**(6), 3073–3080.

Messadek, K. and Moreau, R. (2002), 'An experimental investigation of quasi-two-dimensional turbulent shear flows', *J. Fluid Mech.* **456**, 137–159.

Mistrangelo, C., BÃ¼hler, L., Smolentsev, S., KlÃ¼ber, V., Maione, I. and Aubert, J. (2021), 'MHD flow in liquid metal blankets: Major design issues, MHD guidelines and numerical analysis', *Fusion Engineering and Design* **173**, 112795.

Moffatt, H. K. and Toomre, J. (1967), 'The anihilation of a two dimensional jet a transverse magnetic field', *J. Fluid Mech.* **30 (1)**, 65–82.

Morley, N. B., Burris, J., Cadwallader, L. C. and Nornberg, M. D. (2008), 'Gainsn usage in the research laboratory', *Rev. Sci. Instrum.* **79**, 056107(1–3).

Mück, B., Günther, C., Müller, U. and Bühler, L. (2000), 'Three-dimensional mhd flows in rectangular ducts with internal obstacles', *J. Fluid Mech.* **418**, 265–295.

Müller, U. and Bühler, L. (2001), *Magnetofluiddynamics in channels and containers*, Springer.

Nauber, R., Burger, M., Büttner, L., Franke, S., Räbiger, D., Eckert, S. and Czarske, J. (2013), 'Novel ultrasound array measurement system for flow mapping of complex liquid metal flows', *Eur. Phys. J. Special Topics* **220**, 43–52.

Nguyen Duc, J. M. and Sommeria, J. (1988), 'Experimental characterization of steady two-dimensional vortex couples', *J. Fluid Mech.* **192**, 175–192.

Otake, S. and Konishi, S. (2018), Integration of flexible strain sensor using liquid metal into soft micro-actuator, *in* '2018 IEEE Micro Electro Mechanical Systems (MEMS)', pp. 571–574.

Özişik, M. N. (1993), *Heat conduction*, 2nd edn, Wiley, New York.

Pérez-Barrera, J., Ortiz, A. and Cuevas, S. (2016), *Analysis of an annular MHD stirrer for microfluidic applications*, Springer, 275-288.

Ponomarev, V. M. (1980), 'Stability of a class of axisymmetric flows of an incompressible liquid', *Izvestiya Akademii Nauk SSR, Mekhanika Zhidkosti i Gaza* No. 1, 3–9.

Pothérat, A., Sommeria, J. and Moreau, R. (2000), 'An effective two-dimensional model for mhd flows with transverse magnetic field', *Phys. Fluids* **9 (10)**, 3102–3104.

Prinz, S. (2019), Direct and large-eddy simulations of wall-bounded magnetohydrodynamic flows in uniform and non-uniform magnetic fields, PhD thesis, Technical University of Ilmenau.

Prinz, S., Bandaru, V., Kolesnikov, Y., Krasnov, D. and Boeck, T. (2016), 'Numerical simulations of magnetohydrodynamic flows driven by a moving permanent magnet', *Phys. Rev. Fluids.* **1**, 043601.

Rivero, M., Ávalos-Zúñiga, R. A. and Cuevas, S. (2022), 'A liquid metal mhd voetex generator for energy harvesting applications', *Magnetohydrodynamics* **58**(4), 491–499.

Salas, H., Cuevas, S. and Ramos, E. (2001), 'Electrically driven vortices in a dipolar magnetic field', *J. Fluid Mech.* **37**, 38–44.

Samsami, F., Kolesnikov, Y. and Thess, A. (2014), 'Vortex dynamics in the wake of a magnetic obstacle', *J. Vis.* **17**, 245252.

Satijn, M. P., Cense, A. W., Verzicco, R., Clercx, H. J. H. and van Heijst, G. J. F. (2001), 'Three-dimensional structure and decay properties of votices in shallow fluid layers', *Phys. Fluids* **13(7)**, 1932–1945.

Shercliff, J. A. (1965), *A Textbook of Magnetohydrodynamics*, Pergamon Press.

Singh, R. J. and Gohil, T. B. (2019), 'Numerical study of mhd mixed convection flow over a diamond-shaped obstacle using openfoam', *International Journal of Thermal Sciences* **146**, 106096.

Smolentsev, S. (1997), 'Averaged model in mhd duct flow calculations', *Magnetohydrodynamics.* **33(1)**, 42–47.

Smolentsev, S., Cuevas, S. and Beltrán, A. (2010), 'Induced electric current-based formulation in computations of low magnetic reynolds number magnetohydrodynamic flows', *J. Comput. Phys.* **229**, 1558–1572.

Sommeria, J. (1986), 'Experimental study of the two-dimensional inverse energy cascade in a square box', *J. Fluid Mech.* **170**, 139–168.

Sommeria, J. (1988), 'Electrically driven vortices in a strong magnetic field', *J. Fluid Mech.* **189**, 553–569.

Sreenivasan, B. and Alboussière, T. (2000), 'Evolution of a vortex in a magnetic field', *Eur. J. Mech. B-Fluids* **19**, 403–421.

Sreenivasan, B. and Alboussière, T. (2002), 'Experimental study of a vortex in a magnetic field', *J. Fluid Mech.* **456**, 137–159.

Takeda, Y. (1986), 'Velocity profile measurements by ultrasound doppler shift method', *Intnl J. Heat Mass Flow* **7**, 313–318.

Takeda, Y. (1991), 'Development of an ultrasound velocity profile monitor', *Nucl. Eng. and Design* **126**, 277–284.

Takeda, Y. (1995), 'Instantaneous velocity profile measurement by ultrasound doppler method', *Int. J. JSME Ser B.* **38(1)**, 8–16.

Thielicke, W. and Sonntag, R. (2021), 'Particle image velocimetry for MATLAB: Accuracy and enhanced algorithms in PIVlab', *Journal of Open Research Software* **9**.